Advances in All-Optical Magnetometry for Femto-Tesla Sensitivity in Earth-Field-Scale Magnetic Fields

by
Michael Bulatowicz

A dissertation submitted in partial fulfillment
of the requirements for the degree of
Doctor of Philosophy
Physics

at the
University of Wisconsin-Madison
2023

Date of Final Oral Exam: 09/08/2023
The dissertation is approved by the following members of the Final Oral Committee:

Dr. Thad G. Walker, Professor, Physics
Dr. Deniz Yavuz, Professor, Physics
Dr. Ronald T. Wakai, Professor, Medical Physics
Dr. Jennifer Choy, Assistant Professor, Electrical and Computer Engineering

Advances in All-Optical Magnetometry for Femto-Tesla Sensitivity in Earth-Field-Scale Magnetic Fields

Michael D. Bulatowicz

Abstract

The ability to detect femto-Tesla (10^{-15}) magnetic fluctuations in the presence of large background magnetic fields encountered in unshielded environments on Earth is a capability which can enable a wide array of applications presently requiring magnetically shielded environments. This has been possible for many years through the use of superconducting quantum interference devices (SQUIDs); however, SQUIDs are expensive to purchase, operate, and maintain. In contrast to SQUIDS, optically pumped magnetometers based on warm alkali vapor are relatively inexpensive to purchase, operate, and maintain while promising similar sensitivity capabilities.

In the present work, I have demonstrated an optically pumped scalar magnetometer using a 1 cm diameter by 1 cm length internal dimension cylindrical vapor cell with a photon shot noise limit of 3.5 $fT/\sqrt{Hz}$ and a demonstrated single-channel noise of 10 $fT/\sqrt{Hz}$ as limited by the electrical current source generating a 29 μT bias field. I have further demonstrated a differential pair of these magnetometers, separated by a distance of 9 cm, with measured differential noise of 1 $fTcm^{-1}/\sqrt{Hz}$, consistent with a single-channel noise of 6 $fT/\sqrt{Hz}$. I present a straightforward procedure for optimization of the sensitivity of this magnetometer to achieve fundamental sensitivity limits in the low single digit $fT/\sqrt{Hz}$ and guidelines for detection electronics supporting total noise from the magnetometer dominated by the fundamental sensitivity limit. I demonstrate, analyze, and characterise the basis of a method for detection of the vector components of the incident magnetic field through the use of an applied oscillating field along each vector axis to be measured, and I present initial results with single-axis vector component detection. Included in the relevant chapter are algorithms and feedback methods for achieving high performance, along with a demonstration of each, and measurements of performance including relative accuracy and uncertainty. I further present a demonstration and theory of detection of RF magnetic fields near the natural Larmor precession frequency of the spins, taking advantage of the AC Stark shift of the optical pump beam to generate a linear sensitivity to the RF signal, measured at the difference between the RF frequency and Larmor frequency. Finally, I look toward future work, proposing a method for measurement of the vector direction of the incident magnetic field by real-time observation of the spin precession.

Dedication

To my wonderful, loving wife Julie. I could never have completed this work without your unwavering love and support. Words cannot express my gratitude and appreciation for all that you've done to help me through this journey.

Acknowledgements

First, I would like to thank my advisor, Dr. Thad Walker. Thad's depth and breadth of knowledge and his enthusiasm for physics helped inspire me to make the decision to return to school after a decade of working full time as a mechanical engineer and pivot to pursuing an advanced degree in Physics. Even before making the decision to go back to school, I thoroughly enjoyed working with Thad and learning from him over the course of several years of his help and advice on the atom-based sensors on which I have worked at Northrop Grumman. After all that I had learned from Thad already and in no small part based on the type of person he had demonstrated himself to be, I knew whom I wanted to have as my advisor. I contacted Thad, who immediately agreed to take me on as a grad student–provided that I was accepted to the University of Wisconsin - Madison–and he recommended books for me to study in order to catch up on a good deal of the undergrad physics to which I hadn't been exposed as a mechanical engineering student. Thus began a process that has taken nearly ten years all told and has had many unexpected twists and turns. Thad has been steadfast and supportive through it all, even tolerating my often-excessive independence in my experimental efforts.

I would like to thank the Department of Physics at the University of Wisconsin - Madison. I have learned a great deal of physics in my time as a graduate student and I have thoroughly enjoyed learning from a number of impressively talented physicists eager to pass their knowledge along to the next generation. The knowledge and experience I gained as a result have made me both a much better physicist and a better engineer. The support staff–both those with whom I interacted directly and the behind-the-scenes people who keep the department running smoothly–have been no small part of the great experience I have had in graduate school.

While I learned a great deal in all of my courses, particularly memorable courses include quantum mechanics with Professor Lisa Everett–I've never seen anyone coherently and correctly write equations on a whiteboard even half as quickly while rapid-fire explaining everything in detail–very impressive; lasers and optics with Professor Deniz Yavuz–thoroughly enjoyable and somehow simultaneously laid-back and rigorous with a great deal of highly informative in-class discussion; classical mechanics with Professor Jeff Schmidt–I've never had so many hours of homework in my life from a class that managed to cover all thirteen chapters of *Classical Mechanics* (Goldstein 1980) plus supplementary material; and Introduction to Atomic Structure with Professor Mark Saffman–directly useful to the present work.

I would like to thank Dr. Ron Wakai for his efforts and support in collaborating with Thad and tolerating our presence in the magnetically shielded room during our participation in the fetal biomagnetism experiment. I learned a great deal about biomagnetism and

about challenges and obstacles to overcome in attempting to observe small biomagnetic signals. I would also like to thank everyone with whom I worked as a member of Thad's group: postdoctoral researchers Ibrahim Sulai, Josh Weber, and Elena Zhivun; graduate students Anna Korver, Dan Thrasher, Zack Deland, Susan Sorensen, and Matt Ebert; and undergraduate lab assistants Colin Wahl, Alec Hryciuk, and Jonas Tost. It was fun to work beside all of you, learn from you, and teach what I could whenever the opportunity arose. Last but certainly not least, I would like to thank my family for their love and support in this endeavor. Thank you for everything.

This research was supported by the National Science Foundation (GOALI award PHY-1912543) and by Northrop Grumman Mission Systems University Research Program.

Contents

List of Figures

List of Tables

Chapter 1

Introduction

1.1 Introduction

The ability to detect weak magnetic fluctuations in the presence of large background magnetic fields encountered in unshielded environments on Earth is a capability which can enable a wide array of applications presently requiring magnetically shielded environments. Applications such as biomagnetic signal detection (Strasburger, Cheulkar, and B.; Wakai 2008; Hämäläinen et al. 1993; I. Sulai et al. 2019; Boto et al. 2022; Rea et al. 2022; Klotz, Gizzi, and Röhrle 2022; Hoshino et al. 2022), geosensing (Lorenz, Jones, and J. Wu 2003), dark matter searches (Afach et al. 2021), infrastructure monitoring (Vo et al. 2020), materials inspection (Koss et al. 2022), navigation aiding (A. Canciani and Raquet 2016), RF detection (Lee, V.G. Lucivero, et al. 2021), and many more can benefit from a sensor capable of detecting femto-Tesla (10^{-15}) fluctuations in Earth-field-scale magnetic fields in the tens of μT. This has been possible for many years through the use of superconducting quantum interference devices (SQUIDs); however, while these instruments are extremely sensitive magnetometers, they exhibit the significant disadvantage of requiring cryogenic cooling. SQUIDs are expensive to purchase, operate, and maintain. In contrast to SQUIDS, magnetometers based on warm alkali vapor are relatively inexpensive to purchase, operate, and maintain. In particular, optically pumped atomic magnetometers, often colloquially referred to as simply optically pumped magnetometers (OPMs), offer

the opportunity to build large arrays of non-interfering sensitive elements in addition to exhibiting fundamental limits of performance competitive with SQUIDs. Improvements in production techniques and quality of components, accompanied by increased portability and sensitivity, has resulted in increased interest in optical atomic magnetometers over recent years.

Optically pumped atomic magnetometers utilize the predictable and stable precession of spins in a magnetic field as a means of measuring the magnitude of that field. William E. Bell and Arnold L. Bloom first demonstrated 66 years ago (Bell and Bloom 1957, Bell and Bloom 1961) that modulation of the optical pumping dynamics in a manner synchronous with the natural Larmor precession frequency of the spins provides a means for an all-optical drive and interrogation of the spin precession. Since the initial demonstration of Bell and Bloom's synchronously pumped magnetometer, deeper understanding of the underlying physics, coupled with improvements in enabling technologies such as lasers, fast optical modulators, photodetectors, and analog and digital electronics have dramatically improved the achievable magnetic sensing performance. Relevant to this work, these advancements have improved the feasibility of a fieldable synchronously pumped magnetometer based on pulses of optical pumping light rather than continuous modulation (Grujic and Weis 2013; H. Huang et al. 2015; Gerginov and S. K. S. Knappe 2017; Gerginov, Pomponio, and S. Knappe 2020; Songsong Li et al. 2021; Gartman et al. 2018).

1.2 Background and Motivation

The most sensitive optically pumped magnetometer for detection of low-frequency magnetic field fluctuations (where low frequency is defined as slower than the spin polarization relaxation rate) is the spin-exchange relaxation free (SERF) magnetometer (Allred et al. 2002), which has demonstrated magnetic noise as low as 0.16 $fT/\sqrt{Hz}$ (H.B. Dang, A.C. Maloof, and M.V. Romalis 2010). SERF magnetometers such as the work of H.B. Dang, A.C. Maloof, and M.V. Romalis 2010 are inherently vector magnetometers, detecting the

component of magnetic field orthogonal to the optical pump beam by way of the spins tipping away from the pump axis and into the orthogonal probe axis; thus, SERF magnetometers can provide vector component information about the incident magnetic field. The key advantage of the SERF regime over other methods of magnetic field measurement using optically pumped spins is that the spin-polarization relaxation mechanism driven by spin-exchange collisions is greatly suppressed, resulting in much longer achievable polarization lifetimes and correspondingly reduced fundamental noise limits as compared to magnetometer technologies operating without suppression of spin-exchange relaxation.

One key disadvantage of SERF magnetometers is that they operate in the fast spin exchange limit, wherein the spin exchange rate is many times faster than the precession frequency; for optimal operation, they require near zero net magnetic field in order to dramatically suppress the spin-exchange relaxation. A second key disadvantage is that SERF magnetometers require calibration to achieve a high degree of accuracy: for example, when running a SERF magnetometer with closed-loop response based on driving a magnetic field via a coil along the sensitive axis to zero out the incident field, calibration of the magnetic field coil response is required. Based on these disadvantages, SERF magnetometers are suitable only for a subset of high-sensitivity magnetometry applications: specifically, those which can be performed in a near-zero-field environment such as can be achieved using magnetic shielding, or with the use of carefully tuned externally-applied magnetic fields (S. Seltzer and M. Romalis 2004a).

Optically pumped magnetometers that directly measure the resonant precession frequency of a polarized ensemble of spins in a magnetic field, on the other hand, are not dependent on near-zero-field environments for optimal sensitivity and overcome the calibration limits to a great extent. Specifically, as will be described in more detail in Chapter 2, the instrument physics do not directly limit the accuracy of the sensor: in principle, the conversion factor from magnetic field to precession frequency is based on fundamental physical constants, and only the particular implementation of the magnetometer will limit the accuracy. One example of an optically pumped magnetometer that utilizes the

precession frequency of an ensemble of spins in a magnetic field is the Bell-Bloom magnetometer (Bell and Bloom 1957; Bell and Bloom 1961) concept that is used in the present work. The precession frequency of the spins, being a scalar quantity, is a measure of the magnitude of the magnetic field but not its direction: using only the precession frequency information, then, the instrument is inherently a scalar magnetic field sensor.

While in a subset of the applications mentioned above, scalar field measurements are sufficient, full knowledge of vector components provides additional insight into the ambient field. Vector component information is useful for many applications, including magnetoencephalography (Boto et al. 2022; Rea et al. 2022), magnetometer-based tracking of a magnetic object (for example, Soheilian, Ranjbaran, and Tehranchi 2020), and the enhancement of magnetic-field-based navigation aiding (A. J. Canciani and Brennan 2020), using a greater portion of the information available in Earth's magnetic field as compared to scalar measurement alone (NOAA n.d.). There is further interest in utilizing vector component information to correct for inherent "heading errors" in alkali-based magnetometers, which results from the non-zero nuclear spin of alkali atoms (Lee, V. Lucivero, et al. 2021). Magnetic vector component measurement further enables the measurement of the magnetic gradient tensor Sui et al. 2014, which may improve the precision and accuracy of, for example, navigation aiding (Y. Huang, L. Wu, and D. Li 2015).

The most sensitive vector magnetometry in unshielded environments is presently performed using superconducting quantum interface device (SQUID) magnetometers. The SQUID magnetometer is inherently a vector sensor and detects field projections along its sensitive axis. Furthermore, its capacity to achieve ultrahigh sensitivity has been demonstrated in Earth-field environments (Schönau et al. 2013). A key disadvantage is that SQUIDs require cryogenic cooling and are therefore only applicable to a subset of vector detection applications; those in which the physical size required for sufficient thermal insulation and ongoing cost of achieving and maintaining the required cryogenic temperatures are acceptable. In contrast, optically pumped atomic magnetometers capable of operating in Earth-field-scale magnetic fields typically function by measuring the Larmor

precession frequency of atomic spins of vapor-phase alkali metals (Budker and M. Romalis 2007) or helium (Grosz, Haji-Sheikh, and Mukhopadhyay 2017) in the presence of magnetic fields, and thus are inherently scalar field sensors. However, methods have been demonstrated for the measurement of the vector components of Earth-field-scale incident magnetic fields using these sensors, with at least one example making use of microwave polarization reconstruction (Thiele, Lin, and Brown 2018) and others using methods such as scanning magnetic fields (Alldredge 1960) and rotating fields oscillating at frequencies much faster than the spin relaxation rate (T. Wang et al. 2023). Thus, in contrast to inherent vector sensors such as SQUIDs, 3-axis magnetic sensing using an OPM does not inherently require three physically separate devices, adding physical complexity and potentially degrading the measurement accuracy for nearby sources of magnetic field. Additionally, unlike SQUID magnetometers, OPMs do not require cryogenic cooling, thus reducing operating costs, broadening the application space, and improving portability.

Optically pumped magnetometers have also been demonstrated for radio-frequency (RF) magnetic field detection up to and including the MHz regime without the use of cryogenic cooling (for example, Keder et al. 2014a; Lee, V.G. Lucivero, et al. 2021; I.M. Savukov et al. 2005). Detection of magnetic fields at RF frequencies is useful for many applications from ultra-low-field MRI (Mazurek, Cahn, Yuen, et al. 2021) to NMR spectroscopy (I.M. Savukov et al. 2005), communications (Gerginov and Silva 27 September 2022; I. Savukov, Kim, and Boshier 2017; Bai et al. 2023) and beyond. In contrast to an inductive pick-up coil (Gruber et al. 2018), optically pumped atomic magnetometers are effectively insensitive to electric fields and do not exhibit inductive cross-coupling, making them particularly amenable to use in array configurations. Optically pumped magnetometers configured for detection of RF signals in the range of tens of kHz and above tend to optically pump the spins along the bias field and allow the incident RF field to stimulate resonant or near-resonant precession of the spins about the bias field (Keder et al. 2014b; Lee, V.G. Lucivero, et al. 2021; Bevington, Gartman, and Chalupczak 2019). In this configuration, optically pumped RF magnetometers utilize an optical probe beam

orthogonal to the optical pump to detect the component of spin orthogonal to the bias field. Optical pumping along the bias field allows for an effect known as light narrowing (Appelt et al. 1999) in which spin-exchange relaxation is suppressed by pumping the spins into a stretched state ($m_F = F$); the resulting decrease in relaxation rate allows for improved sensitivity at the cost of reduced detection bandwidth. These magnetometers have demonstrated fT-level sensitivity to incident RF magnetic fields, at the cost of requiring calibration to measure low-frequency magnetic field fluctuations.

Recent advancements (M. Limes et al. 2020) have further demonstrated that optically pumped magnetometers based on similar operational concepts to those used in the present work provide noise levels sufficient for biomagnetic applications in an unshielded earth field environment. Recent work has demonstrated the ability of OPMs to achieve sub-$fT/\sqrt{Hz}$ sensitivities in near-zero field environments (H. Dang, A. Maloof, and M. Romalis 2010) and 3-axis vector sensitivity in near-zero-field environments (Boto et al. 2022; Rea et al. 2022; K. Wang et al. 2022; Yan et al. 2022; Lu et al. 2022; S. Seltzer and M. Romalis 2004a) and 3-axis vector sensitivity in μT-level environments with relatively small vector components orthogonal to the bias field (H. Huang et al. 2015). Yet more advances have been made in extending the operational range of spin-polarized optically pumped magnetometers into the Earth-field regime (Gerginov and S. K. S. Knappe 2017; S. Seltzer and M. Romalis 2004b; A. Perry et al. 2020; Oelsner et al. 2022; S. Seltzer and M. Romalis 2004a; A. R. Perry et al. 2020; M. Limes et al. 2020). Each exhibits it own set of advantages and limitations.

1.3 Overview of This Work

In the 60 years since the pioneering work of Bell and Bloom, supporting technologies for all-optical magnetometers have undergone dramatic improvements, from lasers and optics to fabrication techniques, electronics components, computer software, and more. I have built upon these advancements through rigorous application of physics and advanced electromechanical engineering to demonstrate improvements in sensitivity, bandwidth, apparatus

simplicity, or some combination thereof over other modern optically pumped atomic magnetometers capable of operating in Earth-field-scale magnetic fields; for example, Gerginov and S. K. S. Knappe 2017; S. Seltzer and M. Romalis 2004b; A. Perry et al. 2020; Oelsner et al. 2022; S. Seltzer and M. Romalis 2004a; M. Limes et al. 2020; *GEM Systems GSMP-35 Potassium Magnetometer* 2023. I use deterministic physics-based magnetometer optimization and deterministic physics-based procedural tuning of spin ensemble response to magnetic fields in the continuously synchronously pumped regime where this magnetometer operates to minimize the magnetic-equivalent fundamental noise at the standard quantum limit. Additionally, I have advanced the state of the art in implementation and optimization of supporting technologies to reduce the sum total non-magnetic technical noise an order of magnitude below the fundamental noise.

Through these advancements I have designed, built, and demonstrated a Bell-Bloom magnetometer capable of providing high performance in the full application space described above. I have achieved unprecedented single-channel scalar magnetic sensitivity and two-channel differential scalar magnetic sensitivity for a continuously-synchronously-pumped magnetometer at Earth-field-scale magnetic fields, significantly exceeding the sensitivity of other magnetometers operating in the same regime (Gerginov and S. K. S. Knappe 2017; H. Huang et al. 2015; Songsong Li et al. 2021). More explicitly, I have measured single-channel magnetic sensitivity of better than 10 $fT/\sqrt{Hz}$ with a photon shot noise limit of $3.5ft/\sqrt{Hz}$, comparable to the observed noise in many SERF magnetometers (I. Sulai et al. 2019) but in Earth-field-scale magnetic fields of 29 μT (exceeding SERF regime field limits by orders of magnitude: see Allred et al. 2002) albeit with significantly higher fundamental limits than these SERF magnetometers. The observed single-channel noise floor is comparable to the best published single-channel noise in any Earth-field-capable optically pumped atomic magnetometer (M. Limes et al. 2020), while the closed-loop -3 dB magnitude response bandwidth is improved by more than an order of magnitude. The observed single-channel magnetic noise is consistent with the limitations of the nonetheless very impressive electrical current source used to generate the bias field

(Twinleaf CSUA-1000) in combination with optical pump pulse phase error that is itself dominated by effects associated with the optical pump pulse logic circuitry (see Appendix A.1 for the cause and solution).

I have further demonstrated two-channel differential scalar sensitivity of 1 $fTcm^{-1}/\sqrt{Hz}$ on a 9 cm baseline, approximately an order of magnitude better than the differential scalar measurement performance achieved by M. Limes et al. 2020. This result approaches the performance of the best published differential scalar measurement (Sheng, S. Li, et al. 2013) but at four times the background magnetic field, using a significantly physically simpler apparatus with simpler processing and interpretation of photodetector output data, and on a longer baseline suitable for observation of signals originating at greater distance from the differential pair (I. A. Sulai et al. 2019).

Together with an undergraduate lab assistant, I have demonstrated the feasibility of a method patented by Dr. Thad Walker and myself (Tost, M. Bulatowicz, and T.G. Walker 2023; T.G. Walker and M.D. Bulatowicz 5 April 2022) for measuring vector components of the incident magnetic field using any scalar magnetometer. As a first step toward 3-axis vector component observation using this method, I have measured, theoretically investigated, and demonstrated the performance limitations of this approach in the context of our magnetometer for a single axis of vector component measurement. Finally, I have demonstrated a mechanism for high-sensitivity linearized detection of RF magnetic fields oscillating at frequencies much greater than the transverse spin polarization relaxation rate of the spins, in a manner which does not disrupt the ability to measure low-frequency magnetic field fluctuations, and I present an analysis in Chapter 3. To the best of my knowledge, this linear RF sensitivity result represents the first demonstration of RF sensitivity in a synchronously pumped magnetometer.

1.4 Thesis Organization and Presentation

This thesis is presented as follows. Chapter 2 provides the theory behind the basic operation of our synchronously pumped (Bell-Bloom) magnetometer, presents details of our

experimental apparatus, and goes into detail regarding the fundamental limits of magnetometer sensitivity. Chapter 2 details how to reach the fundamental limits through a combination of deterministic procedural optimization of the magnetometer physics and reduction of technical noise to negligible levels through appropriate design guidelines for the supporting electronic circuitry. Additionally, Chapter 2 presents the observed single-channel magnetic noise spectrum for the present work, consistent with the best published results for an Earth-field-capable optically pumped magnetometer (M. Limes et al. 2020) and demonstrating a two-channel differential scalar noise spectrum approaching the best published results for any differential optically pumped atomic magnetometer capable of operating in magnetic fields of greater than 5 μT (Sheng, S. Li, et al. 2013) but with a significantly simpler apparatus. Both the present work and the work of Sheng, S. Li, et al. 2013 approach the best published differential noise floor per unit physical separation distance of sensitive elements for a SERF magnetometer (H. Dang, A. Maloof, and M. Romalis 2010) but the work described in this thesis uses a longer, biomagnetically relevant (I. A. Sulai et al. 2019) baseline (distance between sensitive elements). In this segment of Chapter 2, factors affecting the limits of the observed differential signal are discussed, leading to recommendations for further improvements. Chapter 2 further discusses finite element modeling of the polarization distribution over the vapor cell volume as a function of incident optical pump characteristics such as intensity profile and the polarization-dependent optical pump photon scattering rate, the polarization-dependent relaxation rate of the spins, the optical intensity profile of the probe beam, and gas diffusion dynamics in the vapor cell. Such a model enables further optimization of magnetometer physics to approach full optimization of the fundamental noise limits for this technology. Chapter 2 concludes with recommendations for future work to incorporate further improvements in performance.

Chapter 3 presents an extension of this technology to closed-loop operation with a demonstrated tens of kHz -3dB response bandwidth, and further extension to detection of the vector components of the incident magnetic field. Detailed in Chapter 3 is a means of

self-calibration of the vector measurements with respect to the scalar field measurement, along with demonstration and characterization of the first steps toward full 3-axis vector measurement and the factors affecting the measurement uncertainty. Chapter 3 further presents detailed characterization of the feedback loop design and implementation. Also presented are the design and analysis of optimal signal filtering and high-performance algorithms for observation of the magnetic field vector components the vector component measurement is performed simultaneously with scalar measurement. Chapter 3 concludes with recommendations for future work demonstrating full three-axis sensitivity with further improvements in performance.

Chapter 4 presents the first demonstration (to the best of our knowledge) of RF sensitivity in a synchronously pumped magnetometer. Theory and measurements are presented detailing the physics of a naively-unexpected result: a slow linear phase modulation response (as opposed to the expected quadratic phase modulation response) to small-amplitude RF signals orthogonal to the bias field, oscillating near the natural Larmor precession frequency of the spins. In this chapter, the physics underlying the linear phase response of the spins is examined in detail, including a comparison between the developed theory and experimental results showing the superimposed linear and quadratic responses of the slow component of spin precession phase. This chapter presents further insight and measurement details for magnetic-noise-equivalent technical noise arising from technical-noise-induced phase error in the optical pump pulses along with a straightforward means of dramatically reducing the imposed single-channel noise limitations.

Finally, this thesis concludes with theory and discussion for future work: utilization of a second probe beam, orthogonal to the first, together with a single oscillating applied magnetic field to observe the precessing spin polarization vector as a function of time. Three-dimensional mapping of the spin polarization vector will enable one to deduce the direction of the incident magnetic field in the optical reference frame, thereby enabling calculation of the three-dimensional vector component solution without a need for the three orthogonal applied oscillating fields mentioned in Chapter 3.

Chapter 2

An all-optical scalar and differential scalar magnetometer with 10 $fT/\sqrt{Hz}$ and 1 $fT/cm/\sqrt{Hz}$ sensitivity in a 30μT field

2.1 Introduction

In this chapter, I present the basic theory of operation of a transversely synchronously pumped (Bell-Bloom: Bell and Bloom 1957; Bell and Bloom 1961) scalar magnetometer. I discuss the basic concepts behind the synchronously pumped magnetometer configuration with its co-propagating optical pump and probe beams, and discuss the experimental apparatus in detail with discussion of single-channel scalar measurement and two-channel differential scalar measurement. Next, I discuss physics-based optimization of the magnetometer response, demonstrating theoretically an optimized regime in which the magnetometer sensitivity is at approximately its minimum value of the standard quantum limit and insensitive to changes in alkali vapor number density; I demonstrate theoretically that the achievable open-loop response bandwidth of the spins in this regime is propor-

tional to the available optical pumping rate provided by the optical pump beam, while the fundamental noise at the standard quantum limit is independent thereof. I demonstrate conceptual architecture and theory for design of an optical polarimeter circuit with technical noise well below the photon shot noise of the probe laser along with a quantitative threshold associated with transimpedance gain resistor value at which technical noise will be equal to photon shot noise. I go into detail regarding physics-based procedural tuning of the magnetometer to optimize the magnetometer performance capability, and I present a finite element model which I have developed, providing opportunities for more-global optimization of the achievable standard quantum noise limits in simulation to inform future experimentation. Experimental results are presented for a 29 μT bias field, demonstrating a single-channel scalar measurement noise floor of approximately 10 $fT/\sqrt{Hz}$ and a differential scalar measurement noise floor of approximately 1 $fT * cm^{-1}/\sqrt{Hz}$ on a 9 cm baseline, equivalent to $6fT/\sqrt{Hz}$ single-channel noise. This chapter concludes with a discussion of the experimental results and recommendations for future work. Chapter 2 further includes and appendix showing a simplified phasor treatment of synchronous pumping.

2.1.1 Basic Theory of Operation

Measurement of magnetic fields by way of observation of spin precession in the magnetic field relies on fundamental properties of the spins of charged particles: any charged particle will exhibit both angular momentum and a magnetic moment. When subjected to a magnetic field $\mathbf{B}$, a particle with magnetic moment μ will experience a torque of magnitude $\mu|\mathbf{B}|$. Coupled with the property of spin, conservation of angular momentum dictates that the torque generates precession of the particle about the magnetic field; the frequency of precession is known as the Larmor frequency ω_L. In the case of the ^{87}Rb atoms used in the present work, a significant majority of the observed magnetic moment is contributed by the unpaired electron in the outer orbital of the atom ($5^2S_{1/2}$).The electron couples with the nucleus, exhibiting two possible ground states: electron and nucleus aligned or

anti-aligned. In either case, the angular momentum of the nucleus and electron together determine the observed precession frequency of the atomic spins in a magnetic field.

In each of the ground states, the total angular momentum F is the sum of the nuclear angular momentum I=3/2 and electron angular momentum J = (L + S) where L is the orbital angular momentum; L=0 for an S orbital and S=1/2 for an electron, so the available values of F = I + J are either 1 or 2. The magnetic sublevels m_F in the reference frame of the observed magnetic field denote the orientation of F relative to the magnetic field, and proceed in integer steps from -F to +F, each with a different energy E in the magnetic field. The energy spacing between magnetic sublevels gives rise to the observed spin precession frequency; spin precession is effectively a superposition of energy sublevels which oscillates at a frequency given by the fundamental relationship between energy and frequency $E = \hbar\omega$. To leading order:

$$\omega_L = \frac{\Delta E}{\hbar} = \gamma|\mathbf{B}|\Delta m_F = \frac{g_e \mu_B |\mathbf{B}| \Delta m_F}{\hbar(2I+1)} \tag{2.1}$$

where g_e is the Landé g-factor of the electron (approximately 2), μ_B is the Bohr magneton, Δm_F is the observed magnetic transition ($\Delta m_F = 1$ in this work) and I is the nuclear angular momentum in units of $\hbar$ (3/2 in the case of ^{87}Rb and 5/2 in the case of ^{85}Rb). The relationship between γ and the magnitude of $\mathbf{B}$ is based on fundamental physical constants and the angular momentum properties of the nucleus; therefore, by measuring ω_L one may deduce the magnitude of $\mathbf{B}$.

In an ensemble of spins, such as the warm ^{87}Rb vapor used in the present work, observation of ω_L requires coherent precession of a non-negligible fraction of the spins; the fraction of the spins exhibiting such coherence is called the spin polarization P. While some polarization is induced by way of the energy splitting generated by the magnetic field, this polarization is induced along the magnetic field and thus does not generate spin precession about that field. Further, the polarization is insufficient at Earth-field-scale magnetic fields to generate a useful precession signal. As such, this experiment requires a means of generating coherent spin precession about the magnetic field. Bell and Bloom

demonstrated more than 60 years ago (Bell and Bloom 1957; Bell and Bloom 1961) that coherent spin precession can be generated by modulation of optical pumping dynamics at a frequency near ω_L in a direction transverse to the magnetic field, and the spin precession can be optically observed; in the experiment described in this thesis, the optical pumping is achieved using an optical pump laser tuned detuned by a fraction of a linewidth from the ^{87}Rb D1 optical transition ($5^2S_{1/2} \rightarrow 5^2P_{1/2}$, approximately 795 nm wavelength) and the optical probe laser observing the spin precession is blue detuned from the ^{87}Rb D2 optical transition ($5^2S_{1/2} \rightarrow 5^2P_{3/2}$, approximately 780 nm wavelength).

The spin polarization $\mathbf{P} = \langle \mathbf{F} \rangle / |\mathbf{F}|$ of an ensemble of spins can naturally be decomposed into components parallel ($P_\parallel$) and perpendicular ($P_\perp$) to the magnetic field. The longitudinal (parallel) component of polarization does not experience a torque and therefore does not precess in the magnetic field; only the perpendicular component of polarization will precess and contribute to measurement of ω_L. Thus, all else equal, the condition $\mathbf{P} = \mathbf{P}_\perp$ will maximize the magnitude of the observable signal on the optical probe beam.

Synchronous (Bell-Bloom) Pumping

As mentioned above, Bell and Bloom demonstrated that spin precession about a magnetic field can be driven by modulation of optical pumping dynamics in a manner synchronous with the natural Larmor precession of the spins in the magnetic field. Modulation of pumping dynamics can be achieved through frequency modulation, polarization modulation (Grujic and Weis 2013), or amplitude modulation of the optical pump light. In the case of frequency modulation, the optical pump wavelength is modulated between a condition near or at resonance with an appropriate optical transition such as the D1 transition and a condition far off resonance (for example, S. J. Seltzer, Meares, and M. V. Romalis 2007). In the case of amplitude modulation, the wavelength is kept stable at a point near resonance with an appropriate optical transition while the optical intensity reaching the spins is modulated (for example, Gerginov and S. K. S. Knappe 2017). In each case, the optical pumping rate $R_{op}(t)$ includes a significant Fourier component at ω_L (or an integer

subharmonic thereof) oriented orthogonal to **B**.

The net effect of Bell-Bloom type optical pump modulation is to optically pump the spins in their rotating reference frame, while the optical pump itself is only along a single axis in the lab frame. Given an optical pump composed of a series of short optical pulses at the m^{th} subharmonic of ω_L along $\hat{R}$ and a magnetic field along $\hat{\Omega}$ with $\hat{B} \cdot \hat{R} = cos\theta$, one can define an orthonormal set of axes using $\hat{\Omega}$, $\hat{R} = cos(\theta)\hat{\Omega} + sin(\theta)\hat{\xi}$ and $\hat{\eta} = \hat{\Omega} \times \hat{\xi}$. With the optical pump repetition rate synchronized and syntonized relative to the natural Larmor precession frequency ω_L of the spins, the pulsed optical pump as observed in the lab frame will include Fourier components at

$$\mathbf{R}_{op}(t) = \sum_p A_p \left[\left(\hat{\Omega} cos\theta + \hat{\xi} sin\theta \right) cos\left(\frac{p}{m} \omega_L t \right) \right] \tag{2.2}$$

where the A_p coefficients are the amplitudes at the p^{th} harmonic of the optical pump repetition rate. For $P_\perp(t) = |P_\perp| e^{(\pm i \omega_L t)}$ in the $\hat{\xi} - \hat{\eta}$ plane, $R_{op}(t)$ will exhibit a co-rotating component and a counter-rotating component relative to the precessing spins: the spins are primarily pumped by the co-rotating component of the optical pump pulses at $p = m$; i.e. the component at ω_L. At Earth-field-scale magnetic fields for ^{87}Rb, the counter-rotating components of $R_{op}(t)$ and the $p \neq m$ harmonics of the optical pump pulse repetition rate are all many magnetic linewidths away from resonance with ω_L and can therefore be neglected. The co-rotating component at $p = m$, naturally, optically pumps the spins in their rotating reference frame, leading to net spin polarization and coherent precession of the spins about $\hat{\Omega}$.

Spin Polarization Relaxation

If the ensemble of spins is optically pumped to an initial spin polarization condition **P** and then allowed to freely evolve with time, the coherence will degrade over time t with a characteristic relaxation rate Γ such that $|\mathbf{P}| \propto exp[-\Gamma t]$. Notable contributors to this spin polarization relaxation in this experiment include Rb collisions with the vapor cell walls, collisions between the Rb atoms and the nitrogen buffer gas in the vapor cell, photon

scattering from the optical pump and probe beams, $^{87}Rb - ^{87}Rb$ spin-exchange and spin-destruction collisions, and $^{87}Rb - ^{85}Rb$ spin-exchange and spin-destruction collisions. Spin-exchange collisions contribute to relaxation of $P_\perp$ but not to relaxation of $P_\parallel$ because spin-exchange collisions conserve angular momentum; thus, $P_\parallel$ is unaffected in spin-exchange collisions. The total spin polarization relaxation rate is simply:

$$\Gamma_{total} = \sum_i \Gamma_i \tag{2.3}$$

where the Γ_i are the individual contributions from each of the spin polarization relaxation mechanisms.

Spin-Exchange Relaxation

A key concept in the understanding of spin-exchange relaxation lies in the difference between the $m_s = \pm 1/2$ ground states (F=1 and F=2 ground states of ^{87}Rb and, equivalently, the F=2 and F=3 ground states of ^{85}Rb). In each case, the magnetic moment of the electron dominates the total magnetic moment of the atom; meanwhile, the difference between ground states, as mentioned above, lies in relative alignment of the electron: spin up or spin down. These two ground states for each isotope of Rb with net nuclear spin therefore precess in opposite directions in the magnetic field; given a spin-exchange collision rate R_{SE}, the spins in each ground state will pick up an average phase between collisions of $+\omega_L/R_{SE}$ for one ground state and $-\omega_L/R_{SE}$. To the extent that Equation 2.1 holds, therefore, any pair of atoms in opposing ground states does not precess; spin exchange between these two spins will drive decoherence of the ensemble. The spin-exchange rate is of course not a uniform rate but simply an ensemble average; thus, between spin exchange collisions a random phase difference between spins in opposing ground states will be observed. Further, while this experiment utilizes isotopically enriched ^{87}Rb, there remains a small fraction of ^{85}Rb. As shown in Equation 2.1, the larger nuclear angular momentum (5/2) causes the ^{85}Rb to precess at a different rate than ^{87}Rb, and so the residual ^{85}Rb contributes to spin-exchange relaxation in this experiment but does not contribute

to measurement of ω_L for ^{87}Rb.

Spin relaxation and redistribution occurs not simply by collisions between alkali atoms in opposing ground states; any collision between alkali atoms other than those in which both atoms are in a "stretched state" (i.e. both atoms in the $|F = 2, m_F = 2\rangle$ state or both in the $|F = 2, m_F = -2\rangle$ state in ^{87}Rb) will conserve angular momentum but still redistribute the spin states (T. G. Walker and William Happer 1997). For instance, T. G. Walker and William Happer 1997 show explicitly one example of spin exchange between two ^{87}Rb atoms, each in a $|F, m_F\rangle = |2, 1\rangle$ state: see Figure 2.1 (copied from T. G. Walker and William Happer 1997 Figure 5a).

Spin-Destruction Collisions

When Rb atoms collide with each other or with N_2 molecules, there exists a finite probability that the collision will not conserve angular momentum (T. G. Walker and William Happer 1997). Further, when Rb atoms collide with the walls of the vapor cell they also lose polarization. The gas-phase spin-destruction rates for ^{87}Rb are (Chen et al. 2007)

$$\Gamma_{SD,Rb-Rb} = n_{Rb} * 4.2 * 10^{-13} cm^3/s \tag{2.4}$$

$$\Gamma_{SD,Rb-N_2} = n_{N_2} * 1.3 * 10^{-25} cm^3/s * T^3 \tag{2.5}$$

where n_{Rb} and n_{N_2} are the number densities of rubidium and nitrogen, respectively, and T is temperature in Kelvin. Meanwhile, collisions with the vapor cell walls contribute to the ensemble average spin polarization relaxation rate by way of diffusion of the Rb spins through the buffer gas. The contribution to spin polarization relaxation can be calculated using the diffusion equation:

$$\frac{dP}{dt} = D\nabla^2 P \tag{2.6}$$

where D is the diffusion coefficient of Rb in N_2 and P is the Rb polarization. Boundary conditions include zero polarization at the vapor cell walls (T. G. Walker and William Happer 1997). Calculation of the resulting relaxation rate Γ_{wall} can be performed in an

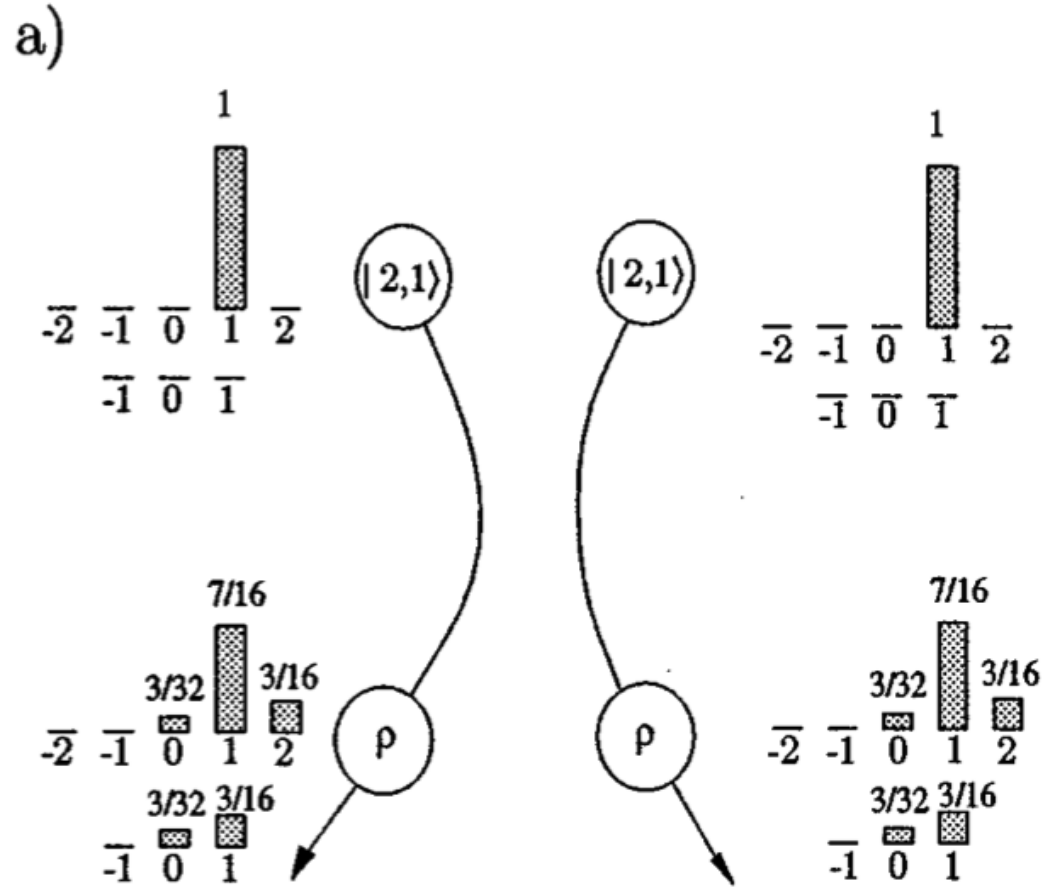

Figure 2.1: Illustration of the results of a spin-exchange collision from T. G. Walker and William Happer 1997 for two alkali atoms with I=3/2 such as ^{87}Rb, each initially in the $|F, m_F\rangle = |2, 1\rangle$ state. The total angular momentum of the pair of spins is conserved, but the magnetic sublevels are not. Of particular concern for spin-exchange relaxation, a significant fraction of spin-exchange collisions in this example result one or both spins transitioning to the F=1 hyperfine level. The two hyperfine (F) levels precess in opposite directions, leading to decoherence of the spin ensemble precession.

approximate fashion by modeling the nominally cylindrical vapor cell with residual fill stem as simply a perfect cylinder; further simplification comes from modeling only the lowest diffusion mode. In this approximation, for a cylinder of length l and diameter d, with a spin relaxation slowing-down factor of q,

$$\Gamma_{wall} \approx Dk^2 q = D\left(\frac{(l+d)\pi}{2dl}\right)^2 q \tag{2.7}$$

which makes use of the characteristic spatial wavevector $k = \pi/2x$ for the lowest mode in the radial direction and the axial direction, where x is the linear dimension along that direction. In this experiment, $d = l$, resulting in

$$\Gamma_{wall} \approx qD\frac{\pi^2}{l^2} = qD_0\frac{n_{N_2}T^{3/2}}{n_{0,N_2}T_0^{3/2}} \tag{2.8}$$

with diffusion coefficient $D_0 = 0.16cm^2/s$ at $n_{0,N_2} = 1$ amagat and 273 Kelvin (Franz and Volk 1976). At the present vapor cell buffer gas number density of approximately 0.8 amagat and temperature of approximately 358 Kelvin, this yields an approximate relaxation rate of $\Gamma_{wall} = 1.9$ q. The multiplication by the slowing-down factor in this case indicates the relaxation of not only the electron spin but also the nuclear spin (T. G. Walker and William Happer 1997).

Optical Pumping

Detailed calculations of optical pumping and spin relaxation can be found in (William Happer 1972) and (W. Happer and Wijngaarden 1987), including effects of both the ground and excited states along with various mechanisms of spin polarization relaxation. Full treatment must take into account the hyperfine splitting and the m_F levels of the atoms; however, the calculations can be greatly simplified when the broadened optical transition linewidth is greater than the hyperfine splitting. In this experiment, as mentioned above the N_2 buffer gas number density is approximately 0.8 amagat; N_2 exhibits a broadening coefficient of approximately 17.8 GHz/amagat for the $87Rb$ D1 optical transition and 18.1

GHz/amagat for the ^{87}Rb D2 transition (M. V. Romalis, Miron, and Cates 1997). The collisional broadening effects alone account for approximately 14 GHz optical linewidth for each transition, approximately double the 6.835 GHz hyperfine splitting (Steck 2003). Therefore, the various energy levels are unresolved for the purposes of optical pumping in this experiment.

Recall that in this experiment circularly polarized light near the ^{87}Rb D1 optical transition ($5^2S_{1/2} \rightarrow 5^2P_{1/2}$, approximately 795 nm wavelength) optically pumps the spins. For an atom to absorb a pump photon, it must absorb not only its energy but also its angular momentum; angular momentum selection rules therefore dictate that only one of the electron magnetic sublevels ($m_s = -1/2$) can absorb σ^+ circularly polarized light while the other ($m_s = +1/2$) cannot. Rapid collisions between Rb atoms in the excited state with each other and with N_2 molecules result in rapid excited-state mixing of the m_s levels. The excited-state Rb atoms are rapidly quenched through non-radiative energy transfer with N_2 although some finite radiative quenching remains (Rosenberry et al. 2007). The non-radiative quenching process preserves the angular momentum and the m_s level of the excited state atom; thus, half of the atoms for each pumping cycle end up in the $m_s = +1/2$ ground state and the average angular momentum added to each atom per pumping cycle is 1/2 in units of $\hbar$. A diagram of this process is shown in Figure 2.2.

The nuclear spin, meanwhile, is not randomized by excited state collisions and tends to become polarized via the hyperfine interaction:

$$\left(\frac{d\langle \mathbf{F} \rangle}{dt}\right)_{op} = \frac{R_{op}}{2}(1 - \mathbf{s} \cdot \mathbf{P}_e) - \frac{\Gamma_e}{2} P_e \tag{2.9}$$

where $\mathbf{P}_e = 2\langle \mathbf{S} \rangle$ is the electron spin polarization in the reference frame of the optical pump, $\mathbf{s}$ is the angular momentum of the optical pump photons ($|\mathbf{s}| = 1$ for a σ^+ photon, R_{op} is the optical pumping rate (the rate at which the atoms will absorb pump photons in the zero-polarization limit), and Γ_e is the electron spin polarization relaxation rate. The

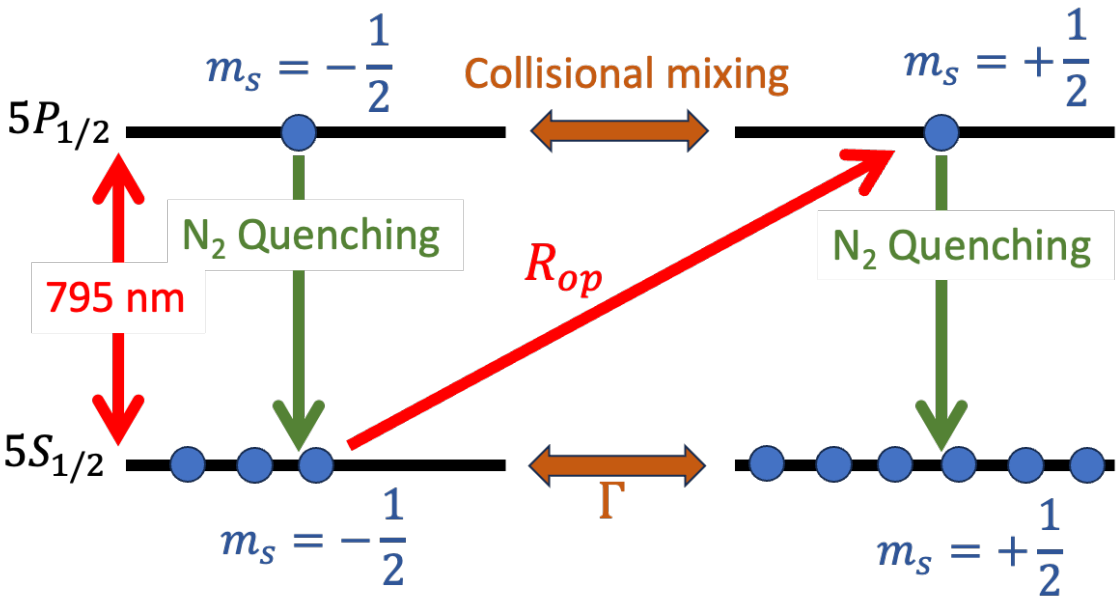

Figure 2.2: Diagram of the optical pumping scheme for this experiment. At thermal equilibrium, the ground state ($5S_{1/2}$) populations in the $m_s = +1/2$ and $m_s = -1/2$ sublevels of the ensemble of ^{87}Rb atoms are approximately equal. Circularly polarized photons R_{op} in the σ^+ polarization state ($\mathbf{s} = 1$), approximately resonant with the ^{87}Rb D1 transition ($\approx 795nm$) drive ground state electrons in the $m_s = -1/2$ sublevel to the excited state $5P_{1/2}, m_s = +1/2$ excited state. Selection rules forbid excitation of $m_s = +1/2$ ground state electrons from absorbing σ^+ photons, so only the $m_s = -1/2$ electrons are excited. Rapid collisional mixing in the excited state places approximately half the excited state electrons into each of the m_s sublevels, and non-radiative quenching through energy transfer to the N_2 buffer gas drives the atoms back to the ground state without altering their respective sublevels. Each photon absorption, therefore, adds on average $1/2\ \hbar$ of angular momentum to the ensemble. Spin polarization relaxation Γ drives the ensemble back toward thermal equilibrium.

optical pumping rate is given by

$$R_{op} = \Phi_{op}\sigma(\nu_{op}) = \Phi_{op} r_e c f_{D1} \frac{\Gamma_\nu/2}{(\nu_{op} - \nu_{D1})^2 + (\Gamma_\nu/2)^2} \tag{2.10}$$

where $\Phi_{op} = IA/(h\nu_{op})$ is the optical pump photon flux for an optical pump of average intensity I and cross sectional area A with Planck's constant h and pump optical frequency ν_{op}, $\sigma(\nu_{op})$ is the interaction cross section, r_e is the classical electron radius, c is the speed of light, $f_{D1} \approx 1/3$ is the oscillator strength of the D1 transition, ν_{D1} is the D1 optical transition resonance frequency, and Γ_ν is the excited state relaxation rate of the D1 transition including all broadening effects. In steady state, then,

$$P_e = \frac{\langle R_{op} \rangle}{\langle R_{op} \rangle + \Gamma} \tag{2.11}$$

in the limit where $\mathbf{s} \cdot \mathbf{P}_e = \mathbf{P}_e$; Γ is the spin polarization relaxation rate.

Spin Precession

In the presence of a magnetic field $\vec{\Omega} = \gamma \mathbf{B}$ the angular momentum $\mathbf{F}$ of the ensemble will evolve with time according to the Bloch equation:

$$\frac{d\mathbf{F}}{dt} = \vec{\Omega} \times \mathbf{F} - (R_{op}(t) + \Gamma_{\parallel,\perp})\mathbf{S} + \frac{\mathbf{R}_{op}(t)}{2} \tag{2.12}$$

where $\Gamma_{\parallel,\perp}$ is the electron randomization rate as applicable to the parallel or perpendicular components of spin polarization relative to $\vec{\Omega}$, and it is assumed that the time-dependent optical pumping rate $R_{op}(t)$ has an appropriate form for D1 transition optical pumping of ^{87}Rb at high pressure.

Under the assumption that the details of the nuclear spin evolution can be described by a simple proportionality $\mathbf{F} = q\mathbf{S}$, one may generate a good approximation of the time evolution of the spin in this experiment. It is also natural to split the angular momentum into components parallel and perpendicular to the magnetic field, and to treat these components separately. With the optical pump propagating along $\hat{R}$ and the

magnetic field along $\vec{\Omega}$,

$$q\frac{dS_{\|}}{dt} = -(R(t) + \Gamma_{\|})S_{\|} + \cos\theta\frac{R(t)}{2} \tag{2.13}$$

where $\hat{R} \cdot \hat{\Omega} = cos\theta$; one may define $\hat{R} = cos\theta\hat{\Omega} + sin\theta\hat{\xi}$ and a third orthonormal vector $e\hat{t}a = \hat{\Omega} \times \hat{\xi}$. The steady-state polarization parallel to the magnetic field is

$$P_{\|} = 2S_{\|} = \frac{\langle R_{op}\rangle cos\theta}{\langle R_{op}\rangle + \Gamma_{\|}} \tag{2.14}$$

which exhibits no sensitivity to the magnitude of the magnetic field and is therefore not useful for scalar magnetometry.

The transverse spin components, however, do precess about the magnetic field as described in Equation 2.12 and can be conveniently expressed in phasor form $S_{+} = S_{\xi} + iS_{\eta} = S_{\perp}e^{i\alpha}$. Substituting this into Equation 2.12 and taking the real part, the magnitude of the transverse component of spin obeys

$$q\frac{dS_{\perp}}{dt} = -(\Gamma_{\perp} + R(t))S_{\perp} + \frac{1}{2}cos\alpha R(t)sin\theta \tag{2.15}$$

As will be shown below, the phase α of the transverse spin obeys $\alpha = \omega t + \delta$. In this experiment, the optical pump pulses are localized in time about $\omega t = 2\pi$w with integer w. In the limit that the optical pumping rate $\langle R_{op}(t)\rangle$ and relaxation rate $\Gamma_{\perp}$ are small compared to the Larmor frequency, the optical pumping rate and relaxation rate can be replaced by their time averages.

As will be shown shortly, pulsed amplitude modulation of the optical pumping light wherein the optical pumping light pulses are of short duration (much less than $2\pi/\omega_L$) and of negligible intensity between pulses has an inherent advantage over other amplitude modulation schemes such as sinusoidal amplitude modulation. The optical pumping rate along $\hat{R}_{op}$ is independent of spin orientation, while in the rotating reference frame of the spins, the polarization of the optical pump is $s(\hat{s} \cdot \hat{S})$ where s is the polarization of the optical pump photons ($s = 1$ along $\hat{R_{op}}$ for σ^{+} circularly polarized pump photons)

and $2\langle S\rangle\hat{S} = \mathbf{P}$ is the spin polarization vector of the ensemble of precessing spins. The direction of the optical pump is held fixed in the lab frame in this experiment, and so the time-average polarization of the optical pump in the rotating reference frame of the spins is

$$\langle \hat{s} \cdot \hat{S} \rangle = \frac{\omega_L}{2\pi} \int_0^{\frac{2\pi}{\omega_L}} s \frac{\mathbf{R}_{op}(t)}{|\mathbf{R}_{op}(t)|} \cdot \hat{S} dt \tag{2.16}$$

In the simple sinusoidal amplitude modulation example where the optical pump photon flux is modulated at $|R_{op}(t)| = \langle R_{op}\rangle(1 + cos(\omega_L t))$, it becomes clear that $\hat{s_\perp} \cdot \hat{S_\perp} = \frac{1}{2}(cos\omega_L t + cos^2\omega_L t)$, which averages to $\langle \hat{s} \cdot \hat{S} \rangle = 1/4$. Hence, in the case of sinusoidal amplitude modulation, the steady-state magnitude of $P_\perp$ is

$$P_{\perp,sine} = \frac{1}{4} sin(\theta) \frac{\langle R_{op}\rangle}{\langle R_{op}\rangle + \Gamma_\perp} \tag{2.17}$$

where $P_{\perp,sine}$ is the magnitude of $P_\perp$ in the case of sinusoidal amplitude modulation of the optical pump and it is clear that sinusoidal amplitude modulation of the optical pump cannot fully polarize the spins even when the optical pump modulation is on resonance with the natural Larmor precession frequency of the spins.

For short pulses with fractional duty cycle $d \ll 1$ (i.e. time duration $2\pi d/\omega$ for any given pump pulse), the optical pumping rate will exhibit a time average of $\langle cos(\alpha) R_{op}(t)\rangle = sinc(\frac{d}{2}) cos\delta \langle R_{op}\rangle \approx cos\delta \langle R_{op}\rangle$. Similar to the expression for the component of polarization parallel to the magnetic field, the steady-state magnitude of the transverse polarization will be

$$P_\perp = 2S_\perp = cos(\delta) sin(\theta) \frac{\langle R_{op}(t)\rangle}{\langle R_{op}\rangle + \Gamma_\perp} \tag{2.18}$$

demonstrating that in principle the atoms can become fully polarized using synchronous pumping with short-duty-cycle pulses. When the optical pump pulse repetition rate ω is equal to the Larmor precession frequency Ω, the spins align with the optical pumping light once per cycle and $cos\delta \to 1$. Pumping with short synchronized pulses of pump light transverse to the magnetic field is therefore as effective at generating spin polarization as the more typical optical pumping along the magnetic field direction.

The phase of the transverse spin similarly obeys

$$\frac{d\alpha}{dt} = \Omega - sin\theta \frac{R_{op}(t) sin\alpha}{2qs_{\perp}} \tag{2.19}$$

and the phase shift relative to the optical pump pulses obeys

$$\frac{d\delta}{dt} = \Omega - \omega - \Gamma_2 \tan\delta \tag{2.20}$$

where $\Gamma_2 = (\Gamma_{\perp} + \langle R_{op} \rangle)/q$ is the slowed transverse spin relaxation rate. In this work, the observable quantity is

$$\mathbf{P} \cdot \hat{R} = P_{\parallel} cos\theta + P_{\perp} cos(\omega t + \delta) = \frac{\langle R_{op} \rangle}{\langle R_{op} \rangle + \Gamma_{\perp}} (cos^2(\theta) + sin^2(\theta) cos(\delta) cos(\omega t + \delta)) \tag{2.21}$$

and demodulation of the result using $sin(\omega t)$ gives the classic dispersion lineshape

$$\langle \mathbf{P} \cdot \hat{R} sin(\omega t) \rangle = P_{max} cos(\delta) sin(\delta)/2 = \frac{P_{max}}{2} \frac{(\Omega - \omega)\Gamma_2}{(\Omega - \omega)^2 + \Gamma_2^2} \tag{2.22}$$

as one would expect.

Light Narrowing

The phenomenon of light narrowing is a means of suppressing spin relaxation by pumping a significant fraction of the spins into a "stretched state" ($|m_F| = F = 2$ for ^{87}Rb). As described in Section 2.1.1, spin-exchange collisions will preserve the total angular momentum, and so spin-exchange between a pair of atoms each in the same $m_F = 2$ state will exhibit no overlap with the opposing ground hyperfine level ($F = 1$) and not result in spin-exchange relaxation. Given this spin-exchange relaxation suppression effect, the net spin-exchange relaxation rate is simply proportional to (1-P). A consequence of driving toward a condition in which a significant fraction of the spins is in a stretched state is that the optical pumping rate must support a high polarization (see Equation 2.35), while the total transverse spin relaxation rate Γ_2 includes contributions from the optical pump

beam (Section 2.1.1). As such, in the continuously synchronously pumped regime as in this experiment, a balance must be struck between suppression of spin-exchange relaxation and decoherence induced by a high optical pump rate (also known as optical pump power broadening). The topic of optimization of magnetometer physics based on these effects will be covered in more depth in Section 2.4.1.

Detection using Faraday Rotation

In this work, the observable quantity $\mathbf{P} \cdot \hat{R}$ is detected using an optical probe beam composed of linearly polarized light, detuned from the D2 ($5S_{1/2} \rightarrow 5P_{3/2}$) optical transition, approximately 780 nm, co-propagating with the optical pump beam. The linear polarization state is an equal superposition of σ^+ and σ^- circular polarization states; the relative phase of these two states determines the angle of linear polarization. As an example, consider the normalized Jones vector representation $\vec{J}_H$ of horizontal linear polarization as compared to right-hand and left-hand circular polarization states, $\vec{J}_{RHC}$ and $\vec{J}_{LHC}$, respectively:

$$\vec{J}_H = \begin{vmatrix} 1 \\ 0 \end{vmatrix} \quad \vec{J}_{RHC} = \frac{1}{\sqrt{2}} \begin{vmatrix} 1 \\ \text{-i} \end{vmatrix} \quad \vec{J}_{LHC} = \frac{1}{\sqrt{2}} \begin{vmatrix} 1 \\ \text{i} \end{vmatrix} \tag{2.23}$$

indicating that the normalized representation of horizontal linear polarization is simply the normalized sum of left-hand and right-hand circular polarization states (i.e. left-hand summed with right-hand circular polarization at equal phase). Similarly, the normalized representation of vertical linear polarization is the normalized difference of left-hand and right-hand circular polarization states (left-hand summed with right-hand polarization at π relative phase). Clearly, then, an equal sum of left-hand and right-hand circular polarization at arbitrary phase produce linear polarization at any arbitrary angle.

As described above in Section 2.1.1, σ^+ photons interact with $m_s = -1/2$ electrons; similarly, σ^- photons interact with $m_s = +1/2$ electrons. In the reference frame of the optical probe beam, the proportion of $m_s = +1/2$ and $m_s = -1/2$ electron spins is

described by $\mathbf{P} \cdot \hat{R}$ (Equation 2.21). With the optical probe beam detuned from resonance, a primary effect of the interaction between the spin ensemble and the probe beam is an index of refraction difference for the σ^+ and σ^- components of the optical probe beam, proportional to $\mathbf{P} \cdot \hat{R}$. As the optical probe beam propagates through the alkali vapor, then, the linear polarization state rotates through an angle ϕ. For this experiment, the 14 GHz collisional broadening induced by the high buffer gas number density of 0.8 amagat keeps the hyperfine structure from being resolved; as mentioned above, the separation in energy between the $F = 1$ and $F = 2$ manifolds is approximately 6.835 GHz (Steck 2003). Neglecting the unresolved hyperfine structure, ϕ is given by (M. V. Romalis, Miron, and Cates 1997)

$$\phi = -\frac{1}{2} l r_e c f n D(\nu) \mathbf{P} \cdot \hat{R} = -l r_e c f n \frac{\Delta}{\Gamma_{\nu,pr}(1 + 4\Delta^2/\Gamma_{nu,pr}^2)} \mathbf{P} \cdot \hat{R} \tag{2.24}$$

where l is the path length through the polarized alkali vapor, r_e is the classical electron radius, c is the speed of light, f is the oscillator strength of the D2 transition, n is the number density of the ^{87}Rb atoms in the vapor phase, $\Gamma_{\nu,pr}$ is the D2 excited state relaxation rate, and Δ is the detuning of the optical probe from resonance. The expression for ϕ can be derived using the methods described in *Electric-Dipole Polarizabilities of Atoms, Molecules, and Clusters* 1997.

Polarization rotation of the optical probe beam can be measured by using a balanced polarimeter consisting of a polarization beamsplitter such as a Wollaston prism and a pair of photodetectors arranged to collect the ordinary and extraordinary components of the incident light (also known as the S and P polarization components). In a balanced polarimeter, the orientation of the polarization beamsplitter is carefully arranged to generate an equal incident photon flux on each of the two photodetectors for an un-rotated optical probe beam. The photon flux at the detectors generates electrical current when operating the photodetectors in photoconductive mode, as in this experiment; the differential

photocurrent δI is given by

$$\delta I = \eta\Phi_{pr}(sin^2(\phi + \frac{\pi}{4}) - sin^2(\phi - \frac{\pi}{4})) = \eta\Phi_{pr}sin(2\phi) \tag{2.25}$$

where η is the quantum efficiency of the photodetector. I have designed and built a high-performance custom photodetector preamp circuit (transimpedance amplifier pair and pair of difference amplifiers) for this experiment, providing for photocurrent measurement dominated by photon shot noise in the optical probe beam (Appendix A.2) in addition to designing a custom physical polarimeter apparatus consisting of custom mount containing a Wollaston prism, a condensing lens, and a matched pair of photodetectors, shown diagrammatically in Figure 2.5.

Fundamental Noise Limits

Optically pumped atomic magnetometers exhibit three major fundamental noise sources (Budker and Kimball 2013): photon shot noise δB_{PSN}, quantum projection noise δB_{QPN}, and probe AC Stark shift noise, also known as light shift noise δB_{LSN}. The photon shot noise arises from statistical counting noise in the number of photons reaching the photodetector; for Φ_{pr} photons reaching the photodetector in a measurement time period (resulting in $\eta\Phi_{pr}$ electrons emitted in photoconductive mode), the noise power is simply equal to Φ_{pr} ($\eta\Phi_{pr}$ electron number noise power). The amplitude of the corresponding photon shot noise limit $\delta\phi$ to the measurement of ϕ is therefore:

$$\delta\phi = \frac{1}{\sqrt{2\eta\Phi_{pr}}} \tag{2.26}$$

where Equation 2.25 has been used to express the photon shot noise on a per square root Hz basis with the approximation that $sin(2\phi) = 2\phi$ in the limit that ϕ is small. The phase response δ of the spins to oscillating magnetic fields of increasing frequency f_{det} is

well-approximated by

$$\delta(f_{det}) = \frac{\delta(0)}{\sqrt{1 + \frac{f_{det}^2}{\Gamma_2^2/\pi^2}}} = \frac{\delta(0)}{\sqrt{1 + f_{det}^2 \pi^2 T_2^2}} \tag{2.27}$$

wherein it is clear that the spin precession phase response follows the same frequency dependence pattern as a simple resistor-capacitor (RC) low-pass filter, with a characteristic frequency Γ_2/π in Hz. This relationship follows naturally from the high-frequency limit of phase accumulation for the spins: for a magnetic field oscillation $B_{\omega_B} cos(\omega_B t)$ where $\omega_B \gg \Gamma_2$

$$\delta(t) = \int \gamma B_{\omega_B} cos(\omega_B t) dt = \frac{\gamma B_{\omega_B} sin(\omega_B t)}{\omega_B} \tag{2.28}$$

which is simply a restatement of Equation 2.1.

Combining Equations 2.21, 2.24, 2.26, and 2.27 leads to an expression for the photon shot noise in magnetic field terms. In the case where $\hat{R} \cdot \hat{\Omega} = 0$ (i.e. $P = P_\perp$):

$$\delta B_{PSN}(f_{det}) = \frac{\Gamma_2 \Gamma_{\nu,pr}^2 (1 + 4\frac{\Delta^2}{\Gamma_{\nu,pr}^2}) \sqrt{1 + f_{det}^2 \pi^2 T_2^2}}{l r_e c f n \Delta P \gamma \sqrt{2\eta \Phi_{pr}}} \tag{2.29}$$

where terms are as defined above.

Quantum projection noise is similarly dependent on the relaxation rate and number density, along with the volume V of spins interacting with the probe beam, and the gyromagnetic ratio (Alem, Sauer, and M.V. Romalis 2013; Ledbetter et al. 2008):

$$\delta B_{QPN} = \frac{1}{\gamma} \sqrt{\frac{\Gamma_2}{nV}} = \frac{1}{\gamma} \sqrt{\frac{\Gamma_2}{N}} \tag{2.30}$$

with total number of spins N being sampled by the optical probe beam.

Additional noise is contributed by quantum fluctuations in the polarization state of the optical probe beam (Ledbetter et al. 2008). This noise is calculated based on the optical intensity (photon flux and cross sectional area A), with other terms as defined above: this noise occurs along the probe direction ($\hat{x}$) and generates an effective magnetic field

noise based on the scalar magnetic field deviation generated by the resulting AC Stark shift noise; the AC Stark energy shift modifies the splitting between m_F levels, and is therefore indistinguishable from a magnetic field and will exhibit its own shot noise based on the photon shot noise of the σ^+ and σ^- components of the optical probe beam linear polarization state. To leading order, this AC Stark shift noise (also known as "light shift noise" is given by (Ledbetter et al. 2008):

$$\delta B_{LSN} = \frac{r_e c f D(\nu)\sqrt{2\Phi_{pr}}}{(2I+1)\gamma A}\hat{R}\cdot\hat{\Omega} \tag{2.31}$$

where $D(\nu) = (\nu - \nu_0)/((\nu-\nu_0)^2 + (\Gamma_{\nu,pr}/2)^2)$ with probe beam optical frequency ν and D2 optical transition resonance frequency ν_0. However, as noted above $\hat{R}\cdot\hat{\Omega} \rightarrow 0$ in this experiment, and so AC Stark shift noise does not meaningfully contribute to the total noise in this experiment but can be a meaningful source of noise in a real-world application where $\hat{R}\cdot\hat{\Omega}$ is rarely negligible.

Measurement of Alkali Number Density

As shown in Equations 2.29 and 2.48, alkali number density n is an important parameter for calculation of the fundamental limits of magnetometer performance. In this experiment, alkali number density is measured in the low probe intensity limit using the relationship

$$Exp[n\sigma_0 l] = \frac{T_{off}}{T_{on}} \tag{2.32}$$

where σ_0 is the on-resonance scattering cross section of ^{87}Rb for the broadened D_2 optical transition, T_{on} is the probe transmission through the alkali vapor in the on-resonance condition, and T_{off} is the probe transmission through the alkali vapor in the far-detuned condition where probe scattering is approximately zero. In this experiment, the optical depth $OD = n\sigma_0 l$ of the vapor cell is sufficiently low to allow reasonable direct use of this method rather than requiring a curve fit of absorption versus wavelength of the probe beam by way of the relationship between cross section and wavelength described in Equation

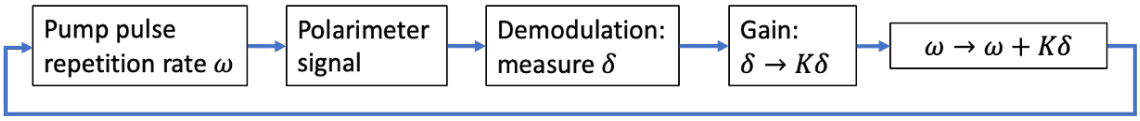

Figure 2.3: Block diagram for closed-loop feedback. Optical pump pulses are input to the magnetometer at a repetition rate ω; the response of the spins is measured by the polarimeter and demodulated (for example, using a lock-in amplifier referenced to ω) to output a signal proportional to δ. A gain stage takes the signal and multiplies it by a transfer function K. The result is then used to modify ω such that $\delta \rightarrow 0$.

2.10. Using the method described in Equation 2.32, I measure $n \approx 2 * 10^{12} cm^{-3}$.

Closed-Loop Feedback Basics

As shown in Equation 2.22, in the limit of small δ the demodulated response of the ensemble of spins in steady state is proportional to the phase difference δ between the optical pump pulse repetition rate and the observed spin polarization signal on the polarimeter; as δ continues to increase, the linearity degrades. Maximum magnetic field sensitivity, therefore, is achieved at $\omega \rightarrow \Omega$; in an unshielded environment, closed-loop feedback designed to drive $\delta \rightarrow 0$ by way of modifying ω, then, will keep the magnetometer operating in its most sensitive and linear-response regime. A conceptual block diagram for closed loop feedback from the perspective of the electronics is shown in Figure 2.3. The topic of closed-loop feedback will be covered in more depth in Chapter 3.

2.2 Present Work

Brief Background

With collaborators, we recently extended the synchronously pumped atomic magnetometer concept to include a scalar and differential scalar magnetometer capable of operating with high sensitivity in earth's field with the goal of improving performance to levels sufficient for biomagnetic imaging in an unshielded environment (A. R. Perry et al. 2020). In the present work, I have achieved repeatable, significantly improved performance over the work described in A. R. Perry et al. 2020, combined with significant simplification of

the system. In (A. R. Perry et al. 2020), similar to the work described in Sheng, A. R. Perry, et al. 2017, the differential magnetic sensitivity was achieved by way of optical subtraction (Figure 2.4). A single optical probe beam passed through a first magnetically sensitive volume (zone 1, labeled Z_1 in Figure 2.4), picking up a first polarization rotation ϕ (Equation 2.37). Reflection off a pair of dielectric mirrors was then used to drive $\phi \rightarrow -\phi$ and displace the optical probe beam to pass through the second sensitive zone, after which the probe beam passed through a second sensitive volume (zone 2; Z_2 in Figure 2.4) nominally identical to the first and optically pumped synchronously with the first: at zero magnetic gradient (equal magnetic field magnitude for each of the two zones) the probe nominally picks up another rotation of θ for a net zero polarization rotation. A non-zero net polarization rotation of the optical probe observed in A. R. Perry et al. 2020, then, indicates a differential magnetic field between the two zones. The underlying perception driving this operational concept was that electrical subtraction of the signals of two zones would be unable to generate a differential detection noise in the range of single digit to tens of $\frac{fT}{cm\sqrt{Hz}}$.

Contrary to this perception, if the technical noise is well below the photon shot noise limit, electrical subtraction can provide the same differential measurement performance limits as optical subtraction. Reaching the photon shot noise limit for a detector observing a mW-scale optical signal simply requires appropriately designed detection electronics: Appendix A.2 demonstrates that such a design is straightforward and solidly based in fundamental physics.

In the limit of a far-off-resonance optical probe (negligible optical absorption in the alkali vapor) a single optical probe beam that passes through two detection zones will generate the same total photocurrent as in the case of a split probe beam passing through each of two zones individually. With identical total photocurrent and all else equal, the two-channel differential photon shot noise will be the same for both configurations; meanwhile, the single-channel photon shot noise can be reduced significantly compared to A. R. Perry et al. 2020, wherein a small fraction of the optical probe light was split off from the

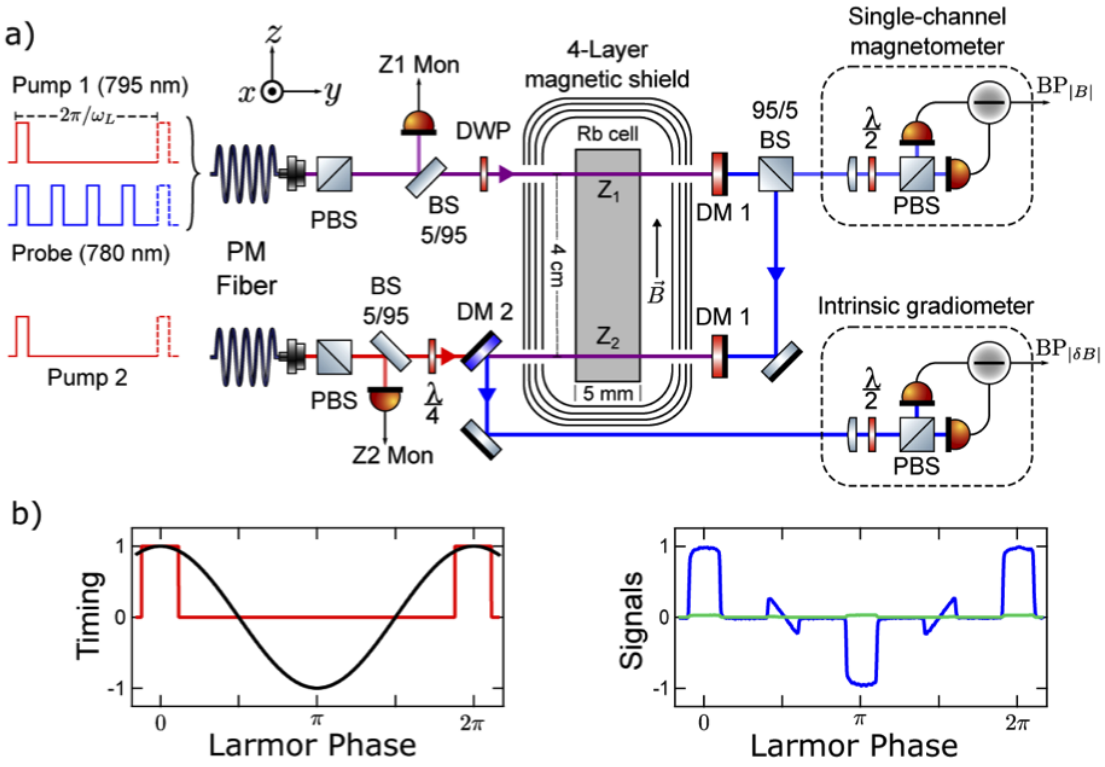

Figure 2.4: Figure 1 from A. R. Perry et al. 2020. (a) Optical layout showing the two interrogation regions probed by a single optical probe beam and pumped by synchronous optical pump pulses. Red lines indicate optical pump ($\approx$ 795 nm), blue lines indicate optical probe ($\approx$ 780 nm), and purple represents co-propagating or counter-propagating pump and probe light. Optical components include PBS (polarization beam splitter), DM (dichroic mirror), BS (non-polarizing beam splitter), $\lambda/2$ (half wave plate), DWP (dichroic wave plate; circularly polarizes 795 nm and leaves 780 nm linearly polarized), and photodetectors (Z_1 Mon, Z_2 Mon, and differential generating $BP_{|B|}$ and $BP_{|\delta B|}$ signals for optical intensity monitoring of the combined pump and probe, second pump, scalar field, and differential scalar field, respectively. (b) Notional timing diagram of optical pumping versus Larmor phase of the spins, and actual photodetector signal from $BP_{|B|}$ (blue) and $BP_{|\delta B|}$ (green) respectively. The optical pump is pulsed once per Larmor cycle and the optical probe is pulsed 4 times per Larmor cycle in this example.

main probe beam after it had passed through zone 1 (see Figure 2.4); this small fraction of the optical probe light was sent to a second polarimeter for measurement of the scalar magnetic field, significantly degrading the photon shot noise limit for scalar magnetic field measurement as compared to the present work. Further, the present configuration uses fewer optical elements than A. R. Perry et al. 2020, thereby simplifying the apparatus.

As described above and in (A. R. Perry et al. 2020), the underlying principles of this synchronously pumped magnetometer scheme can be described by an ensemble of atomic spins, polarized by a periodically pulsed, circularly-polarized pumping laser beam propagating along the axis $\hat{R}$. During the time interval between pump pulses, the polarized atoms precess about the external magnetic field $\mathbf{B}$ at the Larmor precession frequency (Equation 2.1); the experiment described herein probes $\Delta m = 1$ magnetic transitions, so this simplifies to

$$\omega_L = \gamma |\mathbf{B}| \tag{2.33}$$

As described in Section 2.1.1, the probability of absorbing photons from the pump laser (i.e. the optical pump photon scattering rate) is proportional to $(1 - P_R)$ where P_R is the component of the spin polarization along the pump axis. For small deviations of the pump pulse repetition frequency ω about ω_L, there is an enhanced absorption of photons which brings the instantaneous spin polarization closer into alignment with the light. The net result is spin precession at the pulse repetition frequency but with a phase shift δ between the spin precession and the pump pulses driving that precession.

Recall from Section 2.1.1 that the spin precession vector $P_R(t)$ can be broken down into components parallel ($P_\parallel$) and perpendicular ($P_\perp$) to the magnetic field B:

$$P_R(t) = P_\parallel \cos(\theta) + P_\perp \sin(\theta) \cos(\omega t + \delta) \tag{2.34}$$

where $\cos(\theta) = \hat{B} \cdot \hat{R}$. The relevant observable for scalar field magnitude is the component of the atomic spin polarization perpendicular to the external magnetic field. The optical

pump and optical probe propagate along $\hat{R}$, yielding an observable

$$P_{\perp} = \frac{\langle R_{op}(t)\rangle \cos(\delta)}{\langle R_{op}(t)\rangle + \Gamma_{\perp}} \sin(\theta) cos(\omega t + \delta) \tag{2.35}$$

with spin relaxation rate $\Gamma_{\perp}$, optical pumping rate R_{op}, and average angle δ between the spin polarization and $\hat{R}$ during an optical pump pulse.

As noted in Equation 2.35, $P_{\perp} \to 0$ when $\hat{B} \cdot \hat{R} \to 1$; in other words, the magnetometer sensitivity goes to zero as the bias field approaches the optical pump/probe direction. In this work, the magnetic bias field is nominally orthogonal to the optical pump direction in order to maximize the sensitivity, hence $P_{\parallel} \to 0$ and $\hat{B} \cdot \hat{R} \to 0$. As demonstrated above in Section 2.1.1, it can be shown (A. R. Perry et al. 2020) that the steady-state phase shift of the spin precession response to the optical pump pulses is

$$\delta = \tan^{-1}(\Delta\omega T_2) = tan^{-1}\frac{\delta\omega}{\Gamma_2} \tag{2.36}$$

with frequency detuning $\Delta\omega = \omega - \omega_L$. This experiment uses an optical probe beam co-propagating with the pump to detect the atomic spin polarization. The probe is detuned far off the optical resonance, $\Delta_{opt} \gg \Gamma_{3/2}$, where $\Gamma_{3/2}$ is the observed broadened optical linewidth of the $^{87}Rb\ ^5P_{3/2}$ state (including all contributions such as collisional broadening and thermal effects). Here the Faraday rotation of the probe light due to the spin-dependent index of refraction of the atoms minimally perturbs the spins (W. Happer, Jau, and T. Walker 2010). Recall from Equation 2.24 that the probe beam acquires an optical polarization rotation

$$\phi(t) \propto NP_R(t) \tag{2.37}$$

where N is the number of atoms in the sample volume. A polarimeter converts $\phi(t)$ into an electrical signal; demodulation at the pump pulse repetition frequency ω of the electrical signal representing the probe rotation angle, for small $\Delta\omega \approx 0$, yields in-phase and quadrature signals proportional to $\Phi_{pr} N P_{\perp} \cos(\delta)$ and $\Phi_{pr} N P_{\perp} \sin(\delta)$, respectively. So far, the description above has focused on single co-propagating pump and probe lasers;

a second, orthogonal optical probe beam may yield performance advantages (Lee, V.G. Lucivero, et al. 2021) in unshielded applications where $\hat{B} \cdot \hat{R}$ is rarely negligible. Further, an orthogonal second probe beam provides the basis for real-time observation of the polarization vector in 3D space; coupled with a small-amplitude applied oscillating field to lift a sign degeneracy in the measurement, this will enable measurement of not only Ω but also $\hat{\Omega}$. This topic will be covered in more detail along with attendant theory in Chapter 5.

In addition, in practical magnetic sensing applications there are great advantages to be gained in suppression of the effects of fluctuations in relatively uniform background magnetic fields by configuring pairs or arrays of magnetometers as gradiometers or differential magnetometers (V.G. Lucivero et al. 2022; Smullin et al. 2009; Zhang et al. 2020; I. A. Sulai et al. 2019). The experiment described in this chapter includes a simple 1-dimensional array consisting of only two sensitive elements to investigate and demonstrate the differential measurement capabilities of this magnetometer.

2.3 Experimental Apparatus

The experimental apparatus used in the work described in this thesis is largely of my own design/architecture, building upon and modernizing the concepts first demonstrated by Bell and Bloom more than 60 years ago to achieve improved performance. This design and architecture sought to maximize the use of commercially available equipment, re-used the vapor cell housing from a previous experiment performed in the same lab (Zhivun et al. 2019), and relied upon our collaborators (A. R. Perry et al. 2020) for LabVIEW software for control of the optical pump pulse triggering in open-loop mode as in this chapter and Chapter 4. The LabVIEW software and FPGA firmware used in Chapter 3 was developed according to an architecture I designed, and was implemented in collaboration with our group's undergraduate lab assistant Jonas Tost (Tost, M. Bulatowicz, and T.G. Walker 2023). The overall apparatus was assembled with the aid of another undergraduate lab assistant, Alec Hryciuk.

After we conceived the basic concept, I generated the appropriate system architecture, calculated necessary component specifications, and selected appropriate commercially available equipment, including the PXIe system and modules, laser light sources, the method of and equipment for optical pump pulse generation, the lock-in amplifier, optics components, vapor cell, and feedback architecture. Where commercially available equipment was insufficient for the requirements of this experiment, I designed the necessary components: these include the pump pulse triggering logic (Appendix A.1), the pump pulse shuttering system based on a free-space electro-optic modulator, the high-performance differential photodetector preamp (Appendix A.2), the high-performance polarimeter itself, and the ceramic heaters for the vapor cell.

An abbreviated schematic of the apparatus used in this experiment at the University of Wisconsin - Madison is shown in Fig. 2.5. For each detection zone, an isotopically enriched ^{87}Rb atomic vapor and 0.8 amagat of N_2 buffer gas is housed in a 1 cm internal diameter by 1 cm internal length cylindrical vapor cell. The vapor cell is surrounded by ceramic RF heating coils that are designed to minimize induced magnetic fields (M. Bulatowicz 30 March 2012) and thermal insulators consisting of aerogel sheets to maintain a ^{87}Rb vapor pressure of approximately 2-3 $\times$ 10^{12} cm^{-3}. In accordance with (M. Bulatowicz 30 March 2012), each RF heating coil is a planar 3-layer thick-film-on-substrate ceramic circuit board with a magnetic 16-pole winding pattern around the substrate perimeter, designed for minimum self-inductance (minimum induced magnetic field and minimum reactive impedance); the vapor cell is surrounded by a pair of these heating coils, oriented opposite to each other for a net 32-pole RF magnetic coil pattern surrounding the vapor cell. Each heater on its own has been measured to produce a magnetic field of approximately $1nT/A$ on average over the volume of the vapor cell.

For further suppression of the effects of the magnetic field produced by the heaters, the heater drive signal is a sine wave detuned thousands of magnetic linewidths away from the natural Larmor precession frequency of the spins. The heater drive signal is an open-loop voltage control system supplied by a custom designed circuit that simply amplifies and AC

couples an input waveform from a function generator, using a potentiometer to control the gain, and an Apex Micro PA107DP power amplifier to drive the increased voltage and current through the heaters. The heaters dissipate approximately 0.3 W per vapor cell to heat the vapor cells to approximately +85 degrees C. In future work, the heating system may be modified to operate in closed-loop mode for tighter control of vapor cell temperature, and rather than using electrical resistive heat power one may also heat the vapor cell in an effectively non-magnetic fashion using a laser of an appropriate wavelength to be absorbed by the glass of the vapor cell itself or by an appropriate attached optical absorption element (Kitching 2018).

The vapor cell and thermal management for each measurement zone is housed in its own custom 3D printed ABS plastic shell located inside a 4-layer magnetic shield (Twinleaf MS-2). This magnetic shield includes integrated coils for controlling the vector field components and all independent first order magnetic field gradient components. All of the experiments described in this thesis use a magnetic bias field orthogonal to the optical pump at tens of micro-Tesla; orders of magnitude greater than would allow for SERF regime operation (I. M. Savukov and M. V. Romalis 2005). For a continuously synchronously pumped magnetometer, a bias field orthogonal to the optical pump axis represents a condition in which the spins are maximally susceptible to spin-exchange relaxation, residing in the fast spin-exchange limit with a low spin-exchange relaxation slowing-down factor (W. Happer and Tam 1977) while still able to take some advantage of light narrowing phenomena to suppress the spin-exchange relaxation at the cost of increased optical pump power broadening (Appelt et al. 1999, Equation 2.40). Thus, the investigated conditions represent the fastest spin polarization relaxation rate which may be observed under otherwise-optimal conditions; as shown in Equation 2.29, the photon shot noise limit is proportional to the overall spin polarization relaxation rate Γ_2. The electric current for driving magnetic bias and gradient fields is supplied using a low-noise electrical current driver (Twinleaf CSUA-1000). The electrical current-to-field and current-to-gradient conversion factors for the magnetic field coils and magnetic gradient coils, respectively, provided within the mag-

netic shield were calibrated at the location of each vapor cell by way of the relationship described in Equation 2.33.

The optical pump beam is generated using a Vescent Photonics DBR laser driven by a Vescent Photonics laser controller and is tuned near resonance with the 795nm D1 optical transition while an optical probe beam generated with a second DBR laser and driven by a Thorlabs laser controller, tuned near the 780nm D2 optical transition, monitors the atomic spin. The pump beam is intensity modulated using a scheme based on a Newport 4102 electro-optic modulator as shown in Figure 2.6. Logic signals driving "on" versus "off" states of the optical pump beam are generated by a NI PXIe-6614 precision reference counter/timing module with the optional oven-compensated crystal oscillator (OCXO) included for stability and noise performance; the OCXO also provides the timing reference for the PXIe chassis backplane timebase. For minimum periodic jitter in the optical pump pulse trigger logic signals, the apparatus uses an integer countdown from the NI PIXe-6614 reference timebase clock frequency.

When the optical pump beam is in the "off" state, I measure single-digit micro-Watt optical power outputs from the fiber. When the optical pump beam is in the "on" state, I measure a typical optical power output from the fiber of 20 mW. The probe is operated in a continuous steady state mode at approximately 7 mW optical power as measured prior to the non-polarizing beamsplitter shown in Fig. 2.5. The probe and pump are simultaneously combined and split along two separate directions using a non-polarizing beamsplitter cube; one set of combined, co-propagating beams is directed through each of two vapor cells separated by 9cm. On the far side of each vapor cell, the pump light and probe light are separated using a dichroic mirror. The probe light for each zone is sent to a respective balanced polarimeter and corresponding custom differential photocurrent detection circuit consisting of a carefully-designed transimpedance amplifier (current to voltage converter; see Appendix A.2) for each photodiode, and one or more difference amplifiers to generate a voltage signal corresponding to the differential photocurrent. The observed total photocurrent for each zone is 1.5 mA, corresponding to approximately 3

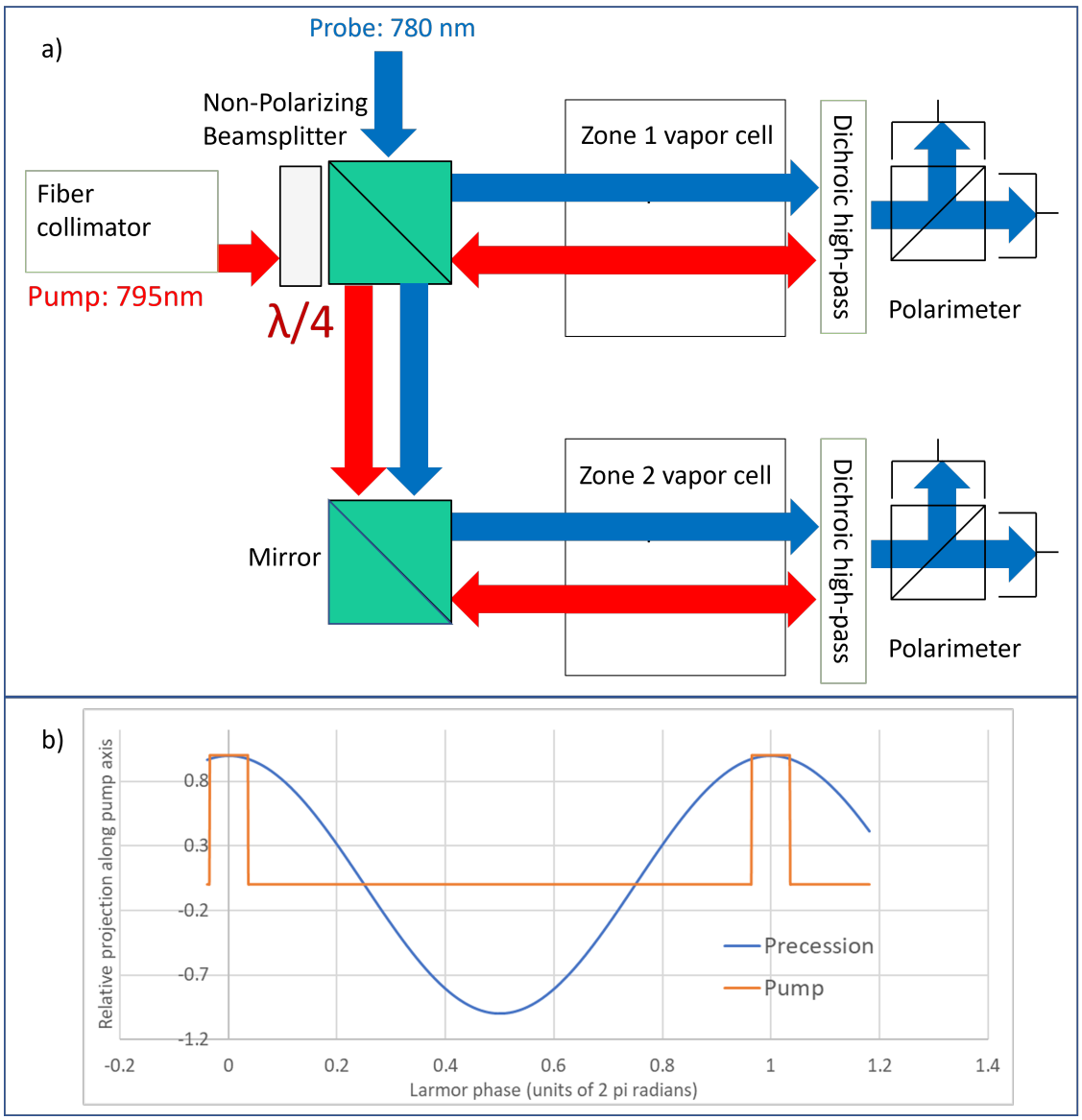

Figure 2.5: a) Block diagram of the operational concept. Collimated optical pump and probe beams are combined and split along two optical paths through respective ^{87}Rb vapor cells, each associated with a respective polarimeter. b) Notional timing diagram showing optical pump pulses during a Larmor precession cycle when the pulses are applied at the Larmor rate

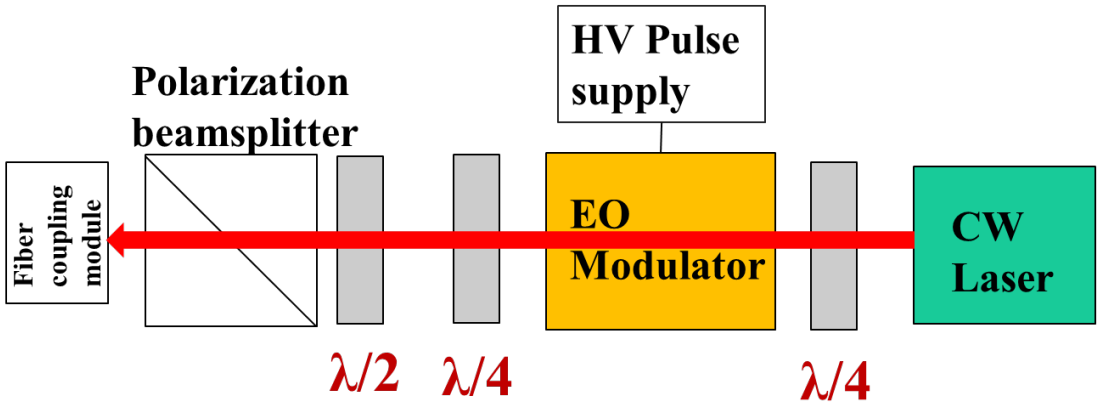

Figure 2.6: Block diagram of the optical pump intensity modulation scheme. The CW laser wavelength of the optical pump is near the ^{87}Rb D1 transition; the EO modulator, waveplates, and polarization beamsplitter work together to generate amplitude modulation of the optical pump beam in the form of short-duty-cycle optical pulses observed at the output of the polarization beamsplitter, which are then coupled into an optical fiber which transmits the optical pump pulses to a collimator (Figure 2.5)

mW reaching each polarimeter.

The voltage signal corresponding to the differential photocurrent signal is demodulated using a lock-in amplifier (SR865A) referenced to the pump pulse repetition rate; the output of the lock-in amplifier is proportional to the product of input signal amplitude and $sin(\delta)$ (Equation 2.36). In the limit of small δ and stable polarization signal amplitude, the lock-in amplifier output is simply proportional to the difference between the pump pulse repetition rate and the natural Larmor precession frequency of the spins.

For the case of scalar magnetic field measurement, the polarimeter signal from a single detection zone is sent to the lock-in amplifier input as a differential signal: for single-channel scalar measurement with polarimeter photodetectors α and β (associated with the S and P polarization components of the detected probe beam, respectively) the custom photodetector circuit is configured to generate a complementary pair of signals consisting of $\alpha-\beta$ and $\beta-\alpha$, enabling the use of a differential input configuration at the lock-in amplifier, labeled "A-B" on the SR865A. This configuration is observed to significantly reduce the influence of electrical noise associated with the finite electrical ground impedance between the lock-in amplifier and the photodetector circuit; the grounding noise is substantially

common mode between the two lock-in inputs. In the case of gradient measurement, the photocurrent signals from the pair of zones are directly differenced at the input of the lock-in amplifier, with a photodetector circuit configuration of simply $\alpha - \beta$ for each zone. In each case, the time series of the output of the lock-in amplifier is recorded using a low-noise data acquisition system (NI PXIe-5171R; 250 million samples per second at 14 bits resolution per sample) and the resulting time series is converted to a frequency spectrum using a fast Fourier transform (FFT) algorithm. The rationale for choosing the PXIe-NI 5171R are described in Appendix A.4. The frequency spectrum is appropriately scaled based on the known applied input stimulus signal, calibrated using the relationship described in Equation 2.33 (field or gradient, as appropriate).

The output response of the demodulation, as perceived by the data collection system, is the result of multiple factors working together, including intensity, wavelength, and rotation angle of the probe, gain of the photodetection circuit, proximity of the pump pulse repetition rate to the natural Larmor frequency of the spins, the angle of the bias field relative to the pump direction, phase tuning of the demodulation signal, and the applied signal gains. To account for the combined effect and appropriately scale the noise spectra, each measurement is calibrated using an input stimulus magnetic field modulation or gradient modulation, as appropriate, at a known frequency and known (calibrated) amplitude. For the measurements shown in Figures 2.9 and 2.10, the apparatus was run in open-loop mode with a continuous series of pump pulses applied at a well-defined repetition rate corresponding to the Larmor precession frequency in the magnetic bias field B_0, and with the bias field orthogonal to the pump/probe direction. Under these conditions, the output of the demodulation represents deviations in the phase of the polarimeter signal (ideally, identical to the phase of the precessing spin ensemble) relative to the optical pump pulse triggering signal, and is interpreted as deviations in the magnetic field relative to B_0.

Differential magnetic scalar measurements were performed by electronically subtracting the polarimeter signals of the two individual scalar magnetometer channels at the

input of the SR865A lock-in amplifier and demodulating the result. Similar to how the single-channel magnetic spectra were calibrated, an oscillating magnetic gradient signal of a known amplitude and frequency was applied during the measurement to yield proper scaling of the noise spectra; the magnetic gradient stimulus signal was calibrated using the relationship described in Equation 2.33.

2.4 Noise Optimization and Tuning

2.4.1 Noise Optimization

As described in section 2.1.1, optically pumped atomic magnetometers exhibit three major fundamental noise sources (Budker and Kimball 2013): photon shot noise δB_{PSN}, quantum projection noise δB_{QPN}, and probe AC Stark shift noise, also known as light shift noise δB_{LSN}. An additional potentially significant source of noise is the net sum of additional noise from the electronics used for detection and interpretation of the experimental signals, expressed here as δB_{tech}. Photon shot noise per square root Hz as observed at the output of the polarimeter is a function of the fundamental electron charge q, total photocurrent I_{PD} (the product of probe photon flux Φ_{pr} and photodetector quantum efficiency η). Translating this shot noise into magnetic units requires scaling based on the gain of the magnetometer. In a 1 Hz bandwidth and ignoring the effects of any additional filters in the signal processing electronics, such as those in the lock-in amplifier:

$$\delta B_{PSN}(f_{det}) = \frac{\sqrt{2\Phi_{pr}\eta}}{gain(f_{det})} = \frac{\sqrt{2qI_{PD}(1+f_{det}^2\pi^2T_2^2)}}{gain(0)} \tag{2.38}$$

$$= \frac{\Gamma_2\Gamma_{\nu,pr}^2(1+4\frac{\Delta^2}{\Gamma_{\nu,pr}^2})\sqrt{1+f_{det}^2\pi^2T_2^2}}{lr_ecfn\Delta P\gamma\sqrt{2\eta\Phi_{pr}}} \tag{2.39}$$

where Equation 2.39 is based on Equation 8 from I.M. Savukov et al. 2005 and has added a frequency dependence based on the open-loop alkali -3dB response bandwidth (in Hz: πT_2). This expression can be separated out into a set of constants (π, the speed of light c, the probe path length through the vapor cell l, the classical electron radius r_e, the probe

transition oscillator strength f, and the gyromagnetic ratio γ); the frequency dependence of noise, as observed at the frequency f_{det} at which one wishes to detect magnetic fluctuations (with a corresponding spin phase response bandwidth Γ_2); a set of probe and photodetector characteristics (probe detuning Δ from the optical transition, linewidth $\Gamma_{\nu,pr}$ of the probe optical transition, probe photon flux Φ_{pr}, and the photodetector quantum efficiency η); and a set of parameters relating to the alkali (relaxation rate $\Gamma_2 = T_2^{-1}$, number density n, and polarization P). For the vapor cell used in this experiment, the optical broadening is dominated by collisions with the buffer gas (M. V. Romalis, Miron, and Cates 1997): $\Gamma_{\nu,pr} = 18.1GHz/Amg * 0.8Amg = 14.5GHz$. Optimization of Equation 2.39 requires simultaneous optimization of the alkali parameters and optical probe parameters.

Of note is that Equation 2.39 contains the implicit assumption that Φ_{pr} and P are uniform throughout the sensitive volume; meanwhile, this experiment utilizes a vapor cell in which approximately the entire internal volume is optically pumped and optically probed, with the $1/e^2$ intensity radius of the pump located at the approximate cylindrical borders of the vapor cell interior and the $1/e^2$ intensity region on the major axis of the spatially elliptical probe beam also approximately located at the cylindrical borders of the vapor cell interior. Thus, in this experiment the results of Equation 2.39 and the associated sensitivity optimization described below must be averaged over the internal volume of the vapor cell in order to generate a valid prediction of photon shot noise; the topic of volumetric total figure of merit for sensitivity will be covered in more depth in Section 2.4.3.

In the following analysis, I have arbitrarily chosen to focus first on optical probe optimization as a function of other parameters and then focus on co-optimization of probe and alkali response. One component of optimization of Equation 2.39 is the transverse relaxation rate Γ_2, itself a function of the optical pumping rate, polarization, probe scattering

rate $\frac{\Gamma_{pr}}{q_{op}}$, and spin destruction rate Γ':

$$\Gamma_2 = \frac{\langle R_{op} \rangle}{q_{op}} + \frac{nk_{SE}(1-P)}{q_{SE}} + \frac{\Gamma_{pr}}{q_{op}} + \frac{\Gamma'}{q_{op}} = \frac{\langle R_{op} \rangle}{q_{op}} + \Gamma_\perp \tag{2.40}$$

In this experiment, the laser linewidth is much narrower than the broadened optical transition, so the probe scattering rate is given by:

$$\frac{\Gamma_{pr}}{q_{op}} = \frac{\Phi_{pr}\sigma_{pr}}{Aq_{op}} = \frac{\Phi_{pr}}{Aq_{op}} \frac{2r_e cf}{\Gamma_{\nu,pr}(1 + 4\frac{\Delta^2}{\Gamma^2_{\nu,pr}})} \tag{2.41}$$

where $\sigma_{pr} = \frac{\sigma_0}{1+4\frac{\Delta^2}{\Gamma^2_{\nu,pr}}}$ is the photon absorption cross section for the optical probe and A is the cross sectional area of the optical probe beam. Restating $\Gamma_\perp$ based on Equation 2.41,

$$\Gamma_\perp = \frac{nk_{SE}(1-P)}{q_{SE}} + \frac{\Phi_{pr}\sigma_0}{Aq_{op}(1+4M^2)} + \frac{\Gamma'}{q_{op}} \tag{2.42}$$

and acknowledging the relationship between $P_\perp$ ($= P$ in this experiment) and $\langle R_{op} \rangle$ (Equation 2.35), Equation 2.39 optimizes when $\Gamma_{pr} \approx (1-P)\langle R_{op} \rangle$, indicating that the optimum condition arises when the pump and probe photon scattering rates are comparable. With the probe beam optimized in terms of the time-average optical pumping rate, the quantity to optimize in the case of this experiment in which the spin precession is orthogonal to the bias field ($P = P_\perp$) is

$$\frac{\Gamma_2}{nP} \approx \frac{\langle R_{op} \rangle (2-P)}{nPq_{op}} + \frac{k_{SE}(1-P)}{Pq_{SE}} + \frac{\Gamma'}{nPq_{op}} \tag{2.43}$$

where $\langle R_{op} \rangle$ is the time-average optical pumping rate, q_{op} is the optical pumping rate slowing-down factor (I.M. Savukov et al. 2005) associated with Γ_2, k_{SE} is the spin-exchange constant depending on the spin-exchange cross-section σ_{SE} and average velocity $\bar{v}$, q_{SE} is the ^{87}Rb spin-exchange relaxation slowing-down factor, Γ_{pr} is the probe photon scattering rate, and Γ' represents the sum total of additional relaxation rates including interaction with the cell walls and spin-destruction collisions with other alkali atoms and with the buffer gas.

Equation 2.43 includes both the alkali polarization and optical pumping rate as explicit terms; these are, however, deterministically related as shown in Equation 2.35, somewhat obscuring optimization of Equation 2.43. Choosing arbitrarily to optimize based on alkali polarization (although one could equivalently express Equation 2.43 in terms of $\langle R_{op} \rangle$ to optimize directly for optical pumping rate), one may solve Equation 2.35 for $\langle R_{op} \rangle$ and insert the result in Equation 2.43:

$$\frac{\Gamma_2}{nP} = \frac{\Gamma_\perp P(2-P)}{(1-P)nq_{op}} + \frac{k_{SE}(1-P)}{Pq_{SE}} + \frac{\Gamma'}{nPq_{op}} \tag{2.44}$$

where $\langle R_{op} \rangle$ has been expressed in terms of $\Gamma_\perp$ such that it is straightforward to solve for the optimal polarization. For an alkali atom such as ^{87}Rb with a spin-3/2 nucleus, $q_{op} = 4$ (I.M. Savukov et al. 2005). For the measured values of $\frac{\Gamma'}{q_{op}} = 32s^{-1}$ and $\Gamma_\perp \approx 1000s^{-1}$ in the low polarization limit at a number density of $n = 2 * 10^{12} cm^{-3}$, Equation 2.44 optimizes when $P \approx 0.87$, implying $\frac{\Gamma_{pr}}{q_{op}} \approx 40s^{-1}$. Inserting these conditions into Equation 2.44 gives:

$$\frac{\Gamma_2}{nP} \approx k_{SE} \frac{1.13 + .15q_{op}}{q_{SE}q_{op}} \tag{2.45}$$

which is effectively independent of number density. Equation 2.44 therefore suggests a straightforward optimization procedure, which will be discussed further in Section 2.4.2. I have measured the value of q_{SE} in this experiment by way of measuring the transverse relaxation rate $\Gamma_\perp$ in the low-polarization limit as a function of vapor cell temperature as a proxy for alkali number density. For this measurement, I calibrated the vapor cell temperature at temperatures below 90 degrees C based on the measured number density using Equation 2.32 and the relationship between temperature and alkali number density (Steck 2003). In contrast to the reported value of $q_{SE} = 5$ for a magnetometer operating at $\omega_L = 2\pi * 99kHz$ (I.M. Savukov et al. 2005)–valid for SERF magnetometers using $I = 3/2$ nuclei, which necessarily operate in the fast spin exchange limit (W. Happer and Tam 1977)–I find that q_{SE} in this experiment is nearly a factor of 5 smaller at approximately

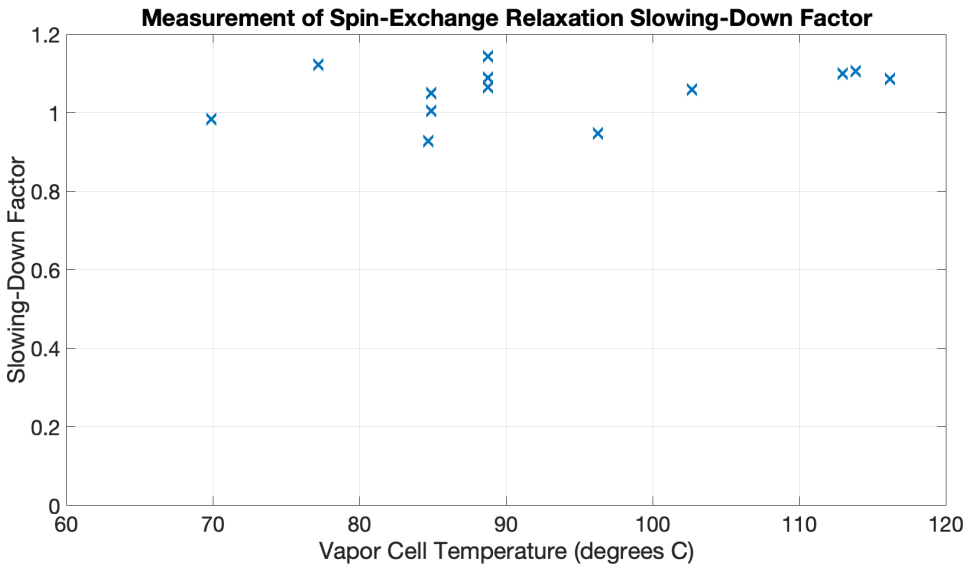

Figure 2.7: Plot of measured q_{SE} as a function of vapor cell temperature. The data shows an average of approximately 1.1 for the value of q_{SE}

1.1, in good agreement with the value $q_{SE} = \frac{9}{8}$ for ^{87}Rb ($I = 3/2$) in the slow spin-exchange limit ($\omega_L \gg R_{SE}$) as calculated by W. Happer and Tam 1977. Figure 2.7 shows the results of measurement of q_{SE} as a function of vapor cell temperature.

This further reduces Equation 10 to

$$\frac{\Gamma_2}{nP} \approx 0.4 k_{SE} \tag{2.46}$$

for this experiment in an optimized condition with the bias field orthogonal to the optical pump direction. Expanding and rearranging Equation 2.46 we find

$$n \approx \frac{\langle R_{op} \rangle}{k_{SE}} \tag{2.47}$$

under the conditions in which Equation 2.39 has been optimized. As noted above in Equation 2.39, Γ_2 determines the phase response bandwidth of the spins; Equation 2.47 clearly demonstrates that under optimized conditions the availability of pump photons, driving $\langle R_{op} \rangle$, determines the achievable "corner frequency" for the photon shot noise: of particular note, the high-frequency limit of photon shot noise in the optimized regime is

inversely proportional to the available optical pumping rate.

Quantum projection noise is similarly dependent on the relaxation rate and number density, along with the volume V of spins interacting with the probe beam, and the gyromagnetic ratio (Alem, Sauer, and M.V. Romalis 2013; Ledbetter et al. 2008):

$$\delta B_{QPN} = \frac{1}{\gamma}\sqrt{\frac{\Gamma_2}{nV}} \tag{2.48}$$

Additional noise is contributed by quantum fluctuations in the polarization state of the optical probe beam (Ledbetter et al. 2008). This noise occurs along the probe direction ($\hat{x}$) and generates an effective magnetic field noise based on the scalar magnetic field deviation generated by the resulting AC Stark shift noise. The AC Stark energy shift modifies the energy splitting of the Δm sublevels and is therefore indistinguishable from a magnetic field and will exhibit its own shot noise based on the photon shot noise of the σ^+ and σ^- components of the optical probe beam linear polarization state. However, the magnetic bias field for the present experimental results shown herein is applied orthogonal to the pump/probe direction (applied in the $\hat{y} - \hat{z}$ plane). Hence, $\hat{x} \cdot \vec{B} \rightarrow 0$ in this experiment. Therefore, the AC Stark shift noise does not contribute meaningfully to the total observed noise under the conditions tested.

Using the polarimeter circuit described in Appendix A.2, the technical noise in this experiment is dominated by the transimpedance amplifier gain resistor thermal Johnson-Nyquist electrical current noise, which is itself approximately an order of magnitude below the photon shot noise limit. For the circuit configuration used in this experiment, the total electrical noise normalized to the differential signal is approximately 17 $nV/\sqrt{Hz}$ ("Texas Instruments Application Report SLVA043B: Noise Analysis in Operational Amplifier Circuits" n.d.), while the photon shot noise accounts for approximately 150 $nV/\sqrt{Hz}$, again normalized to the differential polarimeter preamp output configuration. Therefore, $\delta B_{tech} = 0.4fT/\sqrt{Hz}$.

In this experiment, the measured value of $\frac{\Gamma_{PR}+\Gamma'}{q_{op}}$ is approximately 60/s when the experiment is tuned according to Section 2.4.2; thus, approximately minimum photon shot

Noise Source	Noise ($fT/\sqrt{Hz}$)
Photon shot noise	3.7
Quantum projection noise	0.6
Light shift noise	0.0
Technical Noise	0.4
Total	3.7

Table 2.1: Table of fundamental noise sources for this synchronously pumped magnetometer under experimentally optimized conditions.

noise and approximately minimum quantum projection noise are achieved at $\frac{nk_{SE}}{q_{SE}} > 600/s$ under experimentally optimized conditions; this is achieved with a number density in the low 10^{12} per cubic centimeter range, corresponding to a vapor cell temperature of approximately +85 degrees C, dramatically lower than for a SERF magnetometer demonstrating comparable measured total sensitivity (Wyllie et al. 2012) but with significantly higher fundamental limits based on the increase in Γ_2 associated with spin-exchange relaxation.

Under typical operating conditions for the measurements shown in this paper, the measured number density is $2*10^{12}$ per cubic centimeter, $\Gamma_\perp$ is approximately 1000/s in the low-polarization limit, and the effective sensitive volume observed by the probe is approximately 0.6 cm^3. The measured gain in the low-frequency limit of magnetic field modulation, for small deviations of the bias field about $\Delta\omega = 0$ is typically 6000 to 7000 amps per Tesla, and the total photocurrent is approximately 1.5 mA. Using Equations 2.38 and 2.48, the calculated photon shot noise limit is slightly under 4 $fT/\sqrt{Hz}$, while the quantum projection noise limit is approximately 0.6 $fT/\sqrt{Hz}$. Thus, the quantum projection noise does not contribute meaningfully to the total noise power in this experimental configuration.

Equations 2.39, 2.47, and 2.48 demonstrate a straightforward means of further improvement (where improvement is defined as decreased noise, increased bandwidth, etc. as required by a given application) in the standard quantum limit for this magnetometer through the use of a physically larger vapor cell, an increase in optical probe path length, and an increase in the available optical pump photon flux (i.e. optical pumping rate).

The performance of this magnetometer can therefore be scaled for desired performance characteristics of a given application and for limitations of the available optical pump and probe system.

Rather than solely focusing on noise optimization for this experiment, consider a more-generic scenario in which $\hat{R}\cdot\hat{\Omega} = cos(\theta)$ is not negligible, and therefore the AC Stark shift noise (Equation 2.31) must be taken into account in a more generic optimization of the magnetometer response physics. The total fundamental noise amplitude is based on the sum of the noise power of the individual contributors. Combining Equations 2.31, 2.48, and 2.29 in the limit that the optical probe is detuned by multiple linewidths from the D2 optical transition and in the limit of low detection frequency,

$$\begin{aligned}\delta B^2_{fundamental} &= \delta B^2_{QPN} + \delta B^2_{LSN} + \delta B^2_{PSN} \\ &= \frac{\frac{\langle R_{op}\rangle}{q_{op}} + \frac{nk_{SE}(1-P)}{q_{SE}} + \frac{\Gamma_{pr}}{q_{op}} + \Gamma_{SD}}{\gamma^2 nV} + \frac{\Gamma_{pr} r_e c f cos(\theta)}{32\gamma^2 A^2 \Gamma_{\nu,pr}} + \frac{\left(\frac{\langle R_{op}\rangle}{q_{op}} + \frac{nk_{SE}(1-P)}{q_{SE}} + \frac{\Gamma_{pr}}{q_{op}} + \Gamma_{SD}\right)^2 \Gamma_{\nu,pr}}{2\eta r_e c f \Gamma_{pr} n^2 l^2 P_\perp^2 \gamma^2}\end{aligned} \tag{2.49}$$

Differentiating with respect to Γ_{pr},

$$\begin{aligned}d_{\Gamma_{pr}}\delta B^2_{fundamental} = \frac{1}{\gamma^2 nV q_{op}} + \frac{r_e c f \hat{R}\cdot\hat{\Omega}}{32\gamma^2 A^2 \Gamma_{\nu,pr}} + \frac{\left(\frac{\langle R_{op}\rangle}{q_{op}} + \frac{nk_{SE}(1-P)}{q_{SE}} + \frac{2\Gamma_{pr}}{q_{op}} + \Gamma_{SD}\right)\Gamma_{\nu,pr}}{\eta \Gamma_{pr} r_e c f n^2 l^2 P_\perp^2 \gamma^2 q_{op}} \\ - \frac{\left(\frac{\langle R_{op}\rangle}{q_{op}} + \frac{nk_{SE}(1-P)}{q_{SE}} + \frac{\Gamma_{pr}}{q_{op}} + \Gamma_{SD}\right)^2 \Gamma_{\nu,pr}}{2\eta \Gamma_{pr}^2 r_e c f n^2 l^2 P^2 \gamma^2}\end{aligned} \tag{2.50}$$

one finds that the optimum probe scattering rate becomes a function of the angle between the optical axis and the magnetic field; however, until θ becomes small, the optimal probe relaxation rate is still in the vicinity of $\langle R_{op}\rangle(1-P)$, though slightly smaller than predicted above. Once again setting $\Gamma_{pr} = \langle R_{op}\rangle(1-P)$ and choosing to optimize for polarization:

$$\begin{aligned}\delta B^2_{fundamental} = \frac{\frac{\langle R_{op}\rangle(2-P)}{q_{op}} + \frac{nk_{SE}(1-P)}{q_{SE}} + \Gamma_{SD}}{\gamma^2 nV} + \frac{\langle R_{op}\rangle r_e c f cos(\theta)}{32\gamma^2 A^2 \Gamma_{\nu,pr}} \\ + \frac{\left(\frac{\langle R_{op}\rangle(2-P)}{q_{op}} + \frac{nk_{SE}(1-P)}{q_{SE}} + \Gamma_{SD}\right)^2 \Gamma_{\nu,pr}}{2\eta r_e c f \Gamma_{pr} n^2 l^2 P_\perp^2 \gamma^2}\end{aligned} \tag{2.51}$$

it becomes clear that the optimal polarization differs only based on the effects of the slightly smaller optimal probe scattering rate. Thus, the procedural tuning suggested by

Equations 2.44 and 2.45 remains approximately valid for real-world values of the angle between the optical axis and the incident magnetic field.

2.4.2 Tuning

As shown in the noise optimization analysis, Equations 2.44 and 2.45, one may conclude that there exists a straightforward empirical procedure for experimental optimization of the operation of the magnetometer. The procedure I have developed is as follows. First, I measure Γ': in the weak probe limit, I apply a bias field along the optical pump direction, apply a long-duration pulse of optical pump light (time duration $\gg 1/\Gamma'$), and measure the relaxation time constant in the low-polarization limit. I then set $\Gamma_{pr} \approx \Gamma'$ by tuning the wavelength and intensity of the optical probe beam such that I have approximately doubled the longitudinal relaxation rate. Once this is complete, I re-orient the bias field orthogonal to the optical pump beam, send in a series of short-duty-cycle optical pump pulses at approximately $\omega = \omega_L$ and measure $\Gamma_\perp$ in the low-polarization limit. Next, I adjust the alkali number density using vapor cell temperature until $\Gamma_\perp > 11(\Gamma_{pr} + \Gamma')$, again with $\Gamma_\perp$ as measured in the low-polarization limit. Finally, I send in a continuous series of short-duty-cycle optical pump pulses at $\omega = \omega_L$ with maximum optical pump "on" state intensity; I adjust the optical pump duty cycle and both pump and probe wavelength while observing the magnetometer response to a magnetic stimulus field of known frequency applied along the bias field, as measured at the output of the lock-in amplifier, until the response is maximized. I then verify that the optical pump beam is optimized by adjusting the duty cycle and observing the response characteristics; verifying that I do indeed have the ability to over-pump the spins at the chosen alkali number density.

Given an optimal spin polarization, deviation from this optimal value will degrade the magnetometer performance. Spin polarization will vary as a function of position within the vapor cell due to interaction with the vapor cell walls and with the buffer gas, along with the nonuniform optical intensity throughout the volume of the cell. This spatial variation of conditions throughout the vapor cell complicates analysis of overall optimization of

the magnetometer: experimental parameters such as pump and probe beam collimation size and intensity profile will affect the volumetric average optimization as observed by the optical probe beam. The degree of global optimization, then, as opposed to solely empirical optimization for a specific set of experimental parameters can be analyzed in more detail using finite element analysis.

2.4.3 Finite Element Modeling

I constructed a finite element model in COMSOL Multiphysics Version 3.5a with the goal of examining and visualizing in more detail the effects of experimental parameters on magnetometer operation and to predict optimal conditions and the consequences of varying experimental parameters. This model is used to calculate a figure of merit (FOM) for magnetometer sensitivity. In contrast to how one might interpret Equation 2.39, the ^{87}Rb polarization in the vapor cell is not simply a single uniform polarization throughout the sensitive volume but rather exhibits a spatial distribution with zero polarization at the vapor cell walls and effects from the spatially nonuniform $\langle R_{op} \rangle$, further modified by the optical pump scattering rate proportional to $1 - P$. This model calculates the spatial distribution of ^{87}Rb polarization based on Fick's law of diffusion and Equations 2.35, 2.52, and 2.56. The diffusion coefficient for ^{87}Rb in N_2 buffer gas is 0.16 at 273 K and 1 amagat (Franz and Volk 1976); the model utilizes this value and the buffer gas number density of 0.8 amagat as mentioned above along with a vapor cell temperature of 358 K to calculate diffusion of the spins in the vapor cell. For the sake of simplicity, instead of directly using Equations 2.35 and 2.56 as shown, the model instead uses a normalized effective optical pumping rate $R_{eff} = R_{OP}(r, x)/\Gamma_{\perp}(P \to 0)$ based on the experimentally measured $\Gamma_{\perp}$ in the low-polarization limit; this normalized optical pumping rate is a controllable parameter in the model.

The model requires appropriately-defined input conditions; a priori analysis of the incident optical intensity and the characteristics of its variation through the volume of the vapor cell serve as inputs to the model. The optical pump intensity in this experiment

exhibits an approximately Gaussian distribution at the incident face of the vapor cell, and falls off as the pump beam propagates through the cell based on the pump optical scattering rate (a function of optical pumping rate and the local polarization). With the pump oriented along $\hat{x}$,

$$\nabla_x R_{op} = -nR_{op}dA(1-P) \tag{2.52}$$

Noting that the normalized optical pumping rate described above is the average over the entire incident cross section and further noting that the optical pump beam has an approximately Gaussian intensity profile with a $1/e^2$ radius at the radius R of the interior of the vapor cell, the optical pump beam varies as a function of distance from the cylindrical axis as

$$R_{op}(r) = R_{op,0}e^{-2r^2/R^2} \tag{2.53}$$

with the restriction that the average optical pumping rate in this calculation must be normalized to the effective optical pumping rate:

$$R_{eff} = R_{eff,0}\int \frac{2r}{R^2}R_{op}(r)dr \tag{2.54}$$

which then indicates:

$$R_{eff,0} = R_{eff}\frac{2e^2}{(e^2-1)} \tag{2.55}$$

giving a normalized optical pumping rate at the incident face of the cell of:

$$R_{eff}(r) = R_{eff}\frac{2e^{2-2r^2/R^2}}{(e^2-1)} \tag{2.56}$$

Similarly, the optical probe beam also exhibits an approximately Gaussian intensity profile, but rather than exhibiting circular symmetry instead exhibits a different $1/e^2$ distance from the center of the beam in $\hat{z}$ than in $\hat{y}$ (recall: pump and probe are both propagating along $\hat{x}$).

The finite element analysis results for the distribution of $P_\perp$ throughout the vapor cell volume under the conditions used for this experiment with the bias field orthogonal to the

optical pump beam (Figure 2.8) indicate that for an optical pump beam having a circularly symmetric Gaussian intensity distribution with $1/e^2$ intensity situated at the vapor cell cylindrical walls and at the investigated ^{87}Rb number density of $2 * 10^{12}/cm^3$, the pump beam must be tuned off resonance relative to the optical transition to obtain an optimal magnetometer response. The primary effect of this detuning in terms of magnetometer response optimization is to reduce $\nabla_x R_{op}$, thereby reducing $\nabla_x P_\perp$ and improving relative uniformity and optimization of $P_\perp$ throughout the vapor cell volume. For each iteration of the finite element model, the adjustable parameters were the optical pump detuning and the optical pump power by way of modification of the normalized optical pumping rate. The relevant figure of merit (higher is better, in this case) is the volumetric integral of the product of probe beam photon flux Φ_{probe} and the magnetometer optimization parameter nP/Γ_2 (Equation 2.43):

$$FOM = \int_V \Phi_{probe} \frac{nP}{\Gamma_2} \tag{2.57}$$

which is calculated for every iteration of the finite element model to inform further refinement of the parameters in subsequent model iterations.

The probe is assumed in the model to be consistent with the weak probe limit; far-detuned from resonance and at relatively low optical intensity such that the probe generates only negligible perturbation of the spin polarization. The finite element model figure of merit predicts optimal operation with the optical pump beam detuned approximately 5 GHz off resonance based on a simplified optical pumping model using Equation 2.56 but with only one detuning rather than individual detuning from each of the two ground states; no attempt was made in the model to examine the state distribution in the two ground states. The figure of merit calculation further predicts optimal operation of the magnetometer with a normalized optical pumping rate of approximately q_{op}. These results are both in reasonable agreement with experimental results; experimental optimization demonstrated optimal operation with the optical pump blue detuned by 3.5 GHz as measured relative to the peak of the observed broadened optical pump absorption profile, and a normalized optical pumping rate of 3.7.

This model allows for further a priori optimization for future work. For example, for the presently available optical pump power further optimization may be achievable using the buffer gas pressure as a controllable parameter; lower buffer gas pressure, for example, may increase the efficiency of photon utilization at the cost of increasing Γ' (Section 2.4.1). This may allow increases in the collimation size of the optical pump beam, reducing the spatial variation of the pump and probe beam intensity profiles incident upon the vapor cell, which may in turn reduce the polarization gradients in the volume observed by the probe beam, further improving the photon shot noise limit.

2.4.4 Differential Scalar Measurement

For optimal detection of a magnetic field differential between the two sensitive zones shown in Figure 2.5 a maximal common-mode rejection ratio (CMRR: the ratio of single-channel response to a uniform field modulation to the two-channel difference response to the same uniform modulation) is desirable (I. A. Sulai et al. 2019). In an open-loop measurement as in the present work, a high CMRR requires approximately identical magnitude and phase response (gain) outputs from the differential photodetector circuits associated with the two zones in response to a uniform magnetic field modulation, as measured at the input of the lock-in amplifier. For each of the two zones with nominally identical pump and probe characteristics, the gain observed in the photocurrent for a well-matched pair of photodetectors and a well-balanced polarimeter is shown in Equations 2.38 and 2.39 as modified by Equation 2.36. It is therefore not sufficient to equally split the optical pump and probe beams and heat the individual vapor cells to a nominally identical alkali vapor density; high common mode rejection can still only be observed in the small-differential-field limit and remains sensitive to small changes in operating parameters of the vapor cells such as alkali number density.

In the present work, a best CMRR of approximately 400 was achieved at 1 Hz as averaged over a 30 second measurement interval (i.e. a best observed CMRR of 400 at 1 Hz), indicating a response mismatch of roughly 0.25% for the two detection zones on average

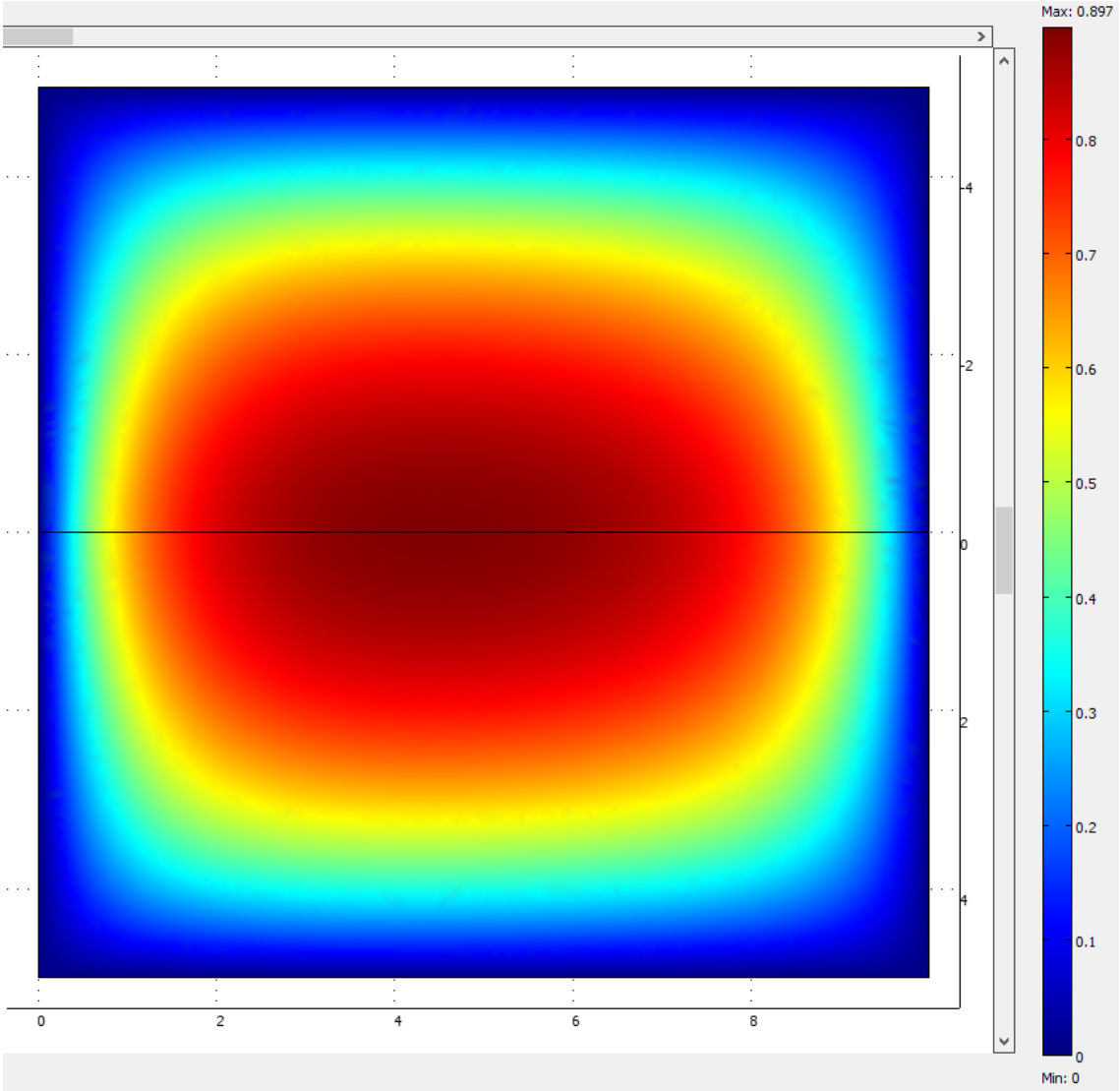

Figure 2.8: Finite element model results for alkali polarization under conditions mimicking the experiment described in this thesis (color online). The plot indicates the finite element model prediction for fractional polarization of the alkali in a slice plot passing through the center of the vapor cell with the pump along $\hat{x}$ under the predicted optimal conditions. The plot may therefore be taken as circularly symmetric about the $\hat{x}$ centerline (black horizontal line running through the center of the plot). Note that the alkali polarization is greater than the optimal value predicted by Equation 2.44 in some portions of the cell and below this value in other portions of the cell; the peak predicted polarization is 0.9 in this simulation. Also worth noting is that the region of predicted maximum polarization is located slightly to the pump incident side of the center of the cell, as expected.

over this measurement interval. At 20 Hz, the best observed CMRR increased to 3000, as averaged over a 30 second measurement interval. This was accomplished by tuning the responses of each of the two sensitive zones as observed at the output of the lock-in amplifier (SR865A) to maximally match the magnitude and phase responses to an incident magnetic field, then sending the signal from the first zone to input A of the lock-in and the signal from the second zone to input B, and using an input configuration for the lock-in of "A-B." The differential magnetic field measurement, therefore, is based on simple electrical subtraction of the voltage signals resulting from the modulating photocurrent on the two sensitive zones. Tuning parameters included the temperature of each vapor cell, optical pump and probe alignment (relative to the laboratory frame and relative to each other) in each sensitive zone, optical pump and probe position within the individual vapor cells, optical collimation of the pump and probe beams, optimization of the physical position and orientation of the individual vapor cells within the magnetic shield set, the rotational orientation of each polarimeter about the pump/probe propagation axis, and the rotational and translational orientation of the non-polarizing beamsplitter cube used for combining/splitting the pump and probe light (Figure 2.5). In future work, further improvement in the open-loop CMRR may be observed by way of post-processing calibrated individual response data in software.

In principle, a robust differential measurement with a consistently higher CMRR than reported above may be observed using individual closed-loop observations of the scalar magnetic field at each of the two zones. The reason for this is that each closed-loop magnetometer acts as a magnetic field to frequency transducer: the loop adjusts the optical pump pulse repetition rate to drive $\Delta\omega \rightarrow 0$ using ϕ as the error signal input to the loop (Equation 2.36). Under ideal conditions (no heading error, perfectly parallel magnetometer axes, identically and optimally tuned feedback for minimum error (Tost, M. Bulatowicz, and T.G. Walker 2023), identical vapor cells, and so on) the upper bound for the achievable CMRR will be limited by the combined effect of open-loop matching and feedback loop effects. For a magnetometer gain (including polarimeter response) $G(\Delta\omega(t))$

and feedback loop gain $K(\Delta\omega(t))$ the residual closed-loop error is inversely proportional to $(1 + GK(\Delta\omega(t)))$; this residual error is effectively a residual open-loop response. For an open-loop CMRR of $\xi_{openloop}$, then, the upper bound of the expected closed-loop value of CMRR would be approximately:

$$\xi_{closedloop} = \xi_{openloop}[1 + GK(\Delta\omega(t))] \tag{2.58}$$

while in any real experimental system the observed value will lie below the upper bound indicated by Equation 2.58 based on the non-ideal nature of physically and electronically separated instruments as noted above.

The present work has demonstrated a closed-loop response with $> 10^4$ suppression of residual error at 1 Hz (Tost, M. Bulatowicz, and T.G. Walker 2023). Based on the measured open-loop CMRR of 400, Equation 2.58 indicates an upper bound to the closed-loop CMRR of approximately $4 * 10^6$ at 1 Hz; the expected observed value will be somewhere below this. The present implementation of the magnetometer prevents a direct measurement of the CMRR in closed-loop operation because there is only a single optical pump pulse repetition rate for the experiment. In future work, the experiment may be updated for closed-loop operation on both sensitive zones by, for example, implementing a second EOM-based optical pump shuttering system (Figure 2.6 for entirely independent control of the second vapor cell or perhaps by adding a gradient magnetic field coil and driving this coil to eliminate the phase difference observed between the two sensitive zones (Equation 2.36).

2.5 Results and Discussion

As shown in Figure 2.9, under optimized conditions achieved as described herein, the instrument has demonstrated a measured single-channel white noise floor of approximately 10 $\frac{fT}{\sqrt{Hz}}$ at a bias field of approximately 29 μT ($\omega_L = 2\pi * 200kHz$), consistent with the noise power spectral density from the Twinleaf CSUA-1000 current source that is used to

generate the magnetic bias field. The photon shot noise limit shown in Figure 2.9 was calculated using the total polarimeter photodetector current (the sum of the photocurrents of the two photodetectors rather than the difference) along with the experimentally measured magnetometer gain as a function of frequency as shown in equation 2.38, and is consistent with the measured noise background in the absence of pump light. The demonstrated performance at 1 Hz is comparable to the lowest-noise commercially available Earth-field-scale magnetometers (*GEM Systems GSMP-35 Potassium Magnetometer* 2023), which exhibit a noise specification in the range of 200 fT/$\sqrt{Hz}$ at 1 Hz.

Finite frequency spikes observed in the spectra shown in Figure 2.9 include 60 Hz and harmonics from the lab electrical power, plus a number of additional narrow-band frequency spikes associated with the drive circuitry for the electro-optic modulator (Figure 2.6). The probe noise spectrum in Figure 2.9 demonstrates that these observed narrow-band spikes mostly consist of actual magnetic fluctuations and/or fluctuations in the optical pump beam pulse phase rather than induced fluctuations in the detection electronics: when the optical pump beam is physically blocked but otherwise operating exactly as it did for collection of the remaining spectra, the narrow-band spikes mostly disappear, as does much of the low-frequency noise background. This behavior is evident also in the differential scalar noise spectrum shown in Figure 2.10, where blocking the optical pump beam dramatically reduces the observed narrow-band spikes and low-frequency noise. As noted above, the detection electronics are more vulnerable to electromagnetic interference in the differential scalar measurement: the polarimeter signal for each detection zone (Figure 2.5) is single-ended for the differential scalar measurement, while for the single-channel scalar measurement the polarimeter circuitry generates a differential output pair for transmission to the lock-in amplifier, resulting in cancellation of a substantial majority of electromagnetic interference effects (largely common-mode between the differential channels).

In the case of the differential scalar measurement, the observed noise is shown in figure 2.10; for a nominally uniform applied oscillating magnetic field that was applied

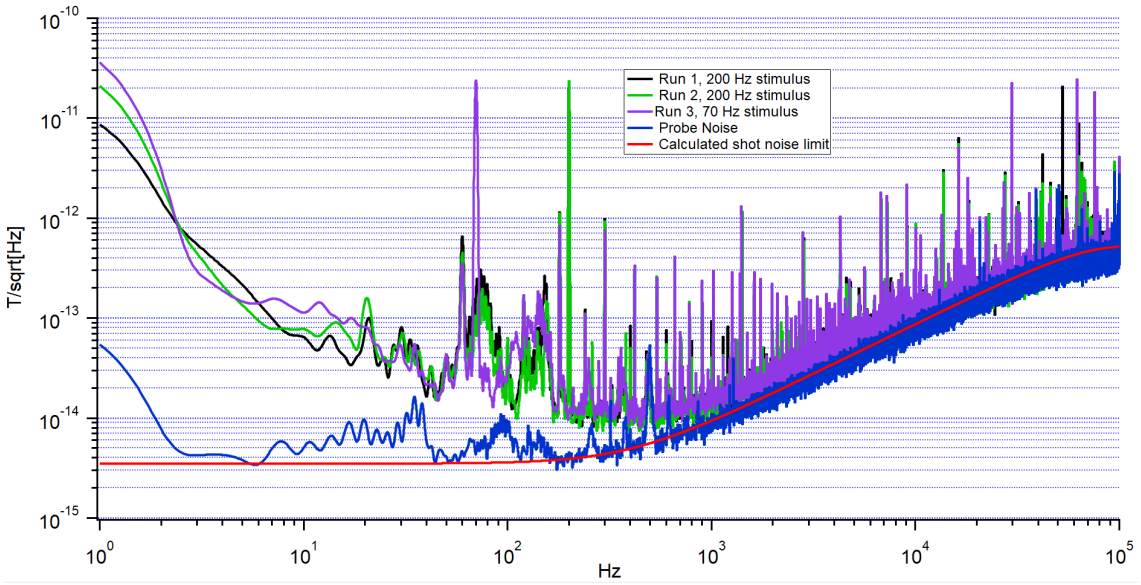

Figure 2.9: (Color online) Black, green, and purple traces: single-channel scalar magnetometer noise spectrum in a $29\mu T$ bias field for three individual measurements. Blue trace: noise background observed when blocking the optical pump beam; represents the sum of probe noise and technical noise. Red trace: calculated photon shot noise limit based on equation 2.38.

using the uniform Z axis magnetic field coil in the Twinleaf MS-2 magnetic shield set the measured common-mode rejection ratio (CMRR) at 20 Hz is approximately 3000. As shown in Figure 2.10, the measured differential scalar noise for the adjacent pair of vapor cells reaches approximately 1 $fT/cm/\sqrt{Hz}$ at around 200 Hz with a measured probe noise limit of 2 fT/cm/$\sqrt{Hz}$ at 1 Hz. Given the 9 cm baseline, this result is consistent with a per-instrument noise of approximately 6 $fT/\sqrt{Hz}$. Compared to other all-optical differential magnetometers capable of detecting low-frequency (less than 1 kHz) differential magnetic fields in Earth field with cm-scale baselines (for example, Sheng, A. R. Perry, et al. 2017, M. E. Limes et al. 2020, V. G. Lucivero et al. 2021, and S. Wu et al. 2023) the present results shown in Figure 2.10 represent an improvement in sensitivity, approaching the best demonstrated differential scalar sensitivity (Sheng, S. Li, et al. 2013) of 0.5 $fT/cm/\sqrt{Hz}$, achieved at approximately 7.3 μT as compared to the 29 μT bias field used in the present work.

Compared to an otherwise-equivalent spin-exchange relaxation free (SERF) magne-

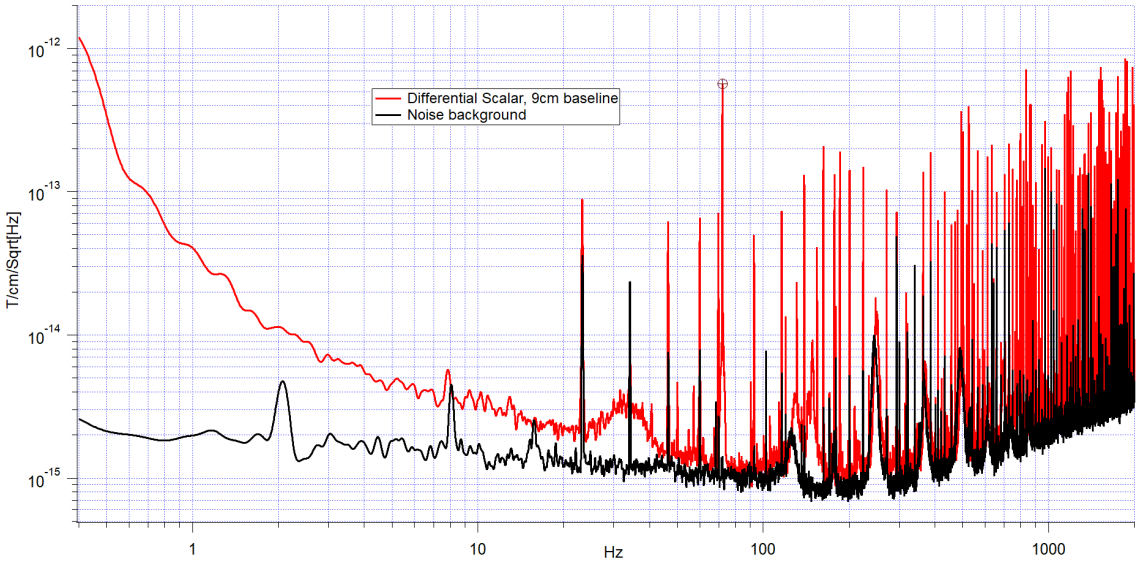

Figure 2.10: (Color online) Red trace: two-channel differential scalar magnetometer noise spectrum in a $29\mu T$ bias field. Black trace: probe noise background observed when blocking the optical pump beam; represents the sum total of optical probe noise and technical noise.

tometer (Allred et al. 2002) operating in near-zero magnetic field, the fundamental limits of the synchronously pumped atomic magnetometer described herein are noisier in absolute terms because Γ_2 is significantly greater in the present work (Equation 2.39): spin-exchange relaxation plays a much greater role in this experiment than in a SERF magnetometer. The results presented herein nonetheless demonstrate measured single-channel sensitivity (noise floor) results comparable to the observed noise floor in many SERF magnetometers (U. Li et al. 2018; I. A. Sulai et al. 2019). Further, the magnetometer described in this thesis demonstrates this noise level in a magnetic bias field orders of magnitude too large to allow SERF regime operation (Allred et al. 2002), and at a much lower vapor cell temperature (+85 degrees C versus typical temperatures greater than +140 degrees C) and in addition at lower optical pump and probe power. For future biomedical applications, the present work has demonstrated magnetic gradient sensitivity comparable with many SERF magnetometers and superconducting quantum interference devices (SQUIDs) (Yang et al. 2016) at a baseline (distance between adjacent sensitive elements) relevant to magnetocardiography (I. A. Sulai et al. 2019; Bison et al. 2009) and

magnetoencephalography (Garachtchenko et al. 1999), and with an all-optical implementation amenable to configuration as a non-interfering array of sensors.

2.6 Conclusions

In this chapter, I have presented the basic theory of operation of a synchronously pumped magnetometer, including descriptions and theory detailing the physical basis underlying the ability to drive and observe coherent spin precession about an incident magnetic field as a means of observing the magnitude of that field. I have presented a description and theory for the fundamental mechanisms by which the coherence of the spin ensemble degrades over time, along with a description of how the coherence time varies with polarization. I have presented theory showing the fundamental limits of magnetometer noise at the standard quantum limit, along with an analysis of noise optimization and physics-based procedural tuning for minimum magnetometer noise. I have utilized this theory to generate a finite element model that has demonstrated good agreement with experimental results, allowing for a priori analysis and optimization of alternative experimental configurations.

Using the provided theoretical and conceptual basis, I have demonstrated an all-optical alkali scalar magnetometer amenable to array configurations and demonstrating sensitivity consistent with bias field noise limitations, comparable to the observed sensitivity of a number of SERF magnetometers and gradiometers (I. A. Sulai et al. 2019; U. Li et al. 2018). I have further demonstrated a one-dimensional and two-sensitive-element array of such instruments with a 9 cm baseline, showing differential scalar magnetic field detection with 1 fT/cm/$\sqrt{Hz}$ differential noise at approximately 200 Hz; this differential result is consistent with an instrument noise of 6 $fT/\sqrt{Hz}$. The instrument has been demonstrated to achieve this high sensitivity while operating in Earth-field-scale magnetic fields of 29 micro-Tesla.

Chapter 3

Vector Magnetometry using A Scalar Magnetometer

3.1 Introduction

In this chapter, I present an introduction to the method of measurement of vector components of the magnetic field incident upon any scalar magnetometer through application of oscillating magnetic fields along the axis or axes to be measured; I detail and demonstrate a means of self-calibration of the vector measurements relative to the scalar measurement accuracy. Three methods of closed-loop feedback are discussed and demonstrated using the magnetometer described in Chapter 2, with -3 dB magnitude response bandwidth up to 19 kHz. Measurement uncertainty in the observation of the magnetic field vector components is discussed and analyzed, showing contributions from scalar noise, feedback loop uncertainty, offset errors, and mixing of harmonics of the measured applied oscillating field. Signal processing and filtering are discussed, including discussion and demonstration of an optimal filter set based on the uncertainty analysis. Next, experimental results are presented for each of the three feedback methods, for applied fields oscillating at four different frequencies, at four different amplitudes each. This chapter will conclude with discussion and interpretation of the vector measurement results, along with recommendations for

future work.

Recall from Chapter 2 that our work utilizes a Bell–Bloom (Bell and Bloom 1957; Bell and Bloom 1961) magnetometer with a single optical axis, implemented with intensity modulation of an optical pump beam along $\hat{R}$ passing through a vapor cell (a 1 cm diameter by 1 cm length internal dimension cylinder containing isotopically enriched ^{87}Rb and nitrogen buffer gas) to drive coherent spin precession of ^{87}Rb spins in an Earth-field-scale magnetic field. The intensity of the optical pump is modulated as a series of short-duty-cycle pulses in a manner similar to that described in (Gerginov and S. K. S. Knappe 2017). The optical pulse repetition rate is approximately resonant with the natural Larmor precession frequency ω_L of the spins, with a first harmonic component $cos(\omega t)$, where $\omega \approx \omega_L$. A linearly polarized optical probe beam co-propagating with the pump measures the $\hat{x}$ projection of the spin polarization vector $\mathbf{P(t)}$; the linear polarization of the optical probe rotates proportional to $\mathbf{P} \cdot \hat{x}$ (Equation 2.24). The polarization rotation of the optical probe beam is measured using a balanced polarimeter with a custom differential transimpedance amplifier circuit.

3.1.1 Vector Measurement Using a Scalar Magnetometer

In general, by applying three spatially orthogonal oscillating magnetic fields to the inherently scalar magnetometer, each vector component of the incident magnetic field may be extracted from the resulting modulation of the overall measured measured magnetic field (T.G. Walker and M.D. Bulatowicz 5 April 2022), herein based on the natural Larmor precession frequency of the spins. For each vector direction $\hat{i}$, the magnetic field component along $\hat{i}$ takes the form $B_i(t) = B_{i,0}(t) + B_i' sin(\omega_i t)$. Given three orthogonal vector directions ($\hat{x}$, $\hat{y}$, and $\hat{z}$ in the instrument reference frame, for example) the total magnetic field vector $\mathbf{B}$ observed by the instrument is

$$|\mathbf{B}| = \sqrt{\sum_i B_i^2} \tag{3.1}$$

The squared magnitude along each $\hat{i}$ can be written as the square of the sum of the

low-frequency component $B_{i,0}$ and modulation component $B_i' sin(\omega_i t)$:

$$B_i(t)^2 = (B_{i,0} + B_i' sin(\omega_i t))^2 = B_{i,0}(t)^2 + 2B_{i,0}(t)B_i' sin(\omega_i t) + \frac{B_i'^2}{2}(1 - cos(2\omega_i t)) \quad (3.2)$$

As a result, it is possible to find both $B_{i,0}$ and B_i' by demodulating the square of the measured magnetic field (Larmor frequency as observed by way of the pump pulse repetition rate) at the first and second harmonics of the applied fields $B_i' sin(\omega_i t)$. As the measured quantity is specifically the pump pulse repetition rate, the success of this method depends on the ability to measure and respond to each applied $(B_i' sin(\omega_i t))$. A top-level block diagram of the implemented algorithm is shown in Section 3.3. This chapter compares three feedback methods for tracking the Larmor frequency, with the ultimate goal of minimizing errors in vector calculations for a full three-axis implementation. As a first step toward this goal, the work presented herein implements only a single modulation field, superimposed on the bias field such that $|\mathbf{B}|^2 = (B_{z,0} + B_z' sin(\omega_z t))^2$, significantly simplifying the analysis and interpretation of results as compared to a full 3-axis implementation.

Note that in Equation (3.2), the assumption is made that the applied magnetic fields form an orthogonal basis set. In reality, effects such as build tolerances, mechanical stresses, differential thermal expansion, and so on guarantee that there will exist some finite deviation from orthogonality of the magnetic field coils producing these fields. As shown in (Gravrand and A. K. e. al 2001), one may form an orthogonal basis set from the three magnetic field coils using a carefully measured mapping matrix.

3.2 Experimental Apparatus and Methods

A block diagram of the updated apparatus is shown in Figure 3.1. As in Chapter 2, at the core of the experiment is a cylindrical glass vapor cell (1 cm internal diameter by 1 cm internal length containing a droplet of ^{87}Rb and 0.8 amagat N_2. The vapor cell is surrounded by ceramic RF heating coils that are designed to minimize induced magnetic

fields (M. Bulatowicz 30 March 2012) and thermal insulators consisting of aerogel sheets to maintain a ^{87}Rb vapor pressure of approximately 2-3 $\times$ 10^{12} cm^{-3} using a heat power dissipation of 0.3 W.

As described previously, a Twinleaf CSUA-1000 current supply drives the current through one of the uniform field coils to generate an ultra-low noise bias field on the order of 29 μT, allowing measurement and verification of the instrument noise floor down to approximately 10 fT/$\sqrt{Hz}$, an impressive fractional noise value of roughly -190 dB/$\sqrt{Hz}$. Using a function generator to provide a sinusoidal driving signal, perturbations up to 267 nT can be superimposed on the bias field through the CSUA modulation input; this was insufficient for the largest-amplitude modulation signals applied in this experiment, so the CSUA-1000 is placed in parallel with a custom current supply circuit capable of significantly larger modulation fields but with a white noise floor of approximately 60 fT/$\sqrt{Hz}$ and a 1/f noise limit of approximately 2 pT/$\sqrt{Hz}$ at 0.1 Hz, thereby dominating the observed magnetic noise spectrum.

In contrast to the apparatus configuration used for the work described in Chapter 2, the PXIe-based implementation has been updated to provide for closed-loop operation using a PXIe-5171R reconfigurable oscilloscope module that is installed in the same chassis as the PXIe-6614 precision timing module and is configured to use the PXIe-6614 reference time-base for high-precision, stable timing. The PXIe-5171R module includes a Xilinx Kintex-7 410T field-programmable gate array (FPGA) and utilizes a relatively small fraction of the FPGA's capability for the module's oscilloscope functionality, leaving most of the FPGA's resources available for user-programmable functionality. We have programmed this FPGA using NI LabVIEW to provide for closed-loop operation of our magnetometer with data collection functionality.

Instead of using a lock-in amplifier for observation and demodulation of the polarimeter preamp signal, in this work the electrical signal from the polarimeter preamp circuit is directly digitized using the PXIe-5171R analog input, which uses an analog-to-digital converter with 14-bit resolution at 250 million samples per second. The (FPGA) on board

the PXIe-5171R reads the digitized signal and performs real-time least-squares fitting of the observed polarimeter signal to measure the phase response of atomic spins to a precision of 47 bits in 0.43 μs as compared to a digital reference model consisting of $cos(\omega t)$ and $sin(\omega t)$ components synchronized to the optical pump pulse trigger signals. Closed-loop digital feedback adjusts the pump pulse repetition rate ω to drive $\omega \rightarrow \omega_L$ by any of the three feedback methods as described herein, and a digital logic output controls the optical pump pulse state ("on" is a logic 1, and "off" is a logic 0) with 8 ns time discretization based on the 125 MHz FPGA "clock speed." The pump pulse repetition rate is controlled by a direct digital synthesis (DDS) frequency synthesizer with 64-bit precision, based on the FPGA clock (see Appendix A.3 for more detail). As in the work described in Chapter 2, this experiment uses an optical pulse shuttering system based on a digitally triggered electro-optic modulator with a high-speed half-bridge for EO voltage control.

Just as in Chapter 2, the atomic vapor is polarized using a circularly polarized pump laser tuned near to the 795 nm D1 line of ^{87}Rb and pulsed with a short duty cycle at a repetition rate approximately equal to the natural Larmor precession frequency in the magnetic bias field. However, for this experiment the pump pulse repetition rate is controlled in a closed-loop fashion by any of three methods. The closed-loop feedback described below updates the DDS frequency (and phase, if applicable) to drive the pump pulse repetition rate to the natural Larmor precession frequency and phase in the presence of perturbations to the scalar field observed by the sensor, and the DDS frequency is captured and recorded as representative of the Larmor precession frequency.

As described in Equation 2.36, differences in the digitally perceived spin precession phase δ_d as compared to the actual spin precession phase δ relative to the optical pump beam will lead to frequency offsets and sensitivity asymmetry in the magnetometer output. Ideally, one may generate a simple offset Δ_δ to compensate for the phase difference; this will include components consisting of a simple time delay due to the latency in the closed-loop system as well as phase error based on the analog response of the polarimeter

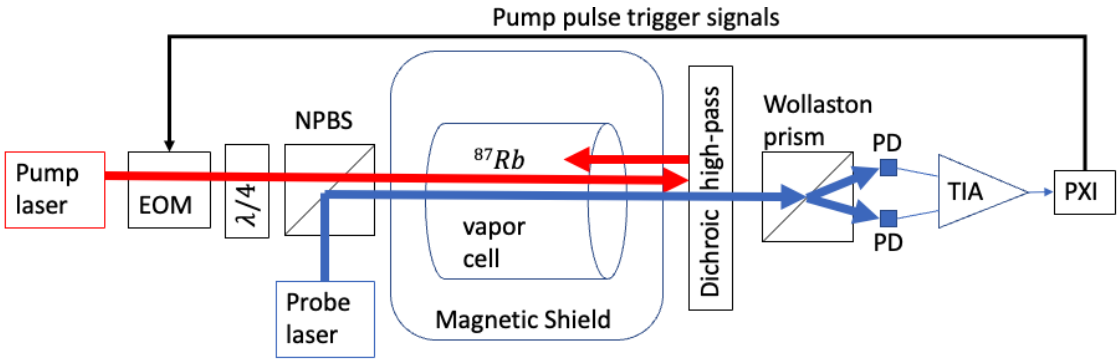

Figure 3.1: Block diagram of the experimental apparatus. The 795 nm optical pump beam pulses are generated using a continuous-wave laser with a custom shuttering system based on an electro-optic modulator (EOM). The pump beam is circularly polarized using a quarter-wave plate ($\lambda/4$). A non-polarizing beam splitter cube (NPBS) combines the optical pump and probe beams such that they co-propagate into the magnetically shielded enclosure and through the ^{87}Rb vapor cell. On the opposite side of the magnetically shielded enclosure is a dichroic high-pass filter designed to reflect the optical pump beam back toward the vapor cell and transmit the optical probe beam to a Wollaston prism, which functions as a polarization beam splitter; S and P polarization components of the probe beam are each sent to a respective photodetector (PD). The Wollaston prism is oriented at approximately 45 degrees relative to the unrotated plane of polarization of the probe beam such that the photodetectors generate approximately equal photocurrents in the absence of probe beam polarization rotation. The observed photocurrents are differenced and converted to a differential voltage signal using a custom transimpedance amplifier (TIA). Finally, the signal is read into the NI PXI-based digital system; feedback controls the optical pump pulse repetition rate by way of signals controlling the EOM.

circuitry. Thus, both the latency compensation and phase compensation must be tuned properly for optimal operation and for generating a true $\omega = \omega_L$ condition. For this experiment, the condition of $\omega = \omega_L$ is determined by sinusoidal modulation of the optical pump wavelength at a frequency $\omega_w \ll \Gamma_2$, driving a corresponding modulation of the polarization and transverse relaxation rate (Equations 2.35 and 2.40) with the intent of finding a feedback phase offset compensation which will generate no first-harmonic response to the modulation. In other words, when $\omega \neq \omega_L$ the polarimeter will exhibit a coherent output component at ω_w; proper adjustment of the latency compensation and phase compensation will result in no observable polarimeter output component at ω_w but instead with an output at $2\omega_w$ based on symmetric modulation about the magnetic line center.

As in Chapter 2, each pump pulse exhibits an "on" state intensity of roughly 10 mW incident on the vapor cell, and the magnetometer sensitivity under our normal operating conditions is observed to maximize at a duty cycle of 0.07, corresponding to 0.7 mW time-average optical pump power incident on the vapor cell, as measured by a Coherent® LaserCheck™ optical power meter. Between pulses, the polarized spins precess about the external bias field at their natural Larmor frequency (Equation 2.33) such that the spin polarization relative to the bias field axis can be written as $P(t) = P_\perp cos(\omega_L t + \delta) + P_\parallel$. For this experiment, the bias field is once again nominally orthogonal to the optical pump beam such that $P_\parallel \to 0$. The pump pulse repetition rate is tuned near the first harmonic of the natural Larmor precession frequency of the spins in the scalar magnetic field observed by the instrument.

As described above, a linearly polarized CW (continuous wave) probe laser passes through the cell to track the spin-dependent index of refraction of the ^{87}Rb vapor via Faraday rotation. This polarized light is detuned multiple linewidths away from the broadened ^{87}Rb D_2 optical resonance near 780 nm in order to reduce the spin relaxation effects of photon scattering from the probe light and correspondingly optimize magnetometer sensitivity (Section 2.4.1), and exhibits an optical power of 3 mW incident on the polarimeter.

The angle ϕ of rotation of the linear polarization of the detected probe light then follows $\phi_{pr}(t) \propto N\hat{x} \cdot P(t)$, where N is the number of spins interacting with the probe beam and the probe is propagating along $\hat{x}$. The resulting polarization rotation angle is measured with a balanced polarimeter; for small polarization rotation angles, the differential photocurrent is proportional to the rotation angle. Given a pair of photodetectors in the balanced polarimeter with photocurrents I_1 and I_2,

$$\phi_{pr} \approx \frac{1}{2}\frac{I_1 - I_2}{I_1 + I_2} \tag{3.3}$$

which is an approximation restatement of Equation 2.25 and only holds well in the small ϕ_{pr} limit. Recall from Equation 2.25 that the rotation ϕ_{pr} of the probe beam as it passes through the polarized alkali vapor is

$$\phi_{pr} = \frac{1}{2} sin^{-1}\frac{I_1 - I_2}{I_1 + I_2} \tag{3.4}$$

In our experiment, the output of the custom polarimeter has a gain of 10 kV/A and the typical output waveform arising from ϕ_{pr} is approximately 1V (0.1 mA) amplitude corresponding to 1.5 mA total photocurrent. Thus, $\phi_{pr} \approx 0.033$ radians, for less than 1 part per thousand deviation from a perfectly linear response. For the purpose of this experiment, then, the waveform is well-approximated by a sinusoid and Equation 3.3 provides a good approximation.

The total noise output from the polarimeter when the probe is being measured is consistent with the photon shot noise limit (Figure 2.9 and Appendix A.2). The polarization angle noise $\delta\phi$ in a 1 Hz bandwidth for small angles is based on the electrical current shot noise from the photodetectors, given elementary charge q on a single electron:

$$\delta\phi_{pol} \approx \frac{1}{2}\frac{\sqrt{2q(I_1 + I_2)}}{I_1 + I_2} = \frac{1}{2}\sqrt{\frac{2q}{I_1 + I_2}} \tag{3.5}$$

For a 3 mW probe at 780 nm wavelength, the silicon phototdetectors provide a responsivity of slightly over 0.5 A/W for a total polarization rotation noise of approximately

7 nano-radians per square root Hz (nrad/$\sqrt{Hz}$). The measured slope of the response ($\frac{d}{dB}(I_1 - I_2)$) during this experiment was typically in the range of 3000 to 5000 amps per Tesla; based on Equation (3.5), at low frequencies $\omega \ll \Gamma_2$, where Γ_2 is the transverse spin polarization relaxation rate, the photon shot noise limit of magnetic field detection is therefore at or below 7 fT/$\sqrt{Hz}$, well below the observed total magnetic noise. The decrease in magnetic sensitivity (increase in photon shot noise) as compared to the experiment in Chapter 2 is attributable to condensation of ^{87}Rb on the optical windows, partially obstructing the optical path and reducing the available optical pumping rate and probe photon flux.

The method of pulsing the optical pump beam at a rate of approximately $\omega = \omega_L$ effectively pumps the spins in their rotating reference frame; as discussed in Chapter 2 the Fourier transform of a sequence of square pulses contains the pulse repetition rate as a major component. Starting from the Bloch equation for spins in a magnetic field, it can be shown (A. Perry et al. 2020) that the observed phase difference ϕ between the spins and the pump pulses near resonance corresponds to the difference $\delta\omega$ between the pump pulse repetition rate and the natural Larmor precession frequency of the spins, and further includes contributions from the phase response ϕ_{pol} of the polarimeter circuitry and the electronics system latency δt:

$$\phi = tan^{-1}(\delta\omega/\Gamma_2) + \phi_{pol} + \omega\delta t \tag{3.6}$$

In the limit where $\delta\omega/\Gamma_2 \ll 1$, the phase shift resulting from $\delta\omega$ is directly proportional to $\delta\omega$, and the response is assumed to be linear such that

$$\phi \to \delta\omega/\Gamma_2 + \phi_{pol} + \omega\delta t \tag{3.7}$$

Each of the feedback methods investigated herein is designed to correct the pump pulse repetition rate directly using the measured phase ϕ as the error signal driving the loop. The phase shift (accumulated phase error) $\delta\phi$ is measured over some period of

time, in this case typically a single precession cycle of the spins. Noting that $\frac{d}{dt}\delta\phi = \delta\omega$, where $\delta\omega$ is the difference between the angular frequency of precession of the spins and the pump pulse repetition rate, it becomes clear that feeding back to the frequency based on the measurement of phase inevitably leads to a precession–frequency-dependent feedback gain component that can lead to instability in the closed-loop response upon increasing the scalar field magnitude and adversely affect bandwidth upon decreasing the scalar field magnitude. This gain component can be mitigated by any of a number of different methods, such as feeding back based on the product $\delta\phi T$, where $\delta\phi$ is again the accumulated phase error and T is the measurement period, rather than feeding back based directly on $\delta\phi$.

The signal-to-noise ratio (SNR) for the measurement of oscillating magnetic fields at a frequency ω_{osc} is based on the SNR at very low frequencies (SNR_0; $\omega_{osc} \ll \Gamma_2$), the frequency of interest ω_{osc}, and the SNR bandwidth $\omega_0 = 2\Gamma_2$; in the limit of high gain at ω_{osc}, this SNR is independent of the feedback method chosen. Thus, the instrument exhibits a "signal-to-noise ratio bandwidth" that is essentially independent of the closed-loop -3 dB response magnitude bandwidth. At low frequencies, then, each feedback method is expected to exhibit effectively identical SNR.

$$SNR(\omega_{osc}) \approx \frac{SNR_0}{\sqrt{1 + \frac{\omega_{osc}^2}{\omega_0^2}}} \tag{3.8}$$

3.2.1 PI Feedback

The input to the PI (proportional plus integral) gain stage in the first of the three closed-loop feedback schemes discussed herein takes the $\delta\phi$ value calculated by the least-squares algorithm and continuously calculates updates to the pump pulse repetition rate as the sum of the proportional and integral gain components. The proportional gain component is a simple multiple of $\delta\phi$, and the integral gain component multiplies $\delta\phi$ by a second gain and sends the result to a digital accumulator. A top-level block diagram is shown in Figure 3.2. For this work, the PI gain stage is tuned by maximizing the absolute gains over the

observed range of precession frequencies while avoiding instability. The maximum achieved feedback bandwidth as measured by the -3 dB response magnitude without insufficient phase margin toward the higher end of the frequency range is approximately 9 kHz.

In the limit of small ϕ_{pol} and δt, a PI loop can provide a very linear closed-loop response. Examining the response of the spins in isolation, the spin phase response exhibits a corner frequency of Γ_2/π as described above: a PI gain stage can provide a complementary behavior by tuning the ratio between the P and I components of gain such that the PI corner frequency is also equal to Γ_2/π. For a digital PI gain stage as in the present experiment, the corner frequency f_c is given by

$$f_c = \frac{I f_I}{2\pi P} = \frac{\Gamma_2}{\pi} \tag{3.9}$$

where P and I are the numerical factors multiplying $\delta\phi$ in the digital gain stage and f_i is the summing rate of the digital integrator; in our experiment, the FPGA clock frequency. In the present experiment, at Earth-field-scale magnetic fields the measurement system does not reside in either the negligible ϕ_{pol} or small δt limits, and further exhibits gain proportional to ω_L as described above. Therefore, as will be shown shortly, more-sophisticated methods of feedback provide improved performance over the PI method.

3.2.2 Nonlinear Feedback

Consider the accumulation of phase between two sinusoids, such as the precession signal and the reference signal:

$$\frac{d\delta\phi(t)}{dt} = \omega_{ref}(t) - \omega(t) \tag{3.10}$$

The rate phase accumulation is simply the difference in frequency between the two sinusoids of interest. Therefore, in a measurement period the accumulated phase is simply proportional to the frequency difference. In contrast, Equation (3.6) indicates that in the steady state limit the tangent of phase is directly proportional to the frequency difference. An important point is that Equation (3.7) holds only for the following cases: (1) in a

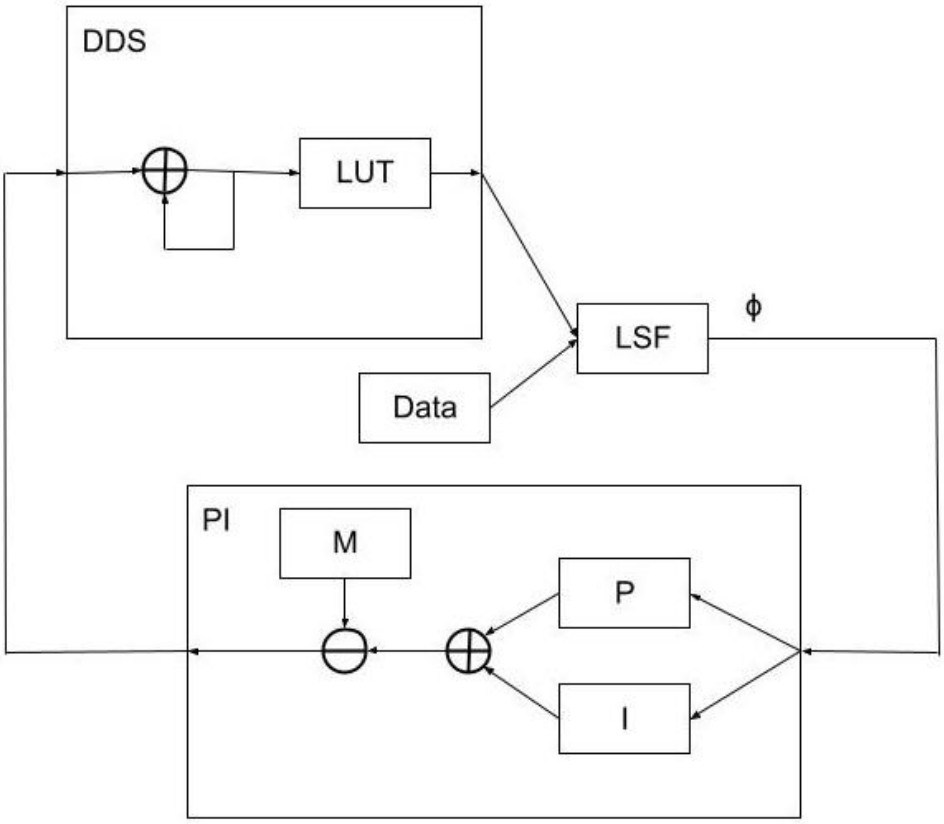

Figure 3.2: A top-level block diagram of the PI feedback scheme. The block labeled DDS is the digital representation of the Rb spin precession phase and frequency and includes a look-up table (LUT) to convert the DDS phase word (register value) into a sinusoidal model of the spin precession; its output is compared to the incoming digitized precession signal (data) in a least-squares filter (LSF) that outputs the value of $\delta\phi$. $\delta\phi$ is then used to drive the PI gain stage (block labeled PI). The result of the PI calculation modifies the DDS phase increment word M.

steady-state condition and (2) only for small phase offsets. One may more accurately capture a portion of the nonlinear response of phase to rapid deviations in precession frequency through a slightly more sophisticated method. More generally, a shift in the ambient field is detected as a temporary shift in the precession frequency relative to the reference frequency (Equation (3.10)); recall that between pump pulses the spin ensemble freely precesses at the natural Larmor precession frequency. Comparing in discrete time the most recent measurement of phase at time interval n ($\phi[n]$) to the previous measurement of phase ($\phi[n-1]$), based on the time between measurements $T_{ref}[n]$, one may deduce the shift in resonant frequency from the previous to present measurements:

$$\frac{\phi[n]-\phi[n-1]}{2\pi T_{ref}[n]} = f_{ref}[n] - f[n], \tag{3.11}$$

where f_{ref} is the reference frequency to which the actual data are being compared (the output of the DDS block in Figure 3.3, representing the co-rotating component of R_{op}). Making a first-order approximation of the time derivative of Equation (3.11) and inserting the result into Equation (3.10), it is possible to solve for the present actual resonant frequency $f[n]$ of the spins (Equation (3.11)). One may then predict a first-order approximation of the expected precession frequency $f[n+1]$ at the next measurement interval and preemptively update the model ($f_{ref}[n+1]$) by way of the DDS phase increment word M. From this, a feedback scheme is constructed, which has a similar form to the PI gain stage (Equation (3.12)):

$$f_{ref}[n+1] = f_{ref}[n](1 - K_p(\phi[n]-\phi[n-1]) - K_i\phi[n]) \tag{3.12}$$

A proportional term (K_p) approximates the derivative between consecutive phase terms, while an integral term (K_i) approximates the derivative to zero phase. Conceptually, this scheme can be seen as a translation from a derivative-proportional (DP) controller into a PI (proportional-integral) controller via a frequency-dependent multiplicative factor. So, this method captures both the phase deviation itself and a multiple of its time

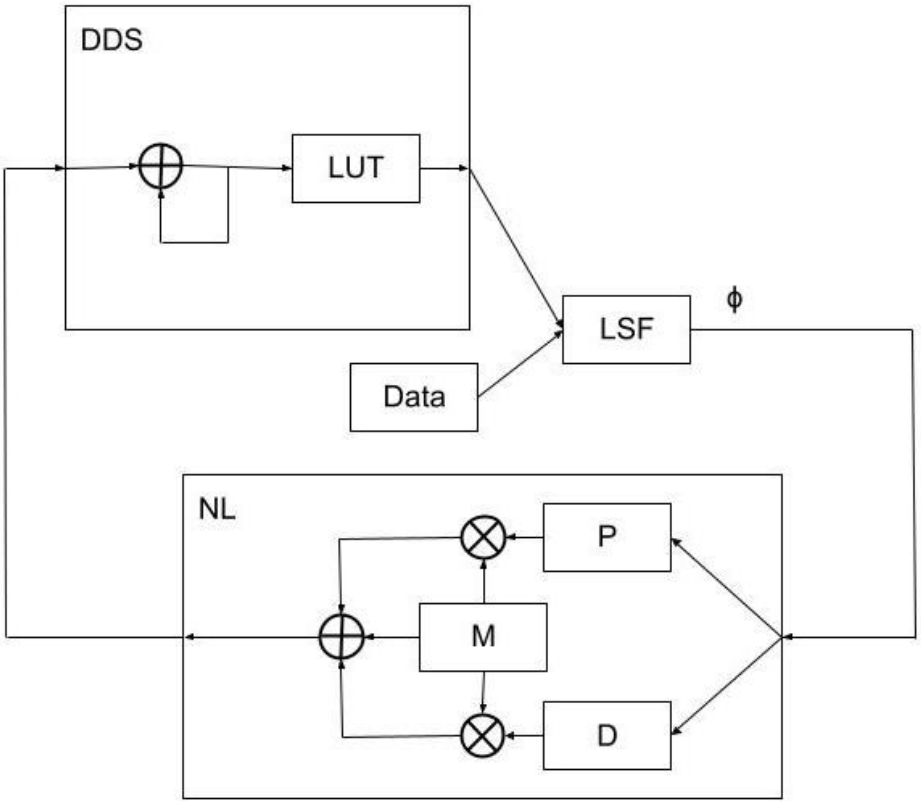

Figure 3.3: A top-level block diagram of the non-linear feedback scheme.

derivative, and therefore generates a gain response that is nonlinear in phase deviation. A top-level block diagram is shown in Figure 3.3. For this work, the gain stage is tuned to maximize the closed-loop -3dB response bandwidth at approximately 17.5 kHz.

3.2.3 Hybrid Self-Oscillator

Based on Equation (3.6), it can be understood that control of the pump pulse repetition rate is required in order to drive $\delta\phi \rightarrow 0$. In a "pure" self-oscillator, the periodic incoming data will directly generate the driving signal. Stated another way, rather than driving the frequency in order to alter the phase, the phase of the pump pulses in a "pure" self-oscillator is driven in order to alter the frequency.

In the hybrid self-oscillator method, the phase deviation $\delta\phi$ of the periodic input $\propto P(t)$

directly drives the phase of both the pump pulses and the reference sinusoid. However, the frequency of the reference must be deduced based on the phase to ensure that the drive frequency matches the reference frequency. In discrete terms, the number of steps taken by the DDS accumulator in one period follows as $N = 2^n/m$, where m is the DDS phase word and n is the bit width of the accumulator. A non-zero phase can be corrected with a shift in the size of the accumulator with a new phase word $m' = (2^n + K_i'\phi)/N$. Reorganizing these terms results in an updated phase word m' and a third feedback scheme:

$$m' = m(1 - K_i\phi) \tag{3.13}$$

For a "pure" self-oscillator approach, direct feedback of the measured phase response as a phase shift in the timing of the optical pump pulses now takes the place of the proportional feedback in the PI and nonlinear feedback schemes. For the PI and nonlinear approaches, the proportional feedback term directly modifies the repetition rate of the optical pump pulses rather than directly modifying their phase. However, since the pure self-oscillator feedback approach does not directly influence the closed-loop -3 dB response bandwidth, it was found to be beneficial to implement a combination of both phase and proportional feedback; hence, it was designated as a hybrid self-oscillator based on this mixing of the nonlinear and self-oscillator methods. A top-level block diagram is shown in Figure 3.4. For this work, the response bandwidth was maximized at approximately 19 kHz.

3.2.4 Feedback Loop Summary

A comparison between the three feedback loop schemes may be understood qualitatively as follows. First, the PI scheme measures the phase difference between the DDS model of the expected precession signal and the actual signal itself and directly uses this phase deviation to update the pump pulse repetition rate (and DDS phase increment word). The PI scheme is therefore only reactive—it responds to a measured phase deviation and makes corrections. Second, the nonlinear scheme takes advantage of the time derivative

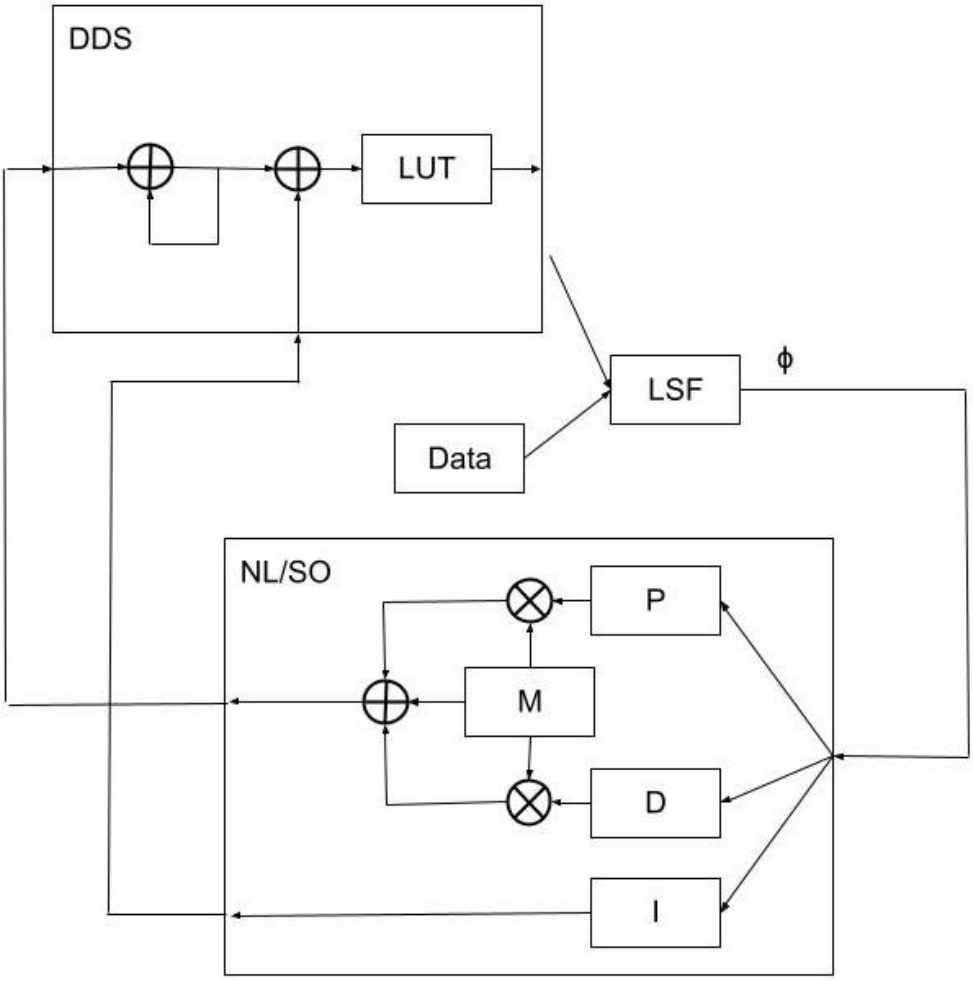

Figure 3.4: A top-level block diagram of the hybrid self-oscillator feedback scheme.

of the phase to predict the next observed spin precession frequency and updates the DDS phase increment word accordingly. The nonlinear scheme is therefore both reactive and predictive; it deliberately seeks to predict the next observed signal increment rather than only responding to the presently observed signal increment. Finally, the hybrid scheme takes the nonlinear scheme and adds a direct phase modification of the next pump pulse based on the observed phase of the present signal with respect to the model (DDS). The hybrid scheme is therefore reactive and predictive, and includes an additional correction factor for further improvement of the timing of the optical pump pulses to coincide with the resonant precession of the spins.

While the PI feedback scheme may accurately correct for frequency offsets, for increasing dB/dt, the latency δt in calculating $\delta\phi$ and updating the frequency (DDS phase increment word M) increasingly limits the phase margin. Predictive modification of the pump pulse repetition rate as in the nonlinear scheme recaptures some of this margin. Meanwhile, a direct adjustment to the phase as in the hybrid self-oscillator feedback mechanization can be expected to allow for faster response times to larger dB/dt, as it does not solely rely on the accumulation of phase inherent in the $\delta\phi$ error signal calculation that drives the PI and nonlinear schemes. Thus, at larger values of the frequency–magnitude product $\omega_i B_i'$ (i.e., a larger dB/dt) the hybrid scheme can be expected to more closely track the spin precession frequency perturbation induced by the applied oscillating magnetic fields as compared to the PI or nonlinear schemes.

3.2.5 Measurement Uncertainty

As shown in Equation 3.2, measurement of the vector components of the incident magnetic field requires observation of the first- and second-harmonic components of the square of the measured total magnetic field in the presence of a modulation applied along the axis for which the vector component is to be observed. Uncertainty in the measurement of these components, such as that arising from the finite gain of the feedback loop, will result in uncertainty in the calculated vector component solution. A key point in the

evaluation of the effects of uncertainty in the closed-loop response is that the instrument is inherently a scalar magnetometer. Extension of the instrument's operation to vector magnetic field measurement is achieved through applied modulating magnetic fields and by way of processing the signals in magnetic-field-squared space.

The scalar magnetic field B_s is perceived by the closed-loop measurement system as measurement value M. Note that M is simply an appropriately scaled version of the DDS phase increment word m mentioned above, converted into magnetic field units: the instrument in the present work is a magnetic-field-to-frequency transducer by way of the relationship between the scalar field, frequency, and the gyromagnetic ratio γ of the spins: $\omega = \gamma B_s$. The value of M includes the actual scalar magnetic field B_s at any particular epoch and an additional uncertainty δB, which includes effects from the finite gain of the feedback loop as well as noise and effects from any applied filtering. Thus, the vector measurement portion of the system perceives

$$M^2 = (B_s + \delta B)^2 \tag{3.14}$$

One may expand the B_s term as a function of time, defining the static (low frequency) portion of each vector component as $B_{i,0}$ with applied modulation of amplitude B_i' and frequency ω_i:

$$B_s^2(t) = \sum_i (B_{i,0} + B_i' cos(\omega_i t))^2 \tag{3.15}$$

where B_0 is the low-frequency component of the incident magnetic field; here, low frequency is defined as lower than ω_i. In the general case $i = \{\hat{x}, \hat{y}, \hat{z}\}$ and it is assumed that modulation is applied along three orthogonal components of the incident magnetic field (i.e., modulations along $\hat{x}$, $\hat{y}$, and $\hat{z}$ in the instrument reference frame). In this work, as a first step toward 3-axis measurement, a single oscillating field is applied along the bias field to simplify analysis and interpretation of the experimental results, reducing Equation 3.15 to simply

$$B_s^2(t) = (B_0 + B'cos(\omega t))^2 \tag{3.16}$$

One may separate δB into its Fourier components at integer multiples of ω to provide additional insight:

$$\delta B = \sum_{k=0}^{\infty} \delta B_k cos(k\omega t + \phi_k) \tag{3.17}$$

Combining Equations 3.14, 3.16 and 3.17 yields

$$\begin{aligned} M^2 = B_0^2 + 2B_0B'cos(\omega t) + B'^2cos^2(\omega t) \\ +2\sum_{k=0}^{\infty}[\delta B_k cos(k\omega t + \phi_k)(B_0 + B'cos(\omega t))] \\ +(\sum_{k=0}^{\infty}\delta B_k cos(k\omega t + \phi_k))^2 \end{aligned} \tag{3.18}$$

Equation 3.18 demonstrates that one may measure the amplitude of the applied oscillating field based on demodulation of the square of the scalar field at 2ω (note: $cos^2(\omega t) = \frac{1}{2}[1 + cos(2\omega t)]$); this result combined with demodulation of the square of scalar field at ω provides a solution for the vector component of magnetic field along the applied oscillating field direction. Equation 3.18 also clearly demonstrates that the process of squaring the magnetic field will generate the mixing of harmonics; particularly relevant are mixed components that result in observed frequency content at ω and 2ω. Significant benefits can therefore be realized through appropriate filtering of the scalar field before and after the squaring operation, prior to demodulation.

This work utilizes a sinc (in frequency) filter prior to squaring (more details will be provided below); a bandpass filter at ω prior to squaring for detection of the 2ω component; and bandpass filters at ω and 2ω after squaring (Figure 3.5). In this work, $B' \leq 534$ nT (3740 Hz precession frequency perturbation amplitude), while $B_0 \approx 29{,}000$ nT (200 kHz precession frequency amplitude); thus, in Equation 3.18, it becomes apparent that $B'^2 \ll 2B_0B' \ll B_0^2$. Given the presence of noise in the measurement, then, the dominant source of uncertainty in the measurement of B_0 by way of the vector component measurement technique described in Equation 3.2 is the uncertainty in the measurement of B':

$$B'_{measured} = B'\{1 + \frac{2\delta B_1 cos(\phi_1)}{B'} + 2\sum_k \frac{\delta B_k \delta B_{k+2}}{B'^2}[cos(\phi_k + \phi_{k+2}) + cos(\phi_k - \phi_{k+2})]\}^{\frac{1}{2}} \tag{3.19}$$

Equation 3.19 demonstrates that, in general, the uncertainty can reasonably be expected to decrease with increasing amplitude B' of the applied oscillating field in addition to benefiting from any filtering prior to the squaring operation that reduces the $\delta B_{k\neq 1}$ components. Additionally notable is that an increase in the feedback loop gain and improvement in phase response at $k\omega$ will suppress any feedback loop contributions to the uncertainty shown in Equation 3.19. Though not explicit in Equation 3.19, each δB_k includes uncertainty $\delta B_{k,noise}$ from the instrument noise as well as uncertainty $\delta B_{k,feedback}$ based on the finite gain of the closed-loop system. Each δB_k also an offset δB_{offset}, which may arise from such effects as any noise rectification. One obvious source of noise rectification based on the feedback methods described above is the use of $\delta\phi$ to feed back to $\delta\omega$: as noted above, the feedback gain is proportional to the precession frequency, eliciting nonlinearity and corresponding asymmetry in the feedback loop response to an applied sinusoidal oscillating field. Even-order terms in this nonlinearity will rectify a portion of the noise.

The error term $\delta B_{k,feedback}$ can be understood as follows. The closed-loop system includes a transfer function $G(2\pi f)$ as a function of frequency f for the instrument and electronics along with a feedback transfer function $K(2\pi f)$, resulting in a finite open-loop transfer function $GK(2\pi f)$. The residual error $\delta B_{k,feedback}$ in the presence of applied oscillating field B' due to the finite response of the closed loop system is therefore proportional to the magnitude of the applied oscillating field:

$$\delta B_{k,feedback} = B'\frac{1}{1 + GK(k\omega)} \tag{3.20}$$

In the limit that $\delta B_{k,feedback} \gg \delta B_{k,noise}$, the contribution to uncertainty in the measurement of B' arising from the feedback loop will dominate. As described in Equations

3.19 and 3.20, the uncertainty will no longer appreciably decrease with increasing amplitude B'. Thus, for $G(2\pi f) \rightarrow fixed$, an improvement in the feedback loop transfer function becomes the sole means of further reduction in uncertainty, which is the focus of this work. Note that for a 3-axis system, this condition will depend on the direction of the bias field relative to a respective applied oscillating field; the feedback uncertainty contribution will depend on the observed modulation of the scalar field imparted by the respective applied oscillating field. Comparing extreme cases in which the bias field is orthogonal to the applied oscillating field versus the case studied here, in which the applied oscillating field is along the bias field, Equation 3.2 demonstrates that in the extreme case, the applied oscillating field must be much larger than in the case studied here to meet the condition that $\delta B_{k,feedback} \gg \delta B_{k,noise}$.

3.3 Results

For each of the three feedback methods investigated in this work, 60 s of scalar magnetometer data were collected using each feedback loop method; in each case, an oscillating magnetic field was superimposed on the bias magnetic field by applying a modulating current through the same magnetic field coil that provides the bias field itself. These oscillating fields were applied at four frequencies (20 Hz, 200 Hz, 2 kHz, and 20 kHz) at each of four magnetic perturbation amplitudes (0.534, 5.34, 53.4, and 534 nT, corresponding to 3.74, 37.4, 374, and 3740 Hz perturbation amplitude in precession frequency units). The amplitudes of the applied oscillating fields were calibrated by way of measuring the change in spin precession frequency per unit drive signal input. For each data set, Equation (3.2) is used as the basis to solve for the vector component of the bias field that is oriented along the applied oscillating field. In this case, the bias field and oscillating field are co-aligned, simplifying the process of evaluating the accuracy of the vector field measurement as compared to the scalar magnetometer using this technique. In particular, if a result shows a high relative accuracy, the vector field component that is measured based on the ω and 2ω components of M^2 as shown in Equation (3.2) will be equal to the observed

scalar field B_0.

Each of the 48 data sets (four amplitudes at each frequency, four frequencies, and three methods) is analyzed by way of the algorithm shown in Figure 3.5 using MATLAB. The calculations shown in Figure 3.5 are implemented as follows. First, the scalar magnetometer data are upsampled using cubic spline interpolation (the "Spline" block in Figure 3.5) to increase the effective data rate of all data streams to a uniform pre-selected effective data rate, chosen such that every frequency of applied oscillating field is represented by an integer countdown of the effective data rate; this significantly simplifies the design of Sinc (in frequency) filters that may be applied to the data. The upsampled data are then mirrored about both endpoints to effectively triple the data length without introducing discontinuities and to allow for removal of filter end effects. The upsampled and extended data are filtered using a Sinc filter that is implemented as a simple moving average using the MATLAB command movmean(data,n), where n is the number of data points in the moving average. This filter suppresses undesired frequency components of M, which would lead to additional frequency mixing and corresponding uncertainty in the measurement of the 2ω component of M^2, such as noise in the vicinity of $N\omega$, where N is an even integer up to a limit imposed by the sample rate. The magnitude part of the transfer function of the Sinc filter can be easily understood in a continuous-time approximation. The average over period T of $cos(\kappa t)$ and starting at an arbitrary time $t_0 = 0$ is simply a Sinc function:

$$\int_0^T \frac{cos(\kappa t)}{T} dt = \frac{sin(\kappa T)}{\kappa T} = Sinc(\kappa T) \tag{3.21}$$

As noted in the discussion above regarding Equation 3.19, the suppression of $\delta B_{k\neq 1}$ components will minimize uncertainty in the measurement of B'; thus, prior to squaring the magnetic field for the measurement of B', a bandpass filter at ω (i.e., $k = 1$) is applied to suppress these undesired components in M. The M^2 data sets are further bandpass filtered at ω and 2ω as appropriate, and then finally truncated back to the original data length, deleting the mirrored data and eliminating the filter end effects such that the filtered data more accurately represent what might be expected in a real-time system with

fully settled filters. These filtered data sets are then demodulated at the appropriate phase to measure values corresponding to the oscillating terms in Equation (3.2) so that a solution can be found for the measurement of the vector component of field along the oscillating field direction. In each case, the bandpass filter is designed using MATLAB's built-in functionality for generating a minimum-order Chebyshev Type II filter; for maximum commonality of filter behavior across the range of frequencies, the filter bandwidth is kept at a constant fraction of the filter center frequency for both the pass-band and the stop-band, and the pass-band ripple and stop-band attenuation specifications remain constant across all filter instances.

The Chebyshev Type II filter, as implemented in MATLAB, will exhibit a nonuniform gain as a function of frequency in addition to exhibiting a non-unity gain at the desired oscillating component frequencies. Therefore, at each step in which a Chebyshev Type II filter is applied, the gain of the filter at the desired frequency is measured using a simple unity-amplitude sinusoidal input to the filter. The filtered M^2 signal is then corrected for the filter gain and passed along to the next step in the analysis.

The "Phase" block in Figure 3.5 refers to the calculation of the ideal phase for demodulation of M^2. Consider an applied magnetic field modulation component $2B_{0,i}B_{ac,i}sin(\omega_i t+\phi_B)$ (Equation 3.2), where ϕ_B is an unknown phase relationship between the modulation signal as observed in the data and the start of the data set. The ideal demodulation signal to measure the amplitude $2B_{0,i}B_{ac,i}$ of the resulting oscillation will of course be to multiply the signal by $sin(\omega t+\phi_B)$. The most precise possible value of ϕ_B can be calculated based on the entire data set–an advantage of post processing. Consider multiplication of the entire data set of a given M^2 separately by $cos(\omega_i t)$ and $sin(\omega_i t)$. Examining the effect on the $2B_{0,i}B_{ac,i}sin(\omega_i t+\phi_B)$ component of the signal and ignoring the amplitude for the moment in order to visually simplify the equations,

$$\begin{aligned}\sin(\omega_i t)sin(\omega_i t+\phi_B) &= \tfrac{1}{2}[cos(\phi)-cos(2\omega_i+\phi_B)]\\ \cos(\omega_i t)sin(\omega_i t+\phi_B) &= \tfrac{1}{2}[sin(\phi)-sin(2\omega_i+\phi_B)]\end{aligned} \tag{3.22}$$

Taking the mean of each of these outputs over the full data set (effectively eliminating the $2\omega_i$ components), one may solve for ϕ_B:

$$\phi_B = tan^{-1}\frac{mean[cos(\omega_i t) * M^2(t)]}{mean[sin(\omega_i t) * M^2(t)]} \tag{3.23}$$

This same technique for the extraction of the appropriate demodulation phase will apply to any signal of interest, and will allow the calculation of both the magnitude response and the (magnitude * phase) response of an incident signal, i.e. the in-phase and quadrature components of the signal. In a real-time system, this calculation may be implemented by way of replacing the "mean" with appropriate low-pass filtering.

Figure 3.7 shows the ratio (scale factor) between the vector component of magnetic field as measured using our vector measurement algorithm (Figure 3.5) and the magnetic field as measured by the scalar magnetometer, after correction for the gains of the filters as described above. Ideally, the vector measurement algorithm will yield exactly the same result as the scalar measurement; in such a case, the scale factor would be exactly 1. As shown in Figure 3.7, the scale factor error for our measurement method is less than 1% in all cases (excluding error bars); in many instances, the scale factor is consistent with exactly 1 within three standard deviations.

Recall from Equations 3.19 and 3.20 that it is specifically in the limit that $\delta B_{k,feedback} > \delta B_{k,noise}$ wherein an appreciable improvement in uncertainty based on the response of the feedback loop is expected. Figure 3.8 is consistent with this prediction; no clear advantage in precision is gained for the nonlinear or hybrid feedback methods over the PI method for any B' amplitude investigated herein at 20 Hz and 200 Hz, where $|GK| \gg 1$ for all three methods. Meanwhile, at 2 kHz and 20 kHz, the precision follows the expected progression of $\delta B_{k,PI} > \delta B_{k,Nonlinear} > \delta B_{k,Hybrid}$ based on the respective closed-loop response characteristics, with the difference between the nonlinear and hybrid methods being most clear at the highest frequency. It is, therefore, concluded that in this work, magnetometer noise dominates the precision of the vector measurement method shown in Equation(3.2 when $\delta B_{k,feedback} < \delta B_{k,noise}$, magnetic measurement noise dominates the scale factor

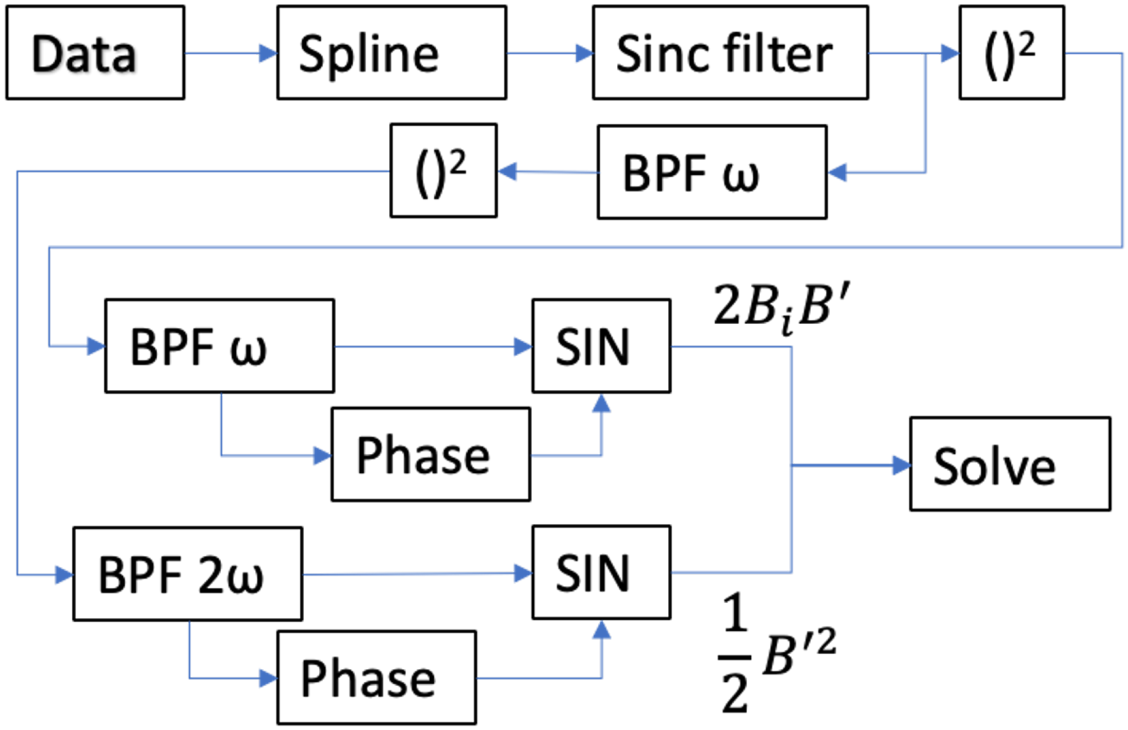

Figure 3.5: A top-level block diagram of the implemented vector calculation algorithm for a single axis, for each data set. The block labeled Spline represents cubic spline interpolation of the data for optimal sinc filtering (block labeled Sinc). After the sinc filter, the data are either immediately piecewise-squared (each data point in the time series is itself squared) or filtered first to suppress $\delta B_{k\neq 1}$ components (Equation (3.19)) and then piecewise squared. The blocks labeled BPF represent band-pass filters at ω and 2ω. The blocks labeled Phase represent phase detection to determine the appropriate demodulation phase (Equation 3.23). The blocks labeled SIN represent sinusoidal demodulation, in which the signal is multiplied by a sine wave at the appropriate frequency and phase and then low-pass filtered to observe the low-frequency component of the output; these then feed into a solver block to measure the incident vector field (B_i) and the oscillating field (B') magnitude.

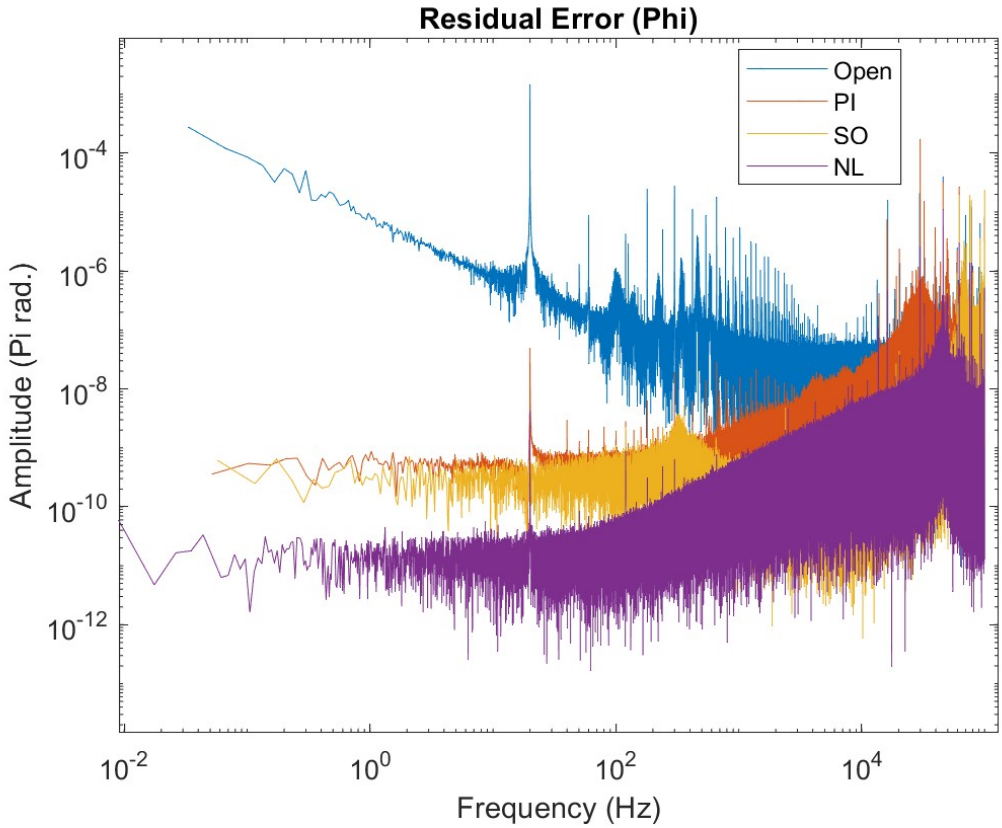

Figure 3.6: A comparison of residual errors between open loop and closed loop operation in a 29 μT bias magnetic field (200 kHz precession frequency) with a 20 Hz, 0.534 nT (3.74 Hz precession frequency perturbation amplitude) oscillation.

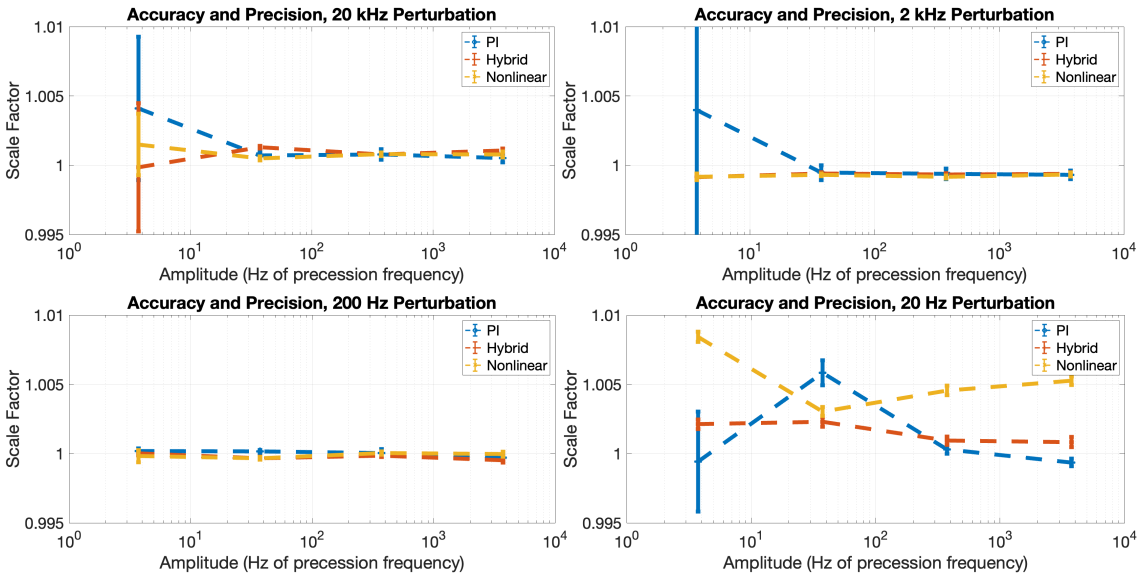

Figure 3.7: The relative accuracy of the oscillating field method compared to the scalar magnetometer (line plots with data points) and precision (error bars) of each method. The scale factor (Y axis) is the ratio between the measured vector field using the oscillating field method and the actual magnetic field as measured by the scalar magnetometer, while the precision is measured as the Allan deviation value of the measured vector time series at one second integration time.

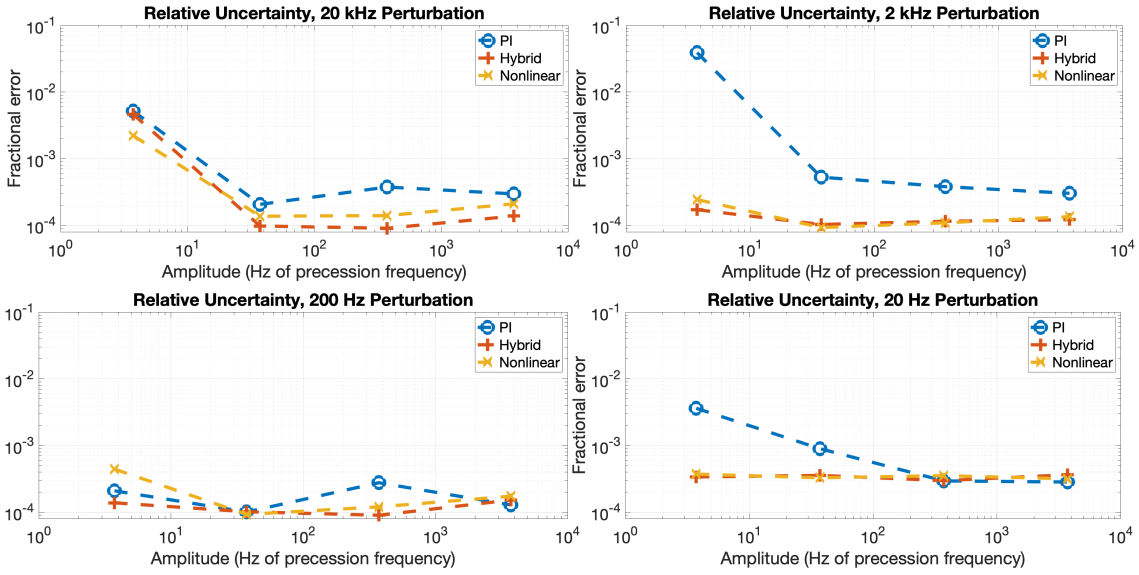

Figure 3.8: (color online) The fractional uncertainty of the measured static vector magnitudes, measured as the Allan deviation value at one second of integration time for each data set.

error, and the chosen feedback method will dominate the relative uncertainty at larger B' and larger ω, where $\delta B_{k,feedback} > \delta B_{k,noise}$.

3.4 Conclusions

The experiment described in this chapter examined and analyzed the comparative suitability of three different feedback methods for the closed-loop operation of a Bell–Bloom magnetometer (Bell and Bloom 1957; Bell and Bloom 1961) operating in Earth-field-scale magnetic fields and driven by intensity-modulated optical pump light with short-duty-cycle pulses of pump light at approximately the natural Larmor precession frequency with the intent of measuring the vector components of the incident magnetic field by way of applying oscillating magnetic fields (T.G. Walker and M.D. Bulatowicz 5 April 2022). The present work takes a first step toward 3-axis vector measurement by applying a single oscillating field along the bias field so that the effects of the feedback method on the relative accuracy and precision of the vector component measurement can be robustly

evaluated in a simple and straightforward manner. The investigated feedback methods include proportional integral (PI), nonlinear, and hybrid self-oscillator feedback methods.

This work has demonstrated, in accordance with Equations 3.19 and 3.20, that with a combination of sufficiently large amplitude and sufficiently high frequency applied oscillating magnetic field, appreciable improvements in measurement uncertainty can only be realized by way of improvements in the feedback loop response. In this work, these improvements are demonstrated when using feedback methods which capture a greater portion of the nonlinear response of the instrument to the increased perturbation amplitude and frequency (Equation 3.6). It is further important to note that the method outlined herein for the measurement of the vector magnetic field components draws its accuracy from the accuracy of the scalar magnetometer itself in addition to any accuracy considerations in the feedback method and the vector calculation process (Figure 3.5). Thus, to meet any particular absolute accuracy specification for the measurement of the vector components of the incident magnetic field, the scalar magnetometer must be at least as accurate as the desired vector accuracy.

In future work, the vector measurement and feedback methods described herein may be extended to 3-axis vector magnetic field measurement. Further, the vector component measurement algorithms may be implemented in real time for the active measurement of the vector components of the magnetic field. Additionally, as described above, the error signal $\delta\phi$ that drives the feedback loop can be updated to improve the response in a wide variety of magnetic field magnitudes. Finally, the magnetometer performance may be evaluated in an unshielded magnetic environment.

3.4.1 Data and MATLAB code Availability

Data and MATLAB code available at

`https://uwmadison.box.com/s/j1rdssru93jjyum7tj3yaoas15kugx0h`

(uploaded 28 March 2023). To process data, download all data and MATLAB code files (.m files) to a single folder and run the code `Data_to_Vector_Time_series.m` from

the same folder.

Chapter 4

All-Optical Synchronously Pumped RF Magnetometer

4.1 Introduction

Atomic magnetometers have demonstrated the potential for high sensitivity detection of magnetic fields at frequencies up to radio-frequency (RF) detection in the MHz regime without the use of cryogenic cooling (Keder et al. 2014b; Lee, V.G. Lucivero, et al. 2021; I.M. Savukov et al. 2005). Low-frequency to RF detection is useful for many applications from ultra-low-field MRI (Mazurek, Cahn, and M. Y. e. al 2021) to NMR spectroscopy (I.M. Savukov et al. 2005), magnetoencephalography (Rea et al. 2022), magnetocardiography (I. A. Sulai et al. 2019) and beyond. In contrast to an inductive pick-up coil (Gruber et al. 2018), optically pumped RF atomic magnetometers are effectively insensitive to electric fields and do not exhibit inductive cross-coupling, making them particularly amenable to use in array configurations. Typically, optically pumped RF magnetometers pump the spins along the bias field and allow the incident RF field to stimulate resonant precession of the spins about the bias field (for example, Keder et al. 2014b; Lee, V.G. Lucivero, et al. 2021; Bevington, Gartman, and Chalupczak 2019). This chapter covers the demonstration and analysis of what is to the best of our knowledge the first demonstration of

RF sensitivity for a synchronously pumped (Bell-Bloom) magnetometer; the underlying physics are presented along with a straightforward path to increased RF sensitivity.

It is worth noting that the typical optically pumped RF magnetometer approach exhibits a lower spin polarization relaxation rate as compared to the present experiment: in the absence of a transverse magnetic field component, spin exchange does not generate decoherence of the ensemble (see Chapter 2) and therefore the magnetometer can take full advantage of light-narrowing (Appelt et al. 1999) to increase the sensitivity. However, these RF magnetometers are primarily sensitive to RF magnetic fields transverse to the bias field and are unable to detect low-frequency fluctuations with high precision and low noise; depending on the application, this may be an advantage or a disadvantage. Further, a decrease in the achievable minimum detectable field (i.e. sensitivity) comes at the cost of response bandwidth; in the photon shot noise limited case, bandwidth and sensitivity are deterministically related by way of the transverse spin relaxation rate Γ_2. As will be shown shortly, an increase in sensitivity by way of decreasing response bandwidth will actually degrade RF detector performance for any applications benefiting from increased information transmission rates.

As described in Equation 2.29, the minimum detectable field for a shot noise limited magnetometer as in the present experiment is proportional to Γ_2, while as noted elsewhere in Chapter 2 the response bandwidth is Γ_2/π. RF applications in which information is being received by a detector benefit more from wideband detection than from an increase in signal-to-noise ratio (SNR): the Shannon-Hartley theorem states that the information capacity C of a signal with bandwidth BW is

$$C = BWLog_2(1 + SNR^2) \tag{4.1}$$

where the information capacity is in bits received by the detector per second. For a magnetometer operating in open-loop mode, then, with an incident radio frequency magnetic field component of B_{RF} and a total noise at the RF detection frequency of δB_{total}, the

Shannon-Hartley theorem states

$$C = \frac{\Gamma_2}{\pi} Log_2\left(1 + \frac{B_{RF}^2}{\delta B_{total}^2 \Gamma_2/\pi}\right) \tag{4.2}$$

which clearly demonstrates that in the limit where technical noise is negligible and where $\delta B_{total} \approx \delta B_{PSN} \propto \Gamma_2$, as in the present experiment, an optimal Γ_2 exists for maximizing the rate of transmitted information; further, the optimal Γ_2 is dependent on the magnitude of the received RF magnetic field. Therefore, a maximal degree of light narrowing is not necessarily advantageous and the advantage or disadvantage of the typical RF magnetometer over a synchronously pumped RF magnetometer must be evaluated on a case-by-case basis.

Equation 2.33 (recall: $\omega_L = \gamma|\mathbf{B}|$) suggests that for any modulating magnetic field orthogonal to the bias field one would expect a second-order response. While the relationship described in Equation 2.33 does hold for low-frequency magnetic fields ($\omega \ll \omega_L$), the approximation breaks down for magnetic field oscillations which are both orthogonal to the bias field and near the natural Larmor precession frequency ω_L. Naively solving the Bloch equations using only an examination of the effects of the magnetic fields, one will conclude that an experiment in which $\hat{B} \cdot \hat{R} = 0$ an oscillating field $\Omega_1 \hat{\Omega} \cos[(\omega_L + \Delta_1)t]$ with $\hat{\Omega} \cdot \hat{B} = 0$ should generate a precession phase response $\phi(t) \propto \Omega_1^2 \cos \Delta_1 t$. As shown in Section 4.3, while this relationship does indeed hold for larger values of Ω_1, in the small Ω_1 limit the magnetometer response is instead linear in Ω_1. We have found that the linear component of the response occurs due to an interaction between the applied oscillating magnetic field and the AC Stark shift $\Omega_{AC}(t)$ associated with the optical pump beam.

For optimal operation of the synchronously pumped magnetometer in this experiment, the optical pump beam is detuned from the D1 optical transition by a non-negligible fraction of the optical absorption linewidth and therefore induces a virtual magnetic field by way of the AC Stark shift, with expectation value $\langle \Omega_{AC} \rangle$ in units of induced precession frequency perturbation. With an optical pump along $\hat{R}$ and a bias field along $\hat{\Omega}$, using the same orthonormal basis set of $\hat{\Omega}, \hat{\xi}$, and $\hat{\eta}$ described in Chapter 2, the effect can

be qualitatively understood as follows: as described in Equation 2.2, $\Omega_{AC}(t)$ includes a significant Fourier component at ω_L, tipping the spins out of the $\hat{\xi} - \hat{\eta}$ plane into $\hat{\Omega}$; meanwhile, in the rotating reference frame of the precessing spins, the incident RF field includes a slow Fourier component at frequency Δ_1 which tips the spins from $\hat{\Omega}$ back toward the $\hat{\xi} - \hat{\eta}$ plane, at a phase deviation $\phi(t)$.

The Bloch equations for the time evolution of the spin $\vec{S}$ in the rotating reference frame of the precessing spins can naturally be divided into components parallel and perpendicular to the bias field; S_z and $S_+ = A_+ e^{i\omega t}$, respectively. Given a natural Larmor precession frequency ω_L, transverse relaxation rate Γ_2, an incident RF field along $\hat{\xi}$ of magnitude Ω_1 and frequency $\omega_1 \approx \omega_L$ with $\Delta_1 = \omega_L - \omega_1$, and an optical pumping rate $R(t)$ associated with a corresponding AC Stark shift $\Omega_{AC}(t)$, the Bloch equations for the transverse component of spin in the case where the optical pump pulse repetition rate is equal to the natural Larmor precession frequency of the spins become:

$$d_t A_+ = -\Gamma_2 A_+ - i\Big[\Omega_{AC}(t) + \Omega_1 cos(\omega_1 t)\Big] S_\Omega e^{-i\omega_L t} + R(t) e^{-i\omega_L t} \tag{4.3}$$

$$d_t S_\Omega = \Big[\Omega_{AC}(t) + \Omega_1 cos(\omega_1 t)\Big]\Big[A_+ e^{i\omega_L t}\Big] - \Big(\Gamma + R(t)\Big) S_\Omega \tag{4.4}$$

In the rotating reference frame, we can replace $\Omega_{AC}(t)e^{-i\omega_L t}$ and $R(t)e^{-i\omega_L t}$ with their time-average values, $\langle \Omega_{AC} \rangle$ and $\langle R \rangle$. Again assuming that the optical pump is on resonance with the natural Larmor precession frequency of the spins, in the rotating reference frame $\langle \Omega_1 cos(\omega_1 t) e^{\pm i\omega_L t} \rangle = i\frac{\Omega_1}{2} e^{\mp i\Delta_1 t}$ and Ω_{AC} does not generate any polarization along $\hat{\Omega}$. Equations 4.3 and 4.4 become

$$d_t A_+ = -\Gamma_2 A_+ - i\left[\langle \Omega_{AC} \rangle + \frac{\Omega_1}{2} e^{i\Delta_1 t}\right] S_\Omega + \langle R \rangle \tag{4.5}$$

$$d_t S_\Omega = \frac{i\Omega_1}{2} A_+ e^{-i\Delta_1 t} - (\Gamma + \langle R \rangle) S_\Omega \tag{4.6}$$

Solving Equations 4.5 and 4.6 for A_+:

$$A_+ = \frac{\langle R \rangle - iS_\Omega \langle \Omega_{AC} \rangle}{\Gamma_2} + \frac{S_\Omega \Omega_1}{2(i\Gamma_2 + \Delta_1)} e^{i\Delta_1 t} \tag{4.7}$$

and S_Ω:

$$S_\Omega = A_+ e^{-i\Delta_1 t} \frac{\Omega_1}{2\Big(i(\Gamma + \langle R \rangle) - \Delta_1\Big)} \tag{4.8}$$

One may solve Equations 4.7 and 4.8 in the limit that the oscillating components of A_+ are small compared to the steady-state component: in this limit, A_+ exhibits magnitude and phase oscillations at frequencies Δ_1 and $2\Delta_1$, proportional to $\Omega_1 \Omega_{AC}$ and Ω_1^2, respectively.

$$A_+ = \frac{\langle R \rangle}{\Gamma_2} \left(1 + \frac{\Omega_1 \Omega_{AC} (i\Delta_1 - (\langle R \rangle + \Gamma)) e^{i\Delta_1 t}}{2\Gamma_2 (\Delta_1^2 + (\langle R \rangle + \Gamma)^2)} + \frac{\Omega_1^2 e^{2i\Delta_1 t}}{4(i\Gamma_2 + \Delta_1)(i(\langle R \rangle + \Gamma) + \Delta_1)} \right) \tag{4.9}$$

with a first harmonic oscillation magnitude of

$$A_{+,osc1} = \frac{\langle R \rangle}{\Gamma_2} \frac{\Omega_1 \Omega_{AC}}{2\Gamma_2 \sqrt{\Delta_1^2 + (\langle R \rangle + \Gamma)^2}} \tag{4.10}$$

noted to be proportional to $\Omega_1 \Omega_{AC}$. Assuming fixed optical pump conditions one would therefore expect to observe a "baseband" precession phase modulation of the spins at the frequency Δ_1, proportional to Ω_1.

A sinusoidal magnetic field modulation along $\hat{\xi}$ is equivalent to a pair of rotating magnetic fields, co-rotating and counter-rotating with respect to the spins. It is specifically the co-rotating component which drives the slow phase shift response described in Equations 4.9 and 4.10. Equivalently, a sinusoidal modulation along $\hat{\eta}$ will exhibit a component co-rotating with the spins and will elicit the same magnitude response, phase shifted by an additional $\pi/2$.

Recall from Equation 2.10 that $R_{op} = \Phi_{op} \sigma(\nu_{op})$ which is maximized when ν_{op} is resonant with the D1 optical transition. Meanwhile, $\langle \Omega_{AC} \rangle$ is maximized when the optical pump beam is detuned significantly from resonance (Levi et al. 2016). Φ_{op} cannot be arbitrarily increased in this experiment due to limitations on the available pump photon

flux, and as a result the optimal ^{87}Rb polarization cannot be reached simultaneously with maximal $\langle\Omega_{AC}\rangle$. Thus, in this experiment I optimize the RF response by specifically maximizing the $\langle\Phi_{mod}\rangle P_{\perp}$ product as a function of ν_{op} by way of maximizing the output response of the magnetometer to an applied oscillating field detuned by Δ_1. I find optimal operation for RF sensitivity at approximately 9.2 GHz detuning from the wavelength of maximum optical absorption of the optical pump laser beam in the vapor cell used herein with $\Gamma_\nu \approx$14.4 GHz (Chapter 2). Compare this to the 3.5 GHz optical pump detuning at which the magnetometer sensitivity to low-frequency magnetic fields is optimized.

4.2 Experimental Apparatus

The basic experimental apparatus in this experiment is identical to the apparatus described in Chapter 2, but with the exception that an oscillating magnetic field $\vec{\Omega_1} = (a\hat{\xi} + b\hat{\eta})cos(\omega_1 t)$ orthogonal to the bias field $\vec{\Omega}$ is now included. An updated version of the abbreviated schematic of the experimental apparatus for this experiment is shown in Fig. 4.1, with the addition of the incident RF magnetic field and a reference for the orientation of the previously-mentioned orthonormal basis set established in Chapter 2. The applied RF oscillating field is driven by way of the modulation input on the same Twinleaf CSUA-1000 current source. Calibration of the applied RF field magnitude is performed relative to the low-frequency response (where low frequency modulations are much slower than Γ_2/π) through observation of the oscillating component of voltage across a resistor in series with the electrical current passing through the magnetic field coil, under the assumption that the current-to-field conversion is sufficiently similar at 200 kHz.

Regarding differences in the current-to-field conversion factor at low frequency versus 200 kHz, recall that the vapor cell is housed inside a Twinleaf MS-2 magnetic shield set with integrated magnetic field coils; the magnetic permeability of magnetic shielding alloys such as ASTM-A-753, Alloy 4 (also known as Hipernom, HyMu 80, Moly Permalloy, or Magnifer 7904) is dependent on frequency. Specifically, the magnetic permeability decreases with increasing frequency (particularly frequencies wherein the "skin depth" is much less than

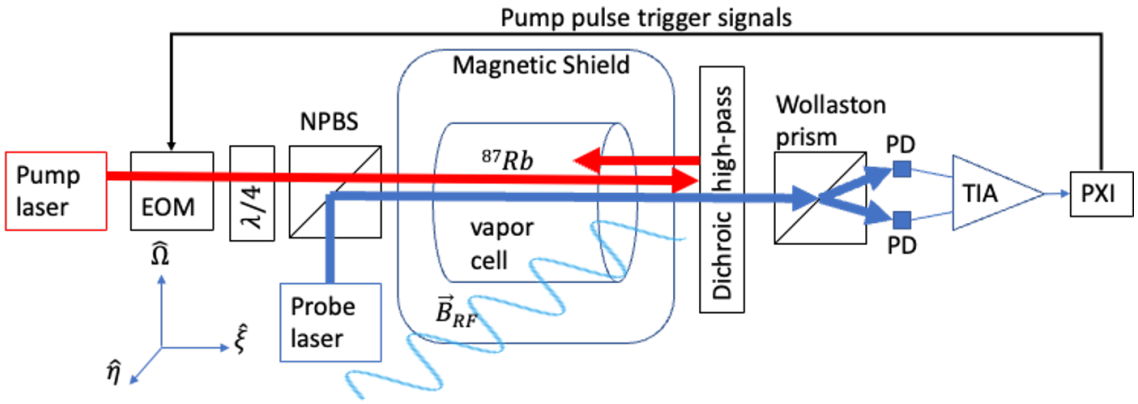

Figure 4.1: a) Block diagram of the operational concept. Similar to Figure 3.1 with the addition of an applied oscillating RF magnetic field in the $\xi - \eta$ plane and a reference showing the orientations of the orthonormal basis set in this experiment.

the thickness of the material). Estimates based on published data ("MuShield Frequently Asked Questions" n.d.) indicate that the effective permeability becomes proportional to $\Omega_1^{-2/3}$. However, based on this same data, the relative magnetic permeability is still expected to be greater than 100, leading to an expected deviation of less than 1 percent in the calibration.

While it is not explicitly shown in Equation 4.9, the low-frequency component of the spin precession phase response to the incident RF magnetic field is sensitive to the detuning of the optical pump pulse repetition rate relative to the natural Larmor precession frequency. When $\omega_L \neq \omega$ (i.e. the optical pump pulse repetition rate is not quite equal to the natural Larmor precession frequency of the spins), the RF response magnitude exhibits asymmetry about ω; this effect can be exploited to carefully tune $\omega \rightarrow \omega_L$ to a higher level of precision and accuracy than is achievable by maximizing the observed amplitude of the precession signal; I therefore set the condition of $\omega = \omega_L$ by square-wave modulating the frequency of the applied RF magnetic field and adjusting ω_L using the bias magnetic field until the RF response to $\pm\Delta_1$ is equal in magnitude.

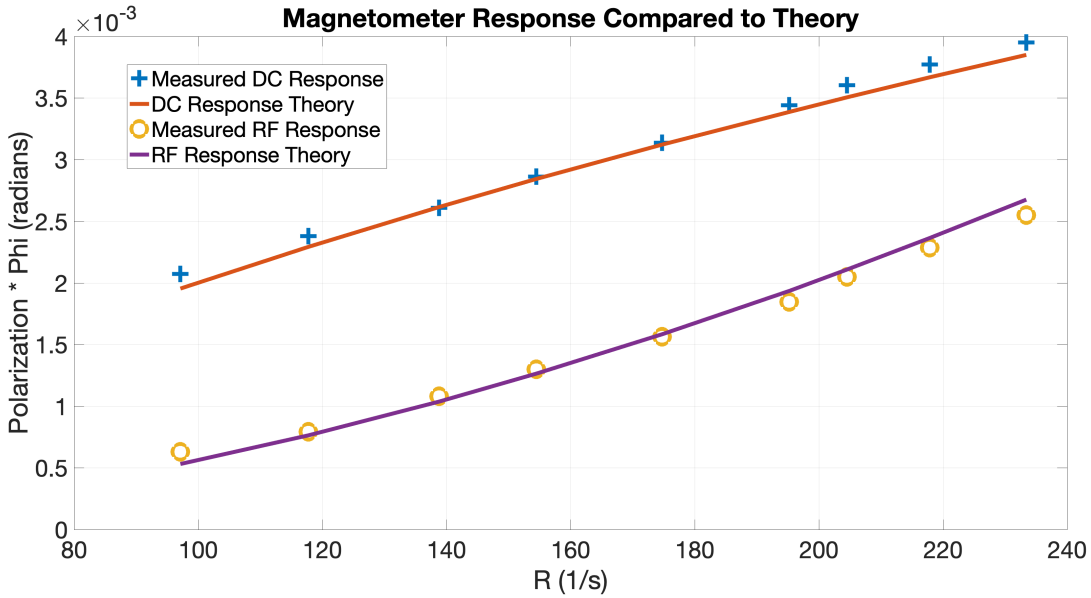

Figure 4.2: Measured spin precession phase response to a 20 Hz magnetic stimulus field along the bias field and a ($\Delta_1 = 20Hz$) stimulus field orthogonal to the bias field as compared to theory (Equations 2.36 and 4.10)

4.3 Results and discussion

I conducted a series of experiments to test the theory outlined in Equation 4.9 with measurement results validated against Equation 4.10. For the results shown in Figure 4.2, the "on" state intensity of the optical pump beam is varied by way of adjusting the voltage applied to the electro-optic modulator (Figure 2.6), thereby adjusting both the optical pumping rate and the AC Stark shift simultaneously. The "Theory" curves shown in Figure 4.2 are calculated using measured values of the magnetic field coil response to RF and DC inputs, the AC Stark shift, optical pumping rate, and transverse relaxation rate of the spins. For these experiments, I arbitrarily chose a DC stimulus field frequency of 20 Hz and corresponding RF detuning of 20 Hz for the sake of convenience: the chosen frequency is much lower than Γ_2, satisfying the quasi-steady-state requirements for validity of Equation 2.36 while remaining fast enough for robust triggering on the oscilloscope to provide for qualitative validation of the lock-in amplifier signal outputs. Figure 4.2 demonstrates that the experimental data and theory are in good agreement.

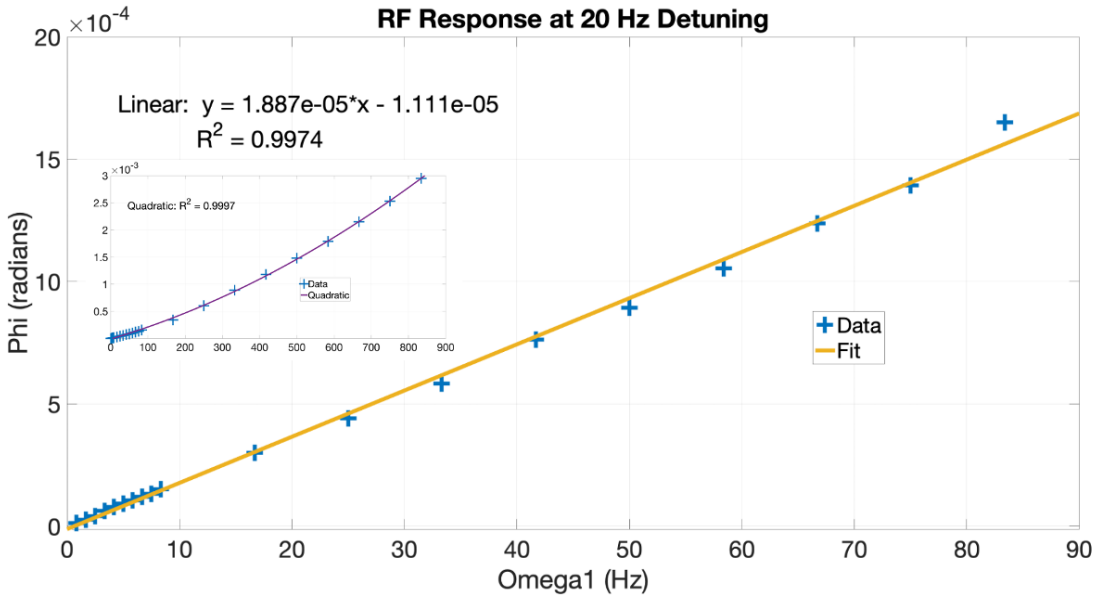

Figure 4.3: Spin precession phase response as a function of applied oscillating field magnitude at $\Delta_1 = 20Hz$ for small Ω_1. Inset: measured response out to larger Ω_1 with 2nd order polynomial fit. The data show a linear-dominated response at low Ω_1, with the response dominated by the second-order term at larger Ω_1, as expected

Equation 4.9 further predicts a linear relationship between the phase modulation of the spin precession and the magnitude of the applied RF magnetic field $\Omega_1 \hat{x} \cos[(\omega_L + \Delta_1)t]$ in the small Ω_1 limit for the response component driven by the AC Stark shift of the optical pump beam; when Ω_1 is comparable to or larger than $\langle \Omega_{AC} \rangle$, Equation 4.9 predicts a quadratic component to the response. As shown in Figure 4.3, this prediction also matches well with the experimental data; in the small Ω_1 limit the magnetometer exhibits a linear relationship between the response magnitude and RF field magnitude at frequency $\Delta_1 = 20Hz$. As Ω_1 increases, one may clearly observe the influence of the expected Ω_1^2 response component. As shown in Figure 4.3, the linear response dominates for $\langle \Omega_{AC} \rangle > \Omega_1$, while the second order response dominates when $\Omega_1 \gg \langle \Omega_{AC} \rangle$ (see Figure 4.3 inset).

The noise spectra shown in Figure 4.4 show a comparison between the sensitivity to RF fluctuations at $\Delta_1 = 20Hz$ versus the sensitivity to magnetic oscillations at 20 Hz. As shown in Figure 4.2, the observed spin precession phase modulation for the RF sensitivity in this magnetometer is lower than the sensitivity observed for low-frequency magnetic field

fluctuations, accounting for the difference in the observed noise minima. Easily visible in Figure 4.4 is the 20 Hz input stimulus signal of a known (calibrated) amplitude which is used for appropriate scaling of the lock-in amplifier output into magnetic units. Additional narrow frequency spikes arise in the spectrum due to electrical power; these are observable at 60 Hz and harmonics.

Noticeable in a comparison of the RF and DC sensitivity curves in Figure 4.4 is that the electrical power interference appears to be similarly shaped for the RF and DC sensitivity curves, though of approximately an order of magnitude difference in amplitude. Next, many harmonics of 60 Hz are present, indicating that the time series of the magnetometer data includes a coherent narrow pulse component at 60 pulses per second. Moreover, the frequency spike at 60 Hz is greater than the spike at 180 Hz, while the magnetic field produced by electrical current in the power lines exhibits a dominant component at 180 Hz–a condition which will be exacerbated by the frequency dependence of the magnetic permeability of the magnetic shielding material. Therefore, the presence of 60 Hz and harmonics is not consistent with being dominated by magnetic field oscillation at the vapor cell. As an additional indication of the cause, the electrical power interference is absent from the probe noise curve, taken upon placing a physical barrier between the optical pump beam and the vapor cell.

Together, these observations therefore suggest that the power line interference is likely observable on the optical pump beam; in particular, manifesting as phase deviations of the optical pump beam relative to its intended phase. A measurement of the optical pump beam pulse time series demonstrates that this is indeed the case: electrical power line interference modifies the timing (phase) of the optical pump pulses, leading to a perceived magnetic field according to Equations 2.33 and 2.36 in addition to any actual induced magnetic fluctuations observed by the precessing spins. The optical pump phase modulation is fundamentally a low-frequency effect; the magnetometer noise spectrum, referenced to RF sensitivity, simply makes the amplitudes appear larger than for the DC sensitivity: in the uncalibrated time series, these amplitudes are indeed identical. See

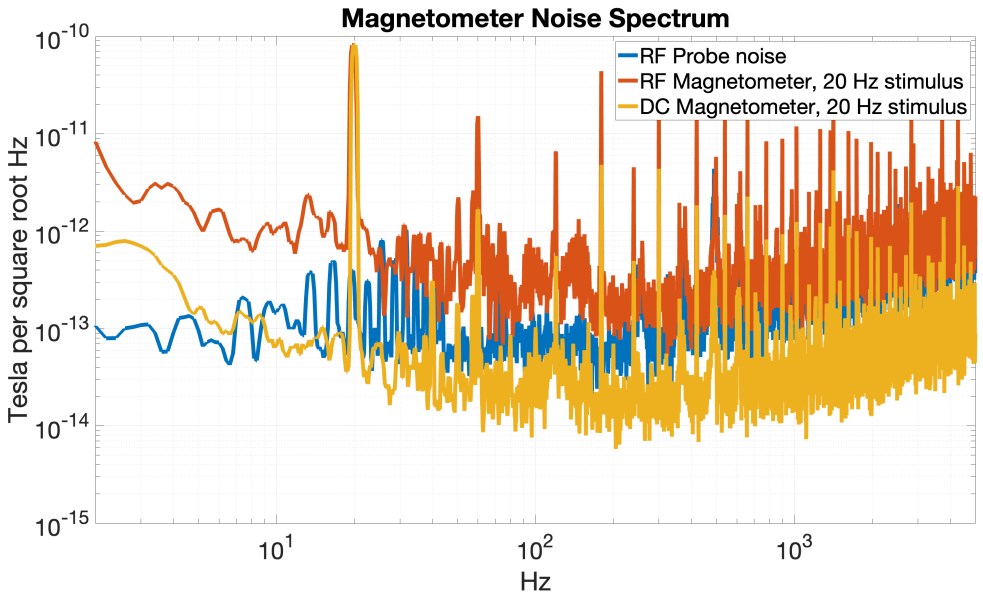

Figure 4.4: (Color online) Red trace: RF magnetometer noise spectrum. Yellow trace: DC magnetometer noise spectrum under identical conditions. Blue trace: RF magnetometer noise floor, dominated by probe noise but also including technical noise.

Appendix A.1 for more detail.

4.4 Conclusions

In the experimental work described in this chapter, I have presented the experimental demonstration and underlying theory for linearized detection of RF magnetic field oscillations near the natural Larmor precession frequency of the spins in an all-optical synchoronously pumped (Bell-Bloom) magnetometer with parallel optical pump and probe beams. Repeated searches of the literature have uncovered no evidence of a prior demonstration of RF sensitivity in a transversely synchronously pumped magnetometer; thus, to the best of our knowledge this work represents the first demonstration of a transversely pumped RF Bell-Bloom magnetometer with parallel pump and probe beams. A potential advantage of a Bell-Bloom RF magnetometer as in the present work is that the RF sensitivity does not inherently interfere with the ability to detect low-frequency magnetic field fluctuations; further, the RF sensitivity can be emphasized or minimized by appropriate

choice of the optical pump wavelength, thereby controlling the value of $\langle \Omega_{AC} \rangle$.

Chapter 5

Conclusions and Future Work

5.1 Suggestions for Future Work

Future work can build upon the successes of the work described in this thesis. For the scalar and differential scalar magnetometer, an alternative pulsed optical pump light source with greater "on" state intensity will enable wider signal-to-noise ratio bandwidth, optical pump pulse intensity profile shaping or optimization, and the use of a physically larger vapor cell for further improvement in the fundamental noise limits. As noted in Chapter 4, such a pump light source will also generate increased RF detection sensitivity. An increase in the optical path length of the probe beam in the polarized vapor (Equation 2.39) will further reduce the photon shot noise limit. For example, a multi-pass optical probe will improve the photon shot noise limit approximately as the square root of the number of passes (recall from Chapter 2: the probe is detuned by several linewidths from the optical transition and exhibits an optimal photon scattering rate, therefore requiring further detuning for optimal operation when the probe passes multiple times through the vapor cell). Next, the differential scalar magnetometer measurement can be implemented in a closed-loop fashion as described in Chapter 2 to improve the common-mode rejection ratio and thereby improve differential detection performance (I. Sulai et al. 2019).

For detection of the vector components of the magnetic field, operation may be extended to full three-axis detection using the method described in Chapter 3, and the

feedback loops can be further improved by modifying the error signal driving the loops from a simple phase difference to the product of phase and observation time such that the loop gain becomes substantially independent of precession frequency (magnetic field magnitude). Finally, a feed-forward system may be implemented to modulate the optical pump pulse repetition rate coherently with the applied oscillating magnetic fields, lifting the presently observed feedback loop performance limits.

Future work on detection of the vector components of magnetic field may also implement a different mechanization than the oscillating field method described in this thesis. Specifically, the addition of a second optical probe beam, orthogonal to the present optical pump/probe axis, can track the "cone of precession" of the spin ensemble in real-time through direct observation of the polarization component projection along a second axis. With the exception of a sign degeneracy that can be lifted using a weak applied oscillating magnetic field, this will allow real-time observation of the vector direction of the incident magnetic field. Consider a pump/probe axis along $\hat{R} = \hat{z}$, a bias magnetic field $\vec{\Omega} = \Omega(\hat{x}sin(\theta_B)cos(\phi_B) + \hat{y}sin(\theta_B)sin(\phi_B) + \hat{z}cos(\theta_B)$, and a second probe along $\hat{x}$. As described in Equation 2.24, a probe along some axis $\hat{x_1}$ will measure $\vec{P} \cdot \hat{x_1}$.

The Bloch equation (Equation 2.12) indicates that for an optical pump repetition rate $\omega = \omega_L$

$$P_z = P\Big(cos^2(\theta_B) + sin^2(\theta_B)cos(\omega t)\Big) \tag{5.1}$$

where terms are as defined above. Taking the ratio of the oscillating component to the steady-state component, we can solve for the opening angle of the cone (up to a sign ambiguity), but not the direction ϕ_B in which that opening is pointing:

$$tan^2(\theta_B) = \frac{P_z(\omega)}{P_z(0)} \tag{5.2}$$

Meanwhile, the orthogonal probe allows for measurement of ϕ_B. The polarization along $\hat{x}$ is

$$P_x = Psin(\theta_B)\Big(cos(\theta_B)cos(\phi_B)[1 - cos(\omega t)] + sin(\phi_B)sin(\omega t)\Big) \tag{5.3}$$

which exhibits a steady-state component and oscillating components that are in-phase and in quadrature with the oscillating component of P_z. Demodulating the output from the $\hat{x}$ probe, we get a demodulated in-phase component

$$P_x cos(\omega t) = P_{x,in-phase} = -Psin(\theta_B)cos(\theta_B)cos(\phi_B) \tag{5.4}$$

and a demodulated quadrature component

$$P_x sin(\omega t) = P_{x,quadrature} = \frac{1}{2}Psin(\theta_B)sin(\phi_B) \tag{5.5}$$

So, the probe along $\hat{x}$ allows us to solve for ϕ_B:

$$tan(\phi_B) = \frac{-2P_{x,quadrature}cos(\theta_B)}{P_{x,in-phase}} \tag{5.6}$$

Having solved for both the opening angle of the cone relative to the optical pump axis $\hat{z}$ and its orientation about $\hat{z}$, we have solved for the vector direction of the incident magnetic field, up to a sign ambiguity in θ_B. The sign ambiguity can be lifted by applying a slow oscillating field $\Omega_z cos\omega_z t$ along $\hat{z}$ and demodulating $\theta_B(t)$:

$$Sign(\theta_B(t)cos(\omega_z t)) = Sign(\theta_B) \tag{5.7}$$

5.2 Conclusions

In this thesis, I have presented a modernized Bell-Bloom magnetometer operating in the continuously synchronously pumped regime for measurement of Earth-field-scale magnetic fields with potential for high performance in a wide range of unshielded applications including biomagnetism, magnetic aiding of navigation, geosensing, RF detection, and many more. I have provided the basic theory and description of the underlying physics of operation, which in turn provides the basis for high-precision measurement of Earth-field-scale magnetic fields. I have described the experimental apparatus and data collection method.

I have demonstrated a combination of scalar magnetic field measurement performance and differential scalar measurement performance matching the best published scalar sensitivity for measurement of Earth-field-scale magnetic fields and approaching the best published result for differential scalar sensitivity, respectively, but using a physically simpler apparatus with simplified data interpretation and much wider measurement bandwidth. I have formulated and demonstrated a deterministic physics-based procedural optimization of this magnetometer for measurement at the standard quantum limit. I have demonstrated a signal-to-noise ratio in the mid-$10^9\sqrt{Hz}$ range with deterministic means of further improvement in noise, bandwidth, or both, and guidance for the same. I have constructed and validated a finite element model for more-global optimization of the performance characteristics of this magnetometer given a particular vapor cell geometry and optical pump and probe intensity profile, capable of analytically optimizing experimental parameters such as vapor cell size and shape, buffer gas pressure, and both pump and probe optical intensity profile. I have provided and demonstrated physics-based guidelines for design of an optical detection system strongly dominated by photon shot noise, allowing the technical noise background to fully support operation at the standard quantum limit of the magnetometer.

I have demonstrated that this magnetometer technology provides scalar magnetic field sensitivity and differential scalar sensitivity in Earth-field-scale magnetic fields that rivals the performance of superconducting quantum interference devices (SQUIDs) while avoiding the primary disadvantages of SQUIDs. Unlike SQUIDs, this magnetometer does not require cryogenic cooling or any of the associated costs and limitations, and therefore shows potential for more-widespread application and use.

I have analyzed and demonstrated the feasibility of a method for measurement of the vector components of a magnetic field, measuring and characterizing a single axis of vector measurement as the first step toward a full three-axis implementation. In this experiment, we formulated and tested three methods of closed-loop feedback comprising a proportional-integral (PI) method that responds to measured phase deviations between

the precessing spin ensemble and the optical pump repetition rate; a nonlinear method which builds upon the PI method with a predictive element that attempts to predict and compensate for the next incremental measured phase deviation; and a hybrid self-oscillator method which builds upon the nonlinear method to add a pump pulse phase correction factor. I have analytically and experimentally demonstrated the performance limitations associated with magnetometer noise and feedback loop limitations, and I have designed, coded, and optimized a set of filters for detection of the vector components of magnetic field using this method.

I have performed possibly the first demonstration of linearized RF sensitivity in a continuously synchronously-pumped (Bell-Bloom) magnetometer. In conjunction with the RF sensitivity, the magnetometer is still capable of measuring low-frequency fields with high precision, with the ratio of RF sensitivity to low-frequency sensitivity tunable by way of using the optical pump beam wavelength and intensity to control the magnitude of the AC Stark shift. We have analyzed the physical basis of the linearized RF sensitivity and have been able to determine that the sensitivity arises from an interaction between the incident RF magnetic field and the oscillating AC Stark shift induced by the optical pump beam. I have experimentally validated the theory, finding RF response in good agreement with theoretical predictions.

Finally, I have provided guidance for future work including an analysis of a future means of measurement of the vector direction of the incident magnetic field. This alternative method overcomes the feedback loop performance limitations of the method demonstrated in the present work (recall: by means of applied oscillating magnetic fields along each axis to be observed). I have provided for future enhancement in sensitivity, bandwidth, or both. With the research presented in this thesis and some design and development of automated startup and tuning features, it is feasible to design and build a robust, fieldable Bell-Bloom magnetometer exceeding both the sensitivity and the bandwidth of the best commercially available magnetometers on the market today.

Appendix A

Apparatus Concerns and Upgrades for Future Work

A.1 Optical Pump Pulse Triggering Circuitry

As shown in Figure 2.6 in the main text, the optical pump pulses are shuttered using an electro-optic modulator (EOM; Newport 4102). Not shown is the custom circuitry used for driving the EOM: the pulses of voltage across the EOM are driven using a half-bridge circuit (Texas Instruments LMG3411EVM), which is itself controlled using logic circuitry set up for break-before-make control of the switches in the half bridge, with analog RC delays of the logic inputs. Figure A.1 shows a simplified schematic of the half-bridge triggering circuitry. As is clear from Figure A.1, the break-before-make condition is necessary to ensure that transistors Q1 and Q2 are never simultaneously in the "on" state, thus avoiding a condition known as "shoot through" wherein the high voltage is connected directly to ground.

Input control logic signals are provided by either a NI PXIe-6614 precision counter and timing reference module or a PXIe-5171R reconfigurable oscilloscope module, as appropriate to the experiment in question. The circuit is configured such that a "logic 1" state corresponds to the "on" state of the optical pump beam (i.e. the shuttering system shown

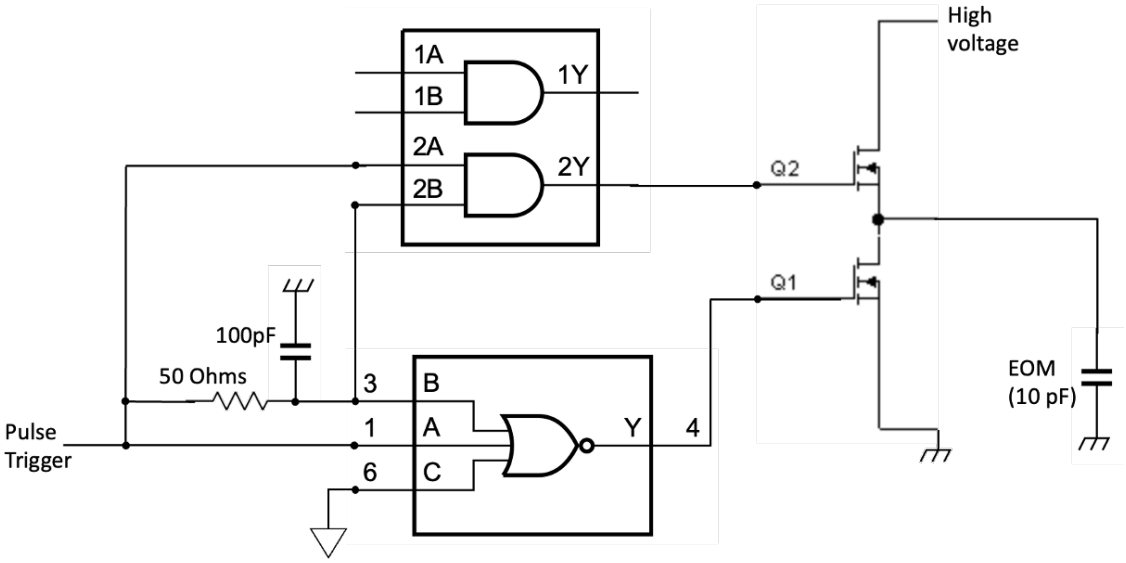

Figure A.1: Simplified schematic of the logic circuit driving the electro-optic modulator shown in Figure 2.6. A configurable analog delay element consisting of a simple resistor-capacitor (RC) delay enforces a break-before-make condition for the half-bridge so that the high-voltage power supply does not connect directly to ground.

in Figure 2.6 allows transmission of the optical pump light to the vapor cell) and the "logic 0" state corresponds to the "off" state of the pump, blocking the optical pump light. As mentioned in the main text, the typical optical pump power at the exit of the pump beam optical fiber is approximately 20 mW in the "on" state and in the low-single-digit μW in the "off" state.

As will be shown shortly, component choices for this circuit can significantly impact the optical pump pulse timing noise observed at the spin ensemble. As mentioned in the main text, Equation 2.36, a perceived deviation in magnetic field magnitude results from any phase deviation between the polarimeter signal (ideally, identical to the phase of the precessing spin ensemble) and the optical pump pulse triggering signal. Slow deviations in the phase of the optical pump pulses observed by the spin ensemble (where slow indicates frequencies less than Γ_2/π) as compared to the optical pump pulse triggering signals will generate corresponding phase deviations of the spin ensemble precession and polarimeter signal relative to the pump pulse triggers. This will in turn generate slow modulation of the output of the lock-in amplifier and be interpreted as deviations in the magnetic field

even though they arise from a non-magnetic source.

A.1.1 Electromagnetic Interference: Pump Pulse Timing Fluctuations

Sources of vulnerability to electromagnetic interference in the circuit shown in Figure A.1 include 1) finite ground impedance between the pulse trigger signal output from the PXI computer, the power supply (not shown) and the EOM driving circuit; 2) finite noise and ripple in the supply voltage powering the logic circuitry; 3) temperature and voltage sensitivity of the analog delay elements; and 4) impedance matching conditions for the logic signals and for the EOM drive signal. Each of these sources of vulnerability will modulate the timing of the actual optical pump pulses as compared to the timing of the pump pulse trigger logic signal; the mechanism of each is described below.

Finite ground impedance between the pulse trigger signal from the PXIe-6614 module and the logic circuits shown in Figure A.1 allows the relative ground potentials for each to vary with time due to inductive and capacitive coupling of external interference signals. The rise and fall rates of the logic signals generated by the PXIe-6614 are themselves finite, and the point in time at which they surpass the logic threshold in the logic circuit triggering signals will therefore vary with any difference in ground potential: see Figure A.2 for an illustration based on the rising edge of the trigger signal. Correspondingly, the finite slope of the falling edge of the trigger signal leads to sensitivity to fluctuations in ground potential. To leading order, the timing offset error is inversely proportional to the magnitude of the triggering signal voltage slope. To the extent that the rising and falling edges are of identical absolute slope, a slow fluctuation in relative ground potential will change the length of the pulse but not its center. However, it is rare for logic circuits to exhibit identical rising and falling edge slope magnitudes.

The logic circuit supply voltage is of particular concern; as is typical for logic circuits (see, for example, the data sheet for 74LVC1G27) the input threshold voltages are approximately proportional to supply voltage. Similar to the ground potential effects shown in Figure A.2, a change in threshold voltage corresponding to a fluctuation in the logic

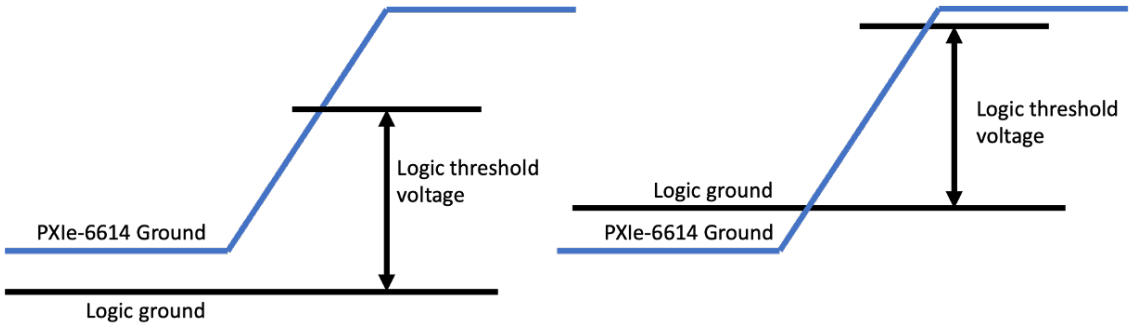

Figure A.2: Illustration (exaggerated for clarity) of the effects of a difference in ground potential between the logic trigger signal source and the local logic ground. As the illustration shows, a change in ground potential causes a change in the time at which a rising trigger signal passes the logic threshold of the logic device. A change in timing generates a phase shift between the optical pump pulse trigger signal and the actual optical pump pulse as observed by the spin ensemble.

circuit supply voltage leads to a change in phase delay between a trigger signal and a change at the logic circuit output. Consider, for example, the 50 Ohm, 100 pF RC delay element shown in Figure A.1: the RC time constant is 5 nanoseconds. For the example of the 3.3V logic trigger signals in this experiment, the voltage slope at one time constant is $3.3V * Exp[-1]/(5ns) = 0.24GV/s$, ignoring the finite rise time of the logic trigger signal. A 1 mV fluctuation in logic threshold, then, contributes approximately 4.1 picoseconds of change in delay time. For a 200 kHz precession frequency, this is equivalent to 5.2 microradians of phase shift. When $\Gamma_2 = 720/s$, Equations 2.33 and 2.36 indicate a magnetic equivalent modulation of approximately 500 fT. The voltage slope at the output of the RC delay element is itself sensitive to temperature and voltage; the resistor and capacitor both exhibit some finite temperature sensitivity to their impedance, and the capacitor will exhibit a finite voltage coefficient of capacitance.

Additional sensitivity arises due to the finite slopes of the logic circuit output signals which are used for control of the half-bridge driver circuit. Supply voltage fluctuations generate fluctuations in the peak output voltages and the output currents (which are proportional to the slope magnitude) from the logic circuits, which in turn modify the time at which the trigger signal is observed by the half-bridge driver circuit.

Impedance mismatches between the PXIe-6614 trigger signal source and the logic cir-

cuit configuration shown in Figure A.1 will lead to rising and/or falling edge slope modifications that can include non-monotonicity of the voltage slope as well as "bouncing" or "ringing" of the voltage at the input of the logic circuits at the terminal ends of the triggering signals. Impedance mismatches between the EOM and the high voltage power supply source can generate similar fluctuations on the voltage across the EOM crystal, in turn leading to fluctuations of the turn-on and turn-off times for the optical pump pulses observed by the spin ensemble as well as generating unintended optical intensity fluctuations at the trailing edge of turn-on and the trailing edge of turn-off.

Figures 2.9 and 2.10 clearly show an increase in noise power spectral density at the lowest frequencies in addition to a large number of finite frequency spikes. The magnitudes of these spikes was noted to depend in part on the ground impedance between the logic circuit and the PXIe, the logic power supply, and the high voltage power supply. These spikes largely consist of 1) 60 Hz and harmonics corresponding to lab electrical power, 2) undersampled interference from the heater drive signal (demonstrated to be modifiable by changing the distance and orientation of the heater drive cable relative to other circuitry in the system), and 3) only a few frequency spikes of undetermined source. Based on examination of the data in Figures 2.9 and 2.10, it is clear that the majority of the observed finite frequency spikes are magnetic fluctuations or equivalent; nearly all of the finite frequency spikes in Figure 2.9 disappear upon blocking the optical pump beam, and the low-frequency noise is dramatically decreased (i.e. the Probe Noise trace in the plot shows very few spikes and reduced low-frequency noise). However, it was not clear whether these spikes and low-frequency noise were generated by actual magnetic fluctuations or solely a magnetic-equivalent effect. Upon examination of the RF sensitivity data (Figure 4.4) it became clear that much of the low-frequency noise and finite frequency spikes are magnetic-equivalent rather than actual magnetic fluctuations. I therefore formulated the hypothesis based on Equation 2.22 that fluctuations in the phase of the optical pump pulses observed by the spin ensemble as compared to the triggering signal may be to blame.

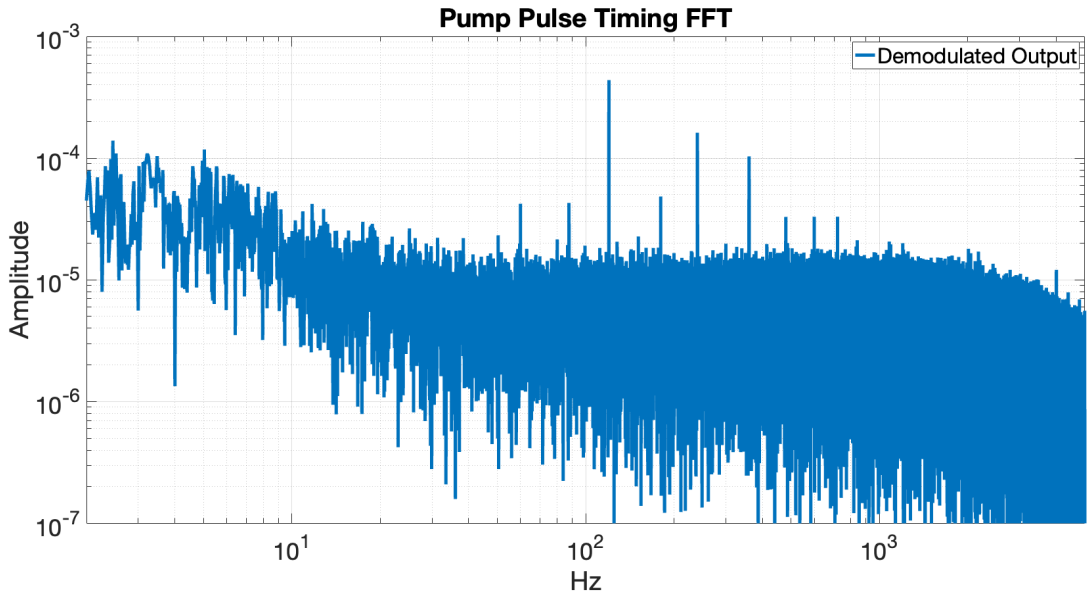

Figure A.3: FFT of lock-in amplifier output (Demodulated Output) when measuring the optical pump pulses observed at the polarimeter (Figure 2.5) with reference to the optical pump pulse trigger signals. A number of the undesired features of the measured magnetic noise spectra are visible, confirming that the optical pump pulse timing does indeed fluctuate.

I tested the pump pulse timing hypothesis using two methods, producing equivalent results. The first method used the lock-in amplifier for demodulation, while the second method utilized manual demodulation of a measured time series of the optical pump pulses. For both methods, the optical probe beam is blocked and the dichroic mirror is removed so that the optical pump beam reaches the polarimeter; the resulting polarimeter signal is sent to the appropriate input (lock-in amplifier input or NI PXIe-5171 oscilloscope card analog input, as appropriate). Further, for both methods the optical pump beam pulse repetition rate is detuned far from the natural Larmor precession frequency, and the vapor cell is at room temperature, such that the influence of the spins on the measurement is negligible. The observed noise spectrum is shown in Figure A.3; multiple harmonics of 60 Hz are easily visible in the spectrum, as is the rising low-frequency noise, confirming that the pump pulse timing does indeed exhibit fluctuations corresponding to at least some of the features observed in Figures 2.9, 2.10, and 4.4.

A.1.2 Suggested Improvements for Future Work

As noted above, the finite slope of the logic triggering signals generates timing errors inversely proportional to the slope magnitude. The slowest voltage slopes come from the analog RC delay and the logic circuit outputs (which in turn trigger the half-bridge driver). The corresponding timing noise can be dramatically mitigated through a combination of improvements to the logic supply voltage and increases in the voltage slopes. First, the logic supply voltage can be improved in stability and noise by the use of a high-performance linear regulator combined with a low-noise supply for the higher voltages required by the LMG3411 EVM half-bridge. Second, the analog delay element can be replaced by a digital delay element with significantly increased voltage slope. Finally, the logic circuits can be replaced with faster circuits performing the same function: the 74HCT08N "AND" gate and CD74HCT02E "NOR" gate can be replaced with alternatives with slope magnitudes several times larger.

A.2 Photon Shot Noise Limited Polarimeter Circuit

To achieve photon shot noise limited detection, one must utilize an appropriately designed differential photocurrent detection circuit with inherent noise well below the photon shot noise limit: as will be shown below, straightforward design guidelines for such a circuit are easily developed. A conceptual schematic of our custom differential photocurrent detection circuit for each of the polarimeters in the present work is shown in Figure A.4. Consider a total photocurrent I: each photodetector in our balanced polarimeter will output a current of $I/2$ when $\theta = 0$ and I when $\theta = \pi/4$. With an appropriate choice of operational amplifier (op-amp) the gain resistor GR will strongly dominate the noise produced by the transimpedance stage itself for mA-scale photocurrent and volt-scale output. With a chosen target transimpedance amplifier output voltage of V_{out} at current I, the gain resistor value $GR = V_{out}/I$.

The Johnson-Nyquist thermal noise limit δI_J in the gain resistor is a function of the resistance GR, Boltzmann's constant k_B, and absolute temperature T:

$$\delta I_J = \sqrt{4k_BT/GR} = \sqrt{4k_BTI/V_{out}} \tag{A.1}$$

which then demonstrates that the criterion for the output signal to be strongly dominated by photon shot noise on the photocurrent is $V_{out} \gg 2k_BT/q \rightarrow V_{out} \gg 52mV$ at a gain resistor temperature of 300 Kelvin. Note that this result for V_{out} is independent of the magnitude of the total photocurrent as long as the gain resistor dominates the noise observed at the output of the transimpedance stage in the absence of photocurrent. Amplification of the transimpedance output signal to 10V at $I/2$, for example, meets this criterion for mA-scale photocurrents while being well within the output capabilities of many junction field effect transistor (JFET) input op-amps: JFET input op-amps typically exhibit input-referred electrical current noise in the range of tens of $fA/\sqrt{Hz}$ or lower; a photocurrent-equivalent noise of less than 0.1 μA. Thus, for a 3 mW optical probe beam as is used in the present work (roughly 1.5 mA total photocurrent when using silicon photodetectors), it is straightforward to design a transimpedance amplifier with its output strongly dominated by photon shot noise. The next stage in the signal processing chain is the lock-in amplifier (SR865A) used in the present work for demodulation of the differential photodetector signal. The lock-in amplifier exhibits an input noise of 2.5 $nV/\sqrt{Hz}$; compare this to the optical probe shot noise limit at $V_{out} = 10V$ and 1.5 mA photocurrent of $GR\sqrt{2Iq} = V_{out}\sqrt{2q/I} = 146nV/\sqrt{Hz}$. Clearly, the photon shot noise in this example will strongly dominate the white noise observed at the lock-in amplifier output.

A.3 Basic Overview of Direct Digital Synthesis (DDS)

Direct digital synthesis (DDS) is a method of generating quasi-arbitrary frequencies using a discrete-time system. The major components of a DDS system are 1) a timebase such as the 250 MHz crystal oscillator for FPGA "clocking" in the present experiment (divided by 2 such that the FPGA timebase is 125 MHz), 2) a digital register representing phase,

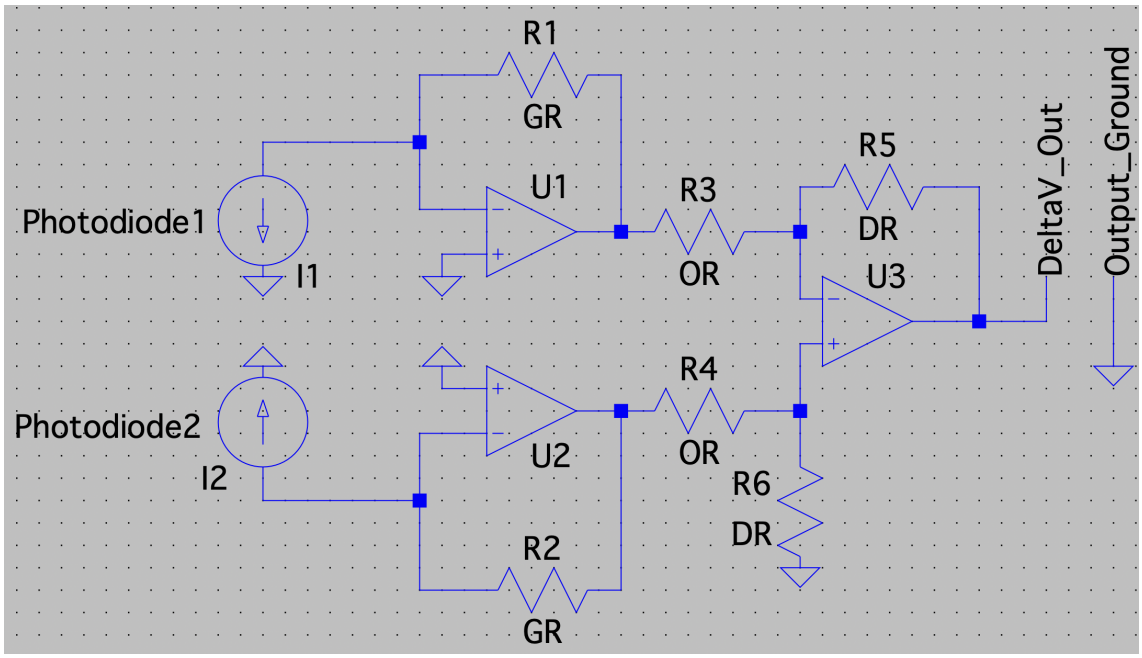

Figure A.4: Conceptual schematic of the differential detection circuit used in the present work. The photocurrents from each of two photodetectors are represented as current sources; these currents are sent through transimpedance amplifiers (current to voltage conversion; operational amplifiers U1 and U2), and the resulting voltage signals are differenced (operational amplifier U3). The transimpedance gain is set by gain resistor GR, the transimpedance output voltage is sent through output resistor OR, and the difference gain resistor value DR sets the gain on the difference between the two photocurrents.

configured to "roll over" the remainder upon overflow, 3) a digital increment value known as the phase increment word, and 4) a means of converting the phase to a sinusoid.

A useful metaphor is to think of the DDS system as a clock: the hands of the clock each are associated with their own phase increment per "tick" of the reference oscillator; 6 degrees per increment for the second hand, 1/10 of a degree for the minute hand, and 1/600 of a degree for the hour hand. In this metaphor, the 64-bit phase register in our experiment represents a full cycle of a hand around the clock face, while the phase increment word represents the step size taken for each "tick." A typical clock uses an integer number of increments per cycle, but a DDS is not constrained to integer values. Consider a DDS using a clock frequency F_{clk}, a phase increment word of M least-significant bits (LSB) where M is an integer, and a DDS phase register size of n bits as described above. The

output frequency F_{out} will be

$$F_{out} = \frac{F_{clk} M}{2^n} \tag{A.2}$$

so it becomes clear that the frequency step size is simply $F_{clk}/2^n$ (i.e. increments of 1 LSB in the phase increment word). As mentioned above, in this experiment $n = 64$: based on the FPGA's 125 MHz timebase we have a frequency resolution equivalent to approximately 10^{-21} Tesla; clearly, this experiment does not make use of the full 64 bit capability in the present DDS implementation. A phase register size of 64 bits was chosen based on limitations of the LabVIEW FPGA programming interface, which for the 2019 version used in this experiment does not allow fully arbitrary choice of register size; registers are either 32 bits (approximately 4 pT per M increment) or 64 bits. To avoid excessive quantization uncertainty a 64-bit phase register was chosen.

A.3.1 Application of DDS in the Present Work

In this experiment, when operating in closed-loop measurement mode, a single DDS controls both the optical pump pulses and the spin precession signal model against which the polarimeter signal is compared (Chapter 3). For the purpose of turning the pump pulses on and off, there is a simple control algorithm that uses the user-defined duty cycle d and triggers a logic 1 at the trigger output when the phase register is between 0 and $d * 2^n$, inclusive of the end points. The spin precession model against which the polarimeter signal is compared, on the other hand, uses a look-up table to generate the sine and cosine components using the phase register as 2π of total phase.

A.4 Rationale for Commercially Available Equipment Choices

A.4.1 Introduction

I selected the commercially available equipment used in this experiment using rigorous rationale based on physics and engineering. Recall from Chapters 2 through 4 that this equipment includes a NI PXIe chassis with a computer module, a NI PXIe-6614 timing ref-

erence module using an oven-compensated crystal oscillator (OCXO) for low noise and stability, and a NI PXIe-5171R reconfigurable multifunction oscilloscope module. While the choice of including a computer module in the PXIe system is fairly obvious—it allows the PXIe system to act as a fully integrated control, data collection, and data interpretation system—technical rationale for these choices are described below. Additional commercially available equipment includes 1) a SRS SR865A lock-in amplifier; 2) a laser system composed of Vescent Photonics low-noise laser controller and 795 nm laser module with integrated optical isolators, free-space-to-optical-fiber coupling modules, a Newport 4102 electro-optic modulator for "DC" polarization rotation (DC to 200 MHz), and a Thorlabs laser controller with 780 nm distributed Bragg Reflector (DBR) laser; and 3) commercially available optical elements and optics mounts from Thorlabs, with the exception of the dichroic mirror from Semrock. As will be demonstrated shortly, the commercially available electronic equipment for data processing and optical pump pulse generation was chosen based on sound technical rationale.

A.4.2 NI PXIe-6614 Timing Reference Module

The NI PXIe-6614 timing reference module is designed to provide a precision frequency reference that coordinates the timing of all modules in the PXIe chassis. As described above, the magnetometer developed in the present work is effectively a magnetic field to frequency transducer; noise and drift in the frequency reference, therefore, can limit the ability to measure the magnetic field. Particularly important for the present experiment are the long-term frequency drift in the OCXO, typically characterized as close-to-carrier phase noise, and random white-noise phase jitter at the optical pump pulse repetition rate ($\omega/2\pi$ in Hz). My goal in selecting an appropriate frequency reference for the present experiment was to ensure that the frequency-reference-related technical noise is negligible with respect to the magnetometer's fundamental noise limits (Chapter 2).

Given a curve of phase noise versus offset from the carrier, typically expressed in decibels relative to the carrier per Hz (dBc/Hz), the root-mean-square (RMS) time error

at a given frequency can be calculated based on the carrier frequency itself and the total area under the curve calculated from the frequency of interest up to twice the carrier frequency (Kester n.d.). The effect of random white-noise phase jitter at the optical pump pulse repetition rate (200 kHz at 29 μT for ^{87}Rb) can be calculated as follows. Consider a RMS time error δt at $\omega/2\pi$: the total magnetic field error δB_{clk} arising from this random white noise in the clock reference on a per square root Hz basis is simply

$$\delta B_{clk} = \frac{\delta t \Gamma_2}{\pi\gamma}\sqrt{\frac{\omega}{2\pi}} \tag{A.3}$$

Based on the phase noise specification for the OCXO used in the PXIe-6614 timing reference module (available upon request from NI), the OCXO phase noise at 200 kHz contributes less than 0.1 $fT/\sqrt{Hz}$, sufficient to support the noise budget described in Chapter 2.

The effect of frequency drift, meanwhile, contributes to the magnetic field measurement accuracy: this particular OCXO exhibits an "aging drift" of within 0.5 parts per billion (ppb) per day. For the 10 MHz timebase reference, 0.5 parts per billion per day is approximately 17 $\mu Hz/\sqrt{s}$ frequency uncertainty (a technical noise limit of 2.5 $fT/\sqrt{s}$ magnetic field uncertainty), approximately 3 orders of magnitude below the observed magnetometer noise at 1 second (Figure 2.9) and is therefore negligible. In principle, the frequency could be "trained" by way of coordination to universal coordinated time (UTC) or to another long-term accurate frequency reference such as GPS (which is itself stabilized based on the international standard definition of the second) to decrease this further.

A.4.3 NI PXIe-5171R Reconfigurable Oscilloscope Module

The NI PXIe-5171R module serves as a low-noise high-speed and high-resolution oscilloscope and includes a user-programmable FPGA that can take advantage of the oscilloscope front-end functionality (250 million samples per second at 14 bits resolution with programmable full-scale voltage input range up to $\pm 2.5V$) and includes digital outputs. My goals in selecting this module for signal acquisition, processing, and feedback included

the following. First, the analog-to-digital conversion needed a sufficient signal-to-noise ratio to be limited by photon shot noise from the magnetometer rather than technical noise. Second, the data acquisition speed and timebase frequency needed to be much faster than the maximum expected alkali precession frequency in the experiment (approximately 1 MHz based on the limitations of the Twinleaf CSUA-1000 current source driving its maximum current through the Z axis coil in the Twinleaf MS-2 magnetic shield set); based on the desire for digital filtering, a factor of 100 provides for high-performance filtering as well as a minimum phase resolution of 1/100 of a precession cycle per "tick" of the timebase–helpful for phase deviation modeling and detection as well as for pump pulse phase resolution when operating the instrument in closed-loop mode. Third, the module needed to include sufficient data processing power to acquire, filter, and model the incoming data; apply active closed-loop feedback with low latency; and record magnetometer data at sample rates of approximately the precession frequency of the spins or faster to enable robust post-processing of the data as necessary. Finally, the module needed to include not only analog inputs but also low-noise digital logic outputs to control the "on" versus "off" states of the optical pump. The NI PXIe-5171R module meets all of these requirements.

The low-noise front end (analog to digital conversion) exhibits a voltage white noise of approximately 82 $nV/\sqrt{Hz}$ at a $\pm 2.5V$ full-scale range setting; greater than 12 noise-free bits of precision (bit 13 down to 2, where bit 0 is the least-significant bit in the measurement register) at the full sampling rate with the anti-alias filter enabled (see specifications for NI PXIe-5171). The polarimeter preamp circuit, meanwhile, is designed to generate approximately a 2V peak-to-peak sinusoidal signal in response to the Faraday rotation of the optical probe beam (Chapter 2), occupying approximately 11 of these noise-free bits with signal (bits 12 down to 2 contain signal and are effectively noise free in technical noise terms), and the output of the polarimeter preamp exhibits a photon shot noise at the differential output of approximately 220 $nV/\sqrt{Hz}$. The photon shot noise limit, then, at the sampling rate, allows for 10 effective noise free bits (utilizing noise-free

bits 12 down to 3).

The least-squares fitting algorithm for detection of the phase difference δ between the optical pump pulse repetition rate DDS and the measured precession signal (see Chapter 3 for more detail) fits the measured polarimeter signal to a sinusoid over one full cycle of the pump pulse control DDS: at the typical precession frequency of 200 kHz in this experiment, the measurement period is approximately 1250 samples. With a root-mean-square (RMS) fractional amplitude noise of $1/2^{10}$ (≈ 0.001)per sample

A.5 SRS SR865A Lock-in Amplifier

Key performance parameters for the lock-in amplifier used in the experiments described in Chapter 2 and 4 include the following. First, the range of acceptable input frequencies must exceed the maximum precession frequency of the spins (approximately 1 MHz as mentioned above). The SR865A can accept input frequencies of up to 4 MHz. Second, the phase lock loop that generates a reference demodulation sinusoid based on the "external reference" input must exhibit a low enough phase noise to support measurement of the magnetic field to the desired precision. The specification for the SR865A phase noise with external reference input is 0.001 degrees RMS at 1 kHz; for $\Gamma_2 = 1000/s$, this corresponds to a technical noise limit based on phase error of $tan(\delta) = \delta\omega/\Gamma_2 \rightarrow \delta B = 1.4aTRMS$ (see Equation 2.36); clearly negligible with respect to the observed magnetic field noise (Figure 2.9). Third and last, the input-referred voltage noise must be negligible with respect to photon shot noise; the specification of $2.5nV/\sqrt{Hz}$ at 10 mV (RMS) input range can be extrapolated to approximately 75 $nV/\sqrt{Hz}$ per input channel (A or B inputs) as compared to the single-ended polarimeter output photon shot noise of 220 $nV/\sqrt{Hz}$. Therefore, the SR865A lock-in amplifier supports operation of the magnetometer described herein at its fundamental noise limits based on the standard quantum limit.

A.5.1 Laser System

The laser system for this experiment needs to provide 1) pulsed laser light with a frequency range significantly narrower than the broadened optical transition linewidth for optical pumping based on the D1 optical transition of ^{87}Rb and 2) CW laser light, much narrower than the broadened optical transition linewidth for detection of spin polarization based on the D2 optical transition of ^{87}Rb. The optical pump power as observed at the spins during the "on" state of the optical pump beam must be sufficient to achieve the optimal polarization (0.87 in this experiment: see Chapter 2) in order to provide for optimization of the fundamental noise of the magnetometer, and must be capable of operating at a stable wavelength, detuned from the optical transition by a non-negligible fraction of the optical linewidth. The optical probe must be of appropriate optical intensity and must be capable of operating at a stable wavelength detuned by several linewidths from the D2 optical transition.

Bibliography

Goldstein, Herbert (1980). *Classical Mechanics, Second Edition*. Reading, Massachusetts: Addison-Wesley.

Strasburger, J.; Cheulkar, and R. B.; Wakai (2008). "Magnetocardiography for fetal arrhythmias". In: *Heart Rhythm* 5.7, pp. 1073–1076.

Hämäläinen, M. et al. (1993). "Magnetoencephalography—Theory, instrumentation, and applications to noninvasive studies of the working hu-man brain". In: *Rev. Mod. Phys.* 65, pp. 413–497.

Sulai, I.A. et al. (2019). "Characterizing atomic magnetic gradiometers for fetal magnetocardiography". In: *Rev. Sci. Instrum.* 90.085003, pp. 413–497. URL: https://doi.org/10.1063/1.5091007.

Boto, E. et al. (2022). "Triaxial detection of the neuromagnetic field using optically-pumped mag-netometry: Feasibility and application in children". In: *Neuroimage* 252.119027. URL: https://doi.org/10.1016/j.neuroimage.2022.119027.

Rea, M. et al. (2022). "A 90-channel triaxial magnetoencephalography system using optically pumped magnetometers". In: *Ann. N. Y. Acad. Sci.* 1517, pp. 107–124. URL: https://doi.org/10.1111/nyas.14890.

Klotz, T., L. Gizzi, and O. Röhrle (2022). "Investigating the spatial resolution of EMG and MMG based on a systemic multi-scale model". In: *Biomech. Model. Mechanobiol.* 21, pp. 983–997. URL: https://doi.org/10.1007/s10237-022-01572-7.

Hoshino, Y. et al. (2022). "Magnetoneurography as a novel functional imaging technique for the ulnar nerve at the elbow." In: *Clin. Neurophysiol.* 138, pp. 153–162.

Lorenz, R., J. Jones, and J. Wu (2003). "Mars magnetometry from a tumbleweed rover". In: *In Proceedings of the 2003 IEEE Aerospace Conference Proceedings (Cat. No.03TH8652)*.

Afach, S. et al. (2021). "Search for topological defect dark matter with a global network of optical magnetometers". In: *Nature Physics* 17, pp. 1396–1401.

Vo, C.K. et al. (2020). "Determining the Depth and Location of Buried Pipeline by Magnetometer Survey". In: *J. Pipeline Syst. Eng. Pract.* 11.04020001. URL: https://ascelibrary.org/doi/abs/10.1061/%5C%28ASCE%5C%29PS.1949-1204.0000438.

Koss, P. et al. (2022). "Optically Pumped Magnetometer Measuring Fatigue-Induced Damage in Steel". In: *Appl. Sci.* 12.1249. URL: https://www.mdpi.com/2076-3417/12/3/1329.

Canciani, A. and J. Raquet (2016). "Absolute Positioning Using the Earth's Magnetic Anomaly Field". In: *Navigation* 63, pp. 111–126. URL: https://onlinelibrary.wiley.com/doi/abs/10.1002/navi.138.

Lee, W., V.G. Lucivero, et al. (2021). *Portable Magnetometry for Detection of Biomagnetism in Ambient Environments*.

Bell, W.E. and A.L. Bloom (1957). "Optical detection of magnetic resonance in alkali metal vapor". In: *Phys. Rev.* 107.1559.

— (1961). "Optically driven spin precession". In: *Phys. Rev. Lett.* 6, pp. 280–281.

Grujic, Z. D. and A. Weis (2013). *Atomic magnetic resonance induced by amplitude-, frequency-, or polarization-modulated light.*

Huang, H.C. et al. (2015). "Three-axis atomic magnetom-eter based on spin precession modulation". In: *Appl. Phys. Lett.* 107.182403. URL: https://doi.org/10.1063/1.4935096.

Gerginov, V. and S. Krzyzewski S. Knappe (2017). "Pulsed operation of a miniature scalar optically pumped magnetometer". In: *J. Opt. Soc. Am. B* 34, pp. 1429–1434.

Gerginov, V., M. Pomponio, and S. Knappe (2020). *Scalar Magnetometry Below 100 $fT/Hz^{1/2}$ in a Microfabricated Cell.*

Li, Songsong et al. (2021). *Faraday rotation Bell Bloom atomic magnetometer using an alternating pump probe beam.*

Gartman, R. et al. (2018). *Linear and nonlinear coherent coupling in a Bell-Bloom magnetometer.*

Allred, J. C. et al. (2002). "High-Sensitivity Atomic Magnetometer Unaffected by Spin-Exchange Relaxation". In: *Phys. Rev. Lett.* 89.130801.

Dang, H.B., A.C. Maloof, and M.V. Romalis (2010). "Ultrahigh sensitivity magnetic field and magnetization measurements with an atomic magnetometer". In: *Applied Physics Letters* 97.151110.

Seltzer, S. and M. Romalis (2004a). "Unshielded three-axis vector operation of a spin-exchange-relaxation-free atomic magnetometer". In: *Appl. Phys. Lett.* 85, pp. 4804–4806. URL: https://doi.org/10.1063/1.1814434.

Soheilian, A., M. Ranjbaran, and M.M. Tehranchi (2020). *Position and Direction Tracking of a Magnetic Object Based on an Mx-Atomic Magnetometer.* URL: https://doi.org/10.1038/s41598-020-57923-w.

Canciani, Aaron Joseph and Christopher J. Brennan (2020). "An Analysis of the Benefits and Difficulties of Aerial Magnetic Vector Navigation". In: *IEEE Transactions on Aerospace and Electronic Systems* 56.6, pp. 4161–4176. DOI: 10.1109/TAES.2020.2987475.

NOAA (n.d.). *Enhanced Magnetic Model (EMM).* URL: https://www.ngdc.noaa.gov/geomag/EMM/.

Lee, W., V. Lucivero, et al. (2021). *Heading errors in all-optical alkali-metal-vapor magnetometers in geomagnetic fields.* URL: https://doi.org/10.1103/PhysRevA.103.063103.

Sui, Y. et al. (2014). *Compact fluxgate magnetic full-tensor gradiometer with spher-ical feedback coil.* URL: https://doi.org/10.1063/1.4856675.

Huang, Y., L. Wu, and D. Li (2015). *Theoretical Research on Full Attitude Determination Using Geomagnetic Gradient Tensor.* URL: https://doi.org/10.1017/S0373463315000259.

Schönau, T. et al. (2013). "SQUID-based setup for the absolute measurement of the Earth's magnetic field". In: *Supercond. Sci. Technol.* 26.e035013. URL: https://doi.org/10.1063/1.1814434.

Budker, D. and M. Romalis (2007). *Optical Magnetometry.* URL: https://doi.org/10.1038/nphys566.

Grosz, A., M. Haji-Sheikh, and S. Mukhopadhyay (2017). *High Sensitivity Magnetometers*. Springer. URL: https://doi.org/10.1007/978-3-319-34070-8_16.

Thiele, T., Y. Lin, and M.O. Brown (2018). *Self-Calibrating Vector Atomic Magnetometry through Microwave Polarization Reconstruction*. URL: https://doi.org/10.1103/PhysRevLett.121.153202.

Alldredge, L. (1960). "A proposed automatic standard magnetic observatory". In: *Journal of Geophysical Research* 65.3777.

Wang, Tao et al. (2023). *Pulsed ^{87}Rb vector magnetometer using a fast rotating field (preprint)*. arXiv: 2304.00214 [quant-ph].

Keder, David A. et al. (2014a). "An unshielded radio-frequency atomic magnetometer with sub-femtoTesla sensitivity". In: *AIP Advances* 4.127159. URL: https://doi.org/10.1063/1.4905449.

Savukov, I.M. et al. (2005). *Tunable Atomic Magnetometer for Detection of Radio-Frequency Magnetic Fields*.

Mazurek, M.H., B.A. Cahn, M.M. Yuen, et al. (2021). "Portable, bedside, low-field magnetic resonance imaging for evaluation of intracerebral hemorrhage". In: *Nat Comms* 12.5119. URL: https://doi.org/10.1063/1.4905449.

Gerginov, V. and F. Da Silva (27 September 2022). *Optically pumped magnetometers for communication reception*.

Savukov, I., Y. Kim, and M.G. Boshier (2017). "High-sensitivity operation of single-beam optically pumped magnetometer in a kHz frequency range". In: *Measurement Science and Technology* 28.3. DOI: 10.1088/1361-6501/aa58b4.

Bai, Xuanyao et al. (2023). "Atomic magnetometers and their application in industry". In: *Frontiers in Physics* 11. DOI: 10.3389/fphy.2023.1212368. URL: https://www.frontiersin.org/articles/10.3389/fphy.2023.1212368.

Gruber, Bernhard et al. (2018). "RF coils: A practical guide for nonphysicists". In: *Journal of magnetic resonance imaging : JMRI* 48.3, pp. 590–604. DOI: doi:10.1002/jmri.26187.

Keder, David A. et al. (Dec. 2014b). "An unshielded radio-frequency atomic magnetometer with sub-femtoTesla sensitivity". In: *AIP Advances* 4.127159. DOI: https://doi.org/10.1063/1.4905449.

Bevington, P., R. Gartman, and W. Chalupczak (2019). "Enhanced material defect imaging with a radio-frequency atomic magnetometer". In: *Journal of Applied Physics* 125.9, p. 094503. DOI: 10.1063/1.5083039. URL: https://doi.org/10.1063/1.5083039.

Appelt, S. et al. (1999). "Light narrowing of rubidium magnetic-resonance lines in high-pressure optical-pumping cells". In: *Phys. Rev. A* 59 (3), pp. 2078–2084. DOI: 10.1103/PhysRevA.59.2078. URL: https://link.aps.org/doi/10.1103/PhysRevA.59.2078.

Limes, M.E. et al. (July 2020). "Portable Magnetometry for Detection of Biomagnetism in Ambient Environments". In: *Phys. Rev. Appl.* 14 (1), p. 011002. DOI: 10.1103/PhysRevApplied.14.011002. URL: https://link.aps.org/doi/10.1103/PhysRevApplied.14.011002.

Dang, H., A. Maloof, and M. Romalis (2010). "Ultrahigh sensitivity magnetic field and magnetization measurements with an atomic magnetometer". In: *Appl. Phys. Lett.* 97.151110. URL: https://doi.org/10.1063/1.3491215.

Wang, K. et al. (2022). "Triaxial closed-loop measurement based on a single-beam zero-field optically pumped magnetometer". In: *Frontiers in Physics* 10.1205. URL: https://www.frontiersin.org/articles/10.3389/fphy.2022.1059487.

Yan, Y. et al. (2022). "Three-axis closed-loop optically pumped magnetometer operated in the SERF regime". In: *Optics Express* 30, pp. 18300–18309. URL: https://doi.org/10.1364/OE.458367.

Lu, F. et al. (2022). "Triaxial Vector Operation in Near-Zero Field of Atomic Magnetometer With Femtotesla Sensitivity". In: *IEEE Trans. Instrum. Meas.* 71, pp. 1–10. URL: https://doi.org/10.1109/TIM.2022.3162282.

Seltzer, S. and M. Romalis (2004b). "Unshielded three-axis vector operation of a spin-exchange-relaxation-free atomic magnetometer". In: *Appl. Phys. Lett.* 85, pp. 4804–4806. URL: https://doi.org/10.1063/1.1814434.

Perry, A. et al. (2020). "All-optical intrinsic atomic gradiometer with sub-20 fT/cm/rtHz sensitivity in a 22 μT earth-scale magnetic field". In: *Optics Express* 28, pp. 36696–36705. URL: http://opg.optica.org/oe/abstract.cfm?URI=oe-28-24-36696.

Oelsner, G. et al. (2022). "Integrated Optically Pumped Magnetometer for Measurements within Earth's Magnetic Field". In: *Optics Express* 17.024034. URL: https://doi.org/10.1103%5C%252Fphysrevapplied.17.024034.

Perry, A. R. et al. (2020). *All-optical intrinsic atomic gradiometer with sub-20 $fT/cm/sqrtHz$ sensitivity in a 22 μT earth-scale magnetic field.*

GEM Systems GSMP-35 Potassium Magnetometer (2023). URL: https://www.gemsys.ca/wp-content/themes/gemsystems/pdf/GEM_Potassium_GSMP-35_fin.pdf.

Sheng, D., S. Li, et al. (Apr. 2013). "Subfemtotesla Scalar Atomic Magnetometry Using Multipass Cells". In: *Phys. Rev. Lett.* 110 (16), p. 160802. DOI: 10.1103/PhysRevLett.110.160802. URL: https://link.aps.org/doi/10.1103/PhysRevLett.110.160802.

Sulai, I. A. et al. (2019). *Characterizing atomic magnetic gradiometers for fetal magnetocardiography.*

Tost, J., M. Bulatowicz, and T.G. Walker (2023). *Feedback Methods for Vector Measurements Using an All-Optical Atomic Magnetometer.*

Walker, T.G. and M.D. Bulatowicz (5 April 2022). *Synchronous Light-Pulse Atomic Magnetometer System.*

Seltzer, S. J., P. J. Meares, and M. V. Romalis (May 2007). "Synchronous optical pumping of quantum revival beats for atomic magnetometry". In: *Phys. Rev. A* 75 (5), p. 051407. DOI: 10.1103/PhysRevA.75.051407. URL: https://link.aps.org/doi/10.1103/PhysRevA.75.051407.

Walker, Thad G. and William Happer (Apr. 1997). "Spin-exchange optical pumping of noble-gas nuclei". In: *Rev. Mod. Phys.* 69 (2), pp. 629–642. DOI: 10.1103/RevModPhys.69.629. URL: https://link.aps.org/doi/10.1103/RevModPhys.69.629.

Chen, W. C. et al. (Jan. 2007). "Spin-exchange optical pumping of ^{3}He with Rb-K mixtures and pure K". In: *Phys. Rev. A* 75 (1), p. 013416. DOI: 10.1103/PhysRevA.75.013416. URL: https://link.aps.org/doi/10.1103/PhysRevA.75.013416.

Franz, F.A. and C. Volk (1976). *Spin relaxation of rubidium atoms in sudden and quasi-molecular collisions with light-noble-gas atoms.*

Happer, William (Apr. 1972). "Optical Pumping". In: *Rev. Mod. Phys.* 44 (2), pp. 169–249. DOI: 10.1103/RevModPhys.44.169. URL: https://link.aps.org/doi/10.1103/RevModPhys.44.169.

Happer, W. and W. A. Van Wijngaarden (1987). "An optical pumping primer". In: *Hyperfine Interactions* 38, pp. 435–470. DOI: https://doi.org/10.1007/BF02394855.

Romalis, M. V., E. Miron, and G. D. Cates (1997). *Pressure broadening of Rubidium D_1 and D_2 lines by ^3He,^4He, N_2, and Xe: Line cores and near wings.*

Steck, Daniel A. (2003). *Rubidium 87 D Line Data (revision 1.6, 14 October 2003).*

Rosenberry, M. A. et al. (Feb. 2007). "Radiation trapping in rubidium optical pumping at low buffer-gas pressures". In: *Phys. Rev. A* 75 (2), p. 023401. DOI: 10.1103/PhysRevA.75.023401. URL: https://link.aps.org/doi/10.1103/PhysRevA.75.023401.

Electric-Dipole Polarizabilities of Atoms, Molecules, and Clusters (1997). World Scientific Pub Co, Inc, New York. ISBN: 9810224931.

Budker, D. and D. Jackson Kimball (2013). *Optical Magnetometry.* Cambridge University Press. URL: https://doi.org/10.1017/CBO9780511846380.

Alem, O., K.L. Sauer, and M.V. Romalis (2013). *Spin damping in an rf atomic magnetometer.*

Ledbetter, M.P. et al. (2008). *Spin-exchange-relaxation-free magnetometry with Cs vapor.*

Sheng, D., A. R. Perry, et al. (Jan. 2017). "A microfabricated optically-pumped magnetic gradiometer". In: *Applied Physics Letters* 110.3, p. 031106. ISSN: 0003-6951. DOI: 10.1063/1.4974349. eprint: https://pubs.aip.org/aip/apl/article-pdf/doi/10.1063/1.4974349/13993001/031106_1_online.pdf. URL: https://doi.org/10.1063/1.4974349.

Happer, W., Y.Y. Jau, and T. Walker (2010). *Optically Pumped Atoms".*

Lucivero, V.G. et al. (2022). *Femtotesla Nearly-Quantum-Noise-Limited Pulsed Gradiometer at Earth-Scale Fields.*

Smullin, S. J. et al. (2009). *Low-noise high-density alkali-metal scalar magnetometer.*

Zhang, R. et al. (2020). *Portable intrinsic gradiometer for ultra-sensitive detection of magnetic gradient in unshielded environment.*

Zhivun, Elena et al. (Mar. 2019). "Dual-Axis π-Pulse Magnetometer with Suppressed Spin-Exchange Relaxation". In: *Phys. Rev. Appl.* 11 (3), p. 034040. DOI: 10.1103/PhysRevApplied.11.034040. URL: https://link.aps.org/doi/10.1103/PhysRevApplied.11.034040.

Bulatowicz, M. (30 March 2012). *Temperature System with Magnetic field Suppression.*

Kitching, J. (2018). *Chip-scale atomic devices.* URL: https://doi.org/10.1063/1.5026238.

Savukov, I. M. and M. V. Romalis (Feb. 2005). "Effects of spin-exchange collisions in a high-density alkali-metal vapor in low magnetic fields". In: *Phys. Rev. A* 71 (2), p. 023405. DOI: 10.1103/PhysRevA.71.023405. URL: https://link.aps.org/doi/10.1103/PhysRevA.71.023405.

Happer, W. and A.C. Tam (1977). *Effect of rapid spin exchange on the magnetic-resonance spectrum of alkali vapors.*

"Texas Instruments Application Report SLVA043B: Noise Analysis in Operational Amplifier Circuits" (n.d.). In: (). URL: https://www.ti.com/lit/an/slva043b/slva043b.pdf?ts=1692299527760.

Wyllie, Robert et al. (2012). *Optical magnetometer array for fetal magnetocardiography.*

Limes, M. E. et al. (2020). *Portable magnetometry for detection of biomagnetism in ambient environments.*

Lucivero, V. G. et al. (Jan. 2021). "Femtotesla Direct Magnetic Gradiometer Using a Single Multipass Cell". In: *Phys. Rev. Appl.* 15 (1), p. 014004. DOI: 10.1103/PhysRevApplied.15.014004. URL: https://link.aps.org/doi/10.1103/PhysRevApplied.15.014004.

Wu, Shuhe et al. (2023). *Quantum magnetic gradiometer with entangled twin light beams.* URL: https://www.science.org/doi/10.1126/sciadv.adg1760.

Li, Uundi et al. (2018). *SERF Atomic Magnetometer - Recent Advances and Applications: A Review.*

Yang, Kang et al. (2016). *Weakly Damped SQUID Gradiometer With Low Crosstalk for Magnetocardiography Measurement.*

Bison, G. et al. (2009). *A room temperature 19-channel magnetic field mapping device for cardiac signals.*

Garachtchenko, Alex et al. (1999). *Baseline distance optimization for SQUID gradiometers.*

Gravrand, O. and A. Khokhlov et al (2001). *On the calibration of a vectorial 4He pumped magnetometer.* URL: https://doi.org/10.1186/BF03351692.

Mazurek, M.H., B.A. Cahn, and M.M. Yuen et al (2021). "Portable, bedside, low-field magnetic resonance imaging for evaluation of intracerebral hemorrhage". In: *Nat Commun* 12.5119. DOI: https://doi.org/10.1038/s41467-021-25441-6.

Levi, F. et al. (Feb. 2016). "Precision test of the ac Stark shift in a rubidium atomic vapor". In: *Phys. Rev. A* 93 (2), p. 023433. DOI: 10.1103/PhysRevA.93.023433. URL: https://link.aps.org/doi/10.1103/PhysRevA.93.023433.

"MuShield Frequently Asked Questions" (n.d.). In: (). URL: http://www.mu-metal.com/faqs.html.

Kester, Walt (n.d.). "Converting Oscillator Phase Noise to Time Jitter". In: MT-008 (). URL: https://www.analog.com/media/en/training-seminars/tutorials/MT-008.pdf.